FULL REALIZATION OF QUANTITATIVE CORTICAL BRAIN SURFACE MEASUREMENT THROUGH STEREO PAIR WITHOUT SEPARATE TRACKING TECHNOLOGY

By

Xiaochen Yang

Dissertation

Submitted to the Faculty of the

Graduate School of Vanderbilt University

in partial fulfillment of the requirements

for the degree of

DOCTOR OF PHILOSOPHY

in

Computer Science

December 14, 2019

Nashville, Tennessee

Approved:

Dr. Benoit M. Dawant

Dr. Michael I. Miga

Dr. Jack Noble

Dr. Reid Thompson

Dr. Richard Alan Peters

ACKNOWLEDGMENTS

Wow! It has been a long journey to reach this stage, and I cannot believe it is almost done. Obtaining a Ph.D. is always one of the very important goals in my life. And I am thankful for everything I experienced these years during the way pursuing the highest degree of human beings.

I would like to express my gratitude to Dr. Benoit Dawant for his consistent guidance and support during all these years. Dr. Dawant is one of the most hardworking professors I have ever met. The huge amount of publications and citations demonstrates his enthusiasm about his research. He is always very patient in guiding my research. I still remember how carefully and detailedly he reviewed my first paper. His valuable feedbacks keep benefiting my following publications. He also has broaden horizon and lots of collaborations so that he introduces me to work with Dr. Miga.

I would also like to express my appreciation to Dr. Michael Miga for his direct mentoring and guidance. Dr. Miga is enthusiastic about his research without doubt, and he is the person who leads me to this image-guided surgery field which intrigued me a lot. I am impressed by his passion and dedication to this field. And I really enjoy the moments when we discuss the projects and papers in his office because he creates and communicates a bold direction and inspires me to think differently. I would not be able to finish those projects and papers without his consistent and patient advisory.

In addition, I would like to thank Dr. Reid Thompson for his assistance on experiments. Dr. Thompson is an excellent neurosurgeon with more than 20 years' experience. He provides constructive feedbacks on my projects, including the software and extensions I built. He also teaches me a lot of medical knowledge related to brain surgery that enhances my research background. I also want to thank Dr. Jack Noble and Dr. Richard Alan Peters to be my dissertation committee members. Moreover, my appreciation would be given to Dr. Lola Chambless, Dr. Peter Morone, and Dr. Le He for taking time out of their busy

schedule to participate the research experiments. Thanks to Dr. Hansen Bow, I really enjoy collaborating with you on the project. I would like to acknowledge John Fellenstein from the Vanderbilt Machine Shop for his assistance in making our surgical setup.

I am so lucky to be able to work in two labs (MIP and BML). I want to thank the colleagues in the MIP lab, Dr. Rui Li, Bill Rodriguez, Dr. Yuan Liu, Dr. Yiyuan Zhao, Dr. Dongqing Zhang, Dr. Ahmet Cakir, Jianing Wang, Srijata Chakravorti, Yubo Fan, Can Cui, and Han Liu. Also, I want to thank the people in BML lab, Dr. Logan Clements, Dr. Ankur Kumar, Dr. Rebekah Griesenauer, Dr. Saramati Narasimhan, Ma Luo, Jon Heiselman, Winona Richey and Alice Ding.

Last, I want to sincerely thank my family for their endless love and support. Without their understanding and support, I certainly would not be able to achieve so far.

TABLE OF CONTENTS

LIST OF TABLES

LIST OF FIGURES

Chapter I

INTRODUCTION

1.1 Objective

Conventional image-guided surgery navigation systems are widely used for guiding brain tumor resection in order to localize the craniotomy, determine tumor margins, and avoid eloquent brain structure. However, one of the most critical challenges is that neurosurgical guidance can be compromised due to soft-tissue deformations, also called brain shift. The causes of brain shift are often attributed to gravity-induced sag accompanied by loss of cerebrospinal fluid, swelling from edema, tissue volumetric contraction due to hyperosmotic drugs, and tissue resection. In order to account for tissue deformations, surgeons use intra-operative magnetic resonance (iMR), computed tomography (iCT), or ultrasound (iUS) imaging during surgery. However, the ionizing radiation of iCT, high cost of iMR, and poor image quality of iUS can compromise adoption, and performance. An alternative solution using intra-operative sparse data and a computational brain deformation model has been garnering increased attention. With respect to sparse data available in the intra-operative environment, two widely-investigated surface data acquisition techniques amenable to the OR are the laser range scanners (LRS) and stereoscopic computer vision techniques through the surgical microscope. Both of these can provide 3D cortical surface data and colorful texture of the surgical field of view. LRS is light-weighted and easily-operated in an operating room (OR), however, performing a single acquisition takes about half a minute requiring the surgery to be interrupted. To the contrary, the surgical microscope is continuously used during the process and provides high-resolution, consistent intra-operative data in real time without interrupting the surgical workflow. In this thesis, we propose an innovative approach to image guidance within the neurosurgical environment. More specifically, we hypothesize that the surgical operating microscope equipped

with two CCD cameras and an intra-operative stereo vision (iSV) system can be used not only as a complete locoregional (restricted to a localized region of the body) platform to achieve conventional image guidance but also to compensate for intra-operative brain shift, all realized without the use of conventional optical tracking technologies, i.e. a trackerless image guidance approach. Locoregional therapy refers to various minimally invasive therapeutic procedures. The approach centers around locoregional, stereo pair-driven, continuous registration strategies designed to match and possibly outperform the standard-of-care instrumentation of a separately optically-tracked surgical microscope.

1.2 Specific Aims

Specific Aim 1: Development of a mock craniotomy and brain shift simulator to evaluate methods for registration and tracking of mock brain shift for evaluation of a stereo-camera platform approach.

In this aim, We have built a novel craniotomy and cortical deformation simulation system that generates realistic soft tissue displacements. The five hemispherical divots visible outside the main circle can serve as a locoregional reference for capturing cortical surface information and maintaining a fixed coordinate reference. After creating a complete rigid body reference system on the craniotomy, the cortical surface can then be tracked, potentially automatically using computer vision methods designed for feature tracking. Tissue deformation can be computed by following over time the position of selected feature points.

Specific Aim 2: Translation of the stereo-pair technology to a stereo surgical microscope and validation of brain shift measurement using stereo-pair reconstructions.

In this aim, we have proposed a GUI-based system that integrates all necessary functionality for reconstructing FOV of stereopair or microscope cameras. The microscope is tracked via an attached tracking rigid body that facilitates the recording of the position of the microscope via a commercial optical tracking system as it moves during the proce-

dure. Point clouds, reconstructed under different microscope positions, are registered into the same space to compute the feature displacements. Using our mock craniotomy device, realistic cortical deformations are generated. The shift measurement can be validated by comparing to the measurement determined by the independent optically tracked stylus.

Specific Aim 3: Development of a novel planner that takes advantage of computer vision approaches to enable the planning of a patient's craniotomy during image-guided neurosurgery without the need of conventional tracking technologies.

Creating an image-to-physical registration system capable of planning a craniotomy without the need of conventional tracking technology is novel. In this aim, we will compare our novel approach to the standard-of-care swabbing with image-to-physical registration. This will be achieved using a trackerless image-guided surgical planning system based on an interactive extension on 3D slicer. The system provides a complete solution for pre-operative craniotomy planning without standard optical tracking. The proposed extension module has a user-friendly interface with multiple functionalities and easy to use. Also, the procedure of using our module is quite simple and efficient compared with conventional approach. It is flexible and can be done prior to surgery relatively easily. The novel features such as real-time updating of MR images, projecting tumor on surface, and real texture rendering, can facilitate the procedure of planning craniotomy.

Specific Aim 4: Demonstrate a proof-of-concept framework whereby deformation-corrected image guided neurosurgery can be performed without the need for conventional tracking and using stereo-pair microscope technology.

In this aim, we have proposed a pipeline for quantitatively measuring intra-operative movement of the cortical surface based on stereo reconstruction from an operating microscope without conventional tracking system. An initial reconstruction of the cortical surface was performed immediately after craniotomy through a stereo operating microscope.

Then, fluid was drained to simulate intraoperative brain shift and a second reconstruction was performed to track the subsequent motion of the cortical surface. At each stage, feature points were identified on the cortical surface and their ground truth positions were measured using an optical tracking system.

1.3 Impact

The goal of this thesis is to achieve a novel approach to image guided surgical microscopy without the use of cumbersome external trackers. In some respects, this thesis hypothesizes a new form of surgical workflow for conducting image guidance that uses the surgical microscope as a complete, and independent surgical guidance platform. If this is fully realized, it has the potential to provide the instrumentation aspect for a noninvasive soft tissue correction platform and quantify brain shift at the cortical surface.

Chapter II

BACKGROUND AND SIGNIFICANCE

2.1 Statistics

Cancer is a disease where abnormal cells uncontrollably invade or spread to other parts of the body and destroy body tissue. It has become one of the most serious health problems in the world, and it is the second leading cause of death in the United States. According to the data from American Cancer Society (ACE) [1] and American Brain Tumor Association (ABTA) [2], the estimated numbers of new cancer cases for 2017 are nearly 1.7 million (see Figure 2.1). Among these cases, nearly 80,000 new cases of primary brain and Central Nervous System (CNS) tumors were diagnosed in 2017. Based on severity, there are two types of tumors: benign and malignant. Malignant brain tumors contain cancer cells, can be proliferative, and can result in high morbidity and mortality. Nearly one-third of brain and CNS tumors are malignant [2]. The total number of people who are living with a primary brain and CNS tumor in the U.S. is 700,000. Approximately 17,000 patients failed to survive as a result of these tumors, which further indicates that brain and CNS tumors are serious clinical problem [2].

2.2 History

One aspect of the standard of care for brain tumor treatments is tumor resection surgery in which the tumor is located and resected while minimizing damage to surrounding healthy tissue. Surgery is the most common treatment for most benign tumors, while the malignant tumors might need radiation therapy and/or chemotherapy in addition to surgery. The goal of the surgical procedure is to remove as much of the tumor as possible without damaging healthy brain tissue in order to reduce symptoms and relieve the pain of patients. Historically, before medical imaging techniques were developed, the presence of the skull

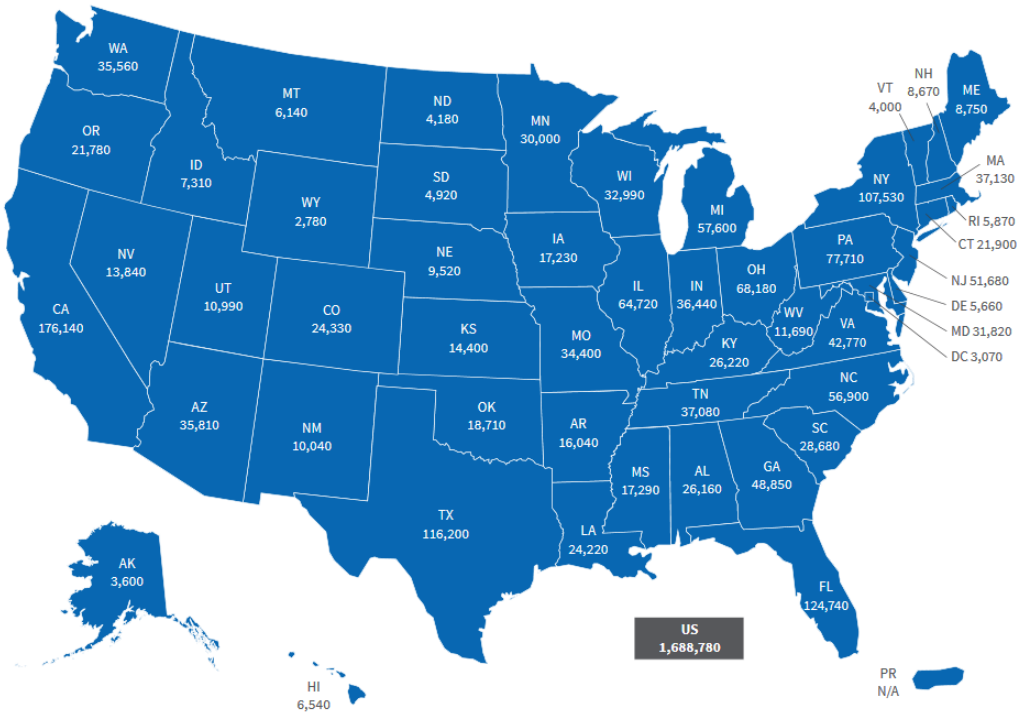

Figure 2.1: Estimated numbers of new cancer cases for 2017. (American Cancer Society).

made it very hard to locate the position of tumors. However, the development of modern neuroimaging techniques, for example, X-rays, provides surgeons visual hints to locate the tumors. The first image-guided surgery was performed just eight days after the discovery of X-rays. Later, the invention of contrast agent-enhanced computed tomography (CT) and magnetic resonance imaging (MRI) made the use of medical imaging a standard solution [3]. Moreover, the image sets went from two dimensional to three dimensional in space and time, which create the field of image-guided procedures (IGPs) that involves physical devices and related techniques [4].

2.3 Standard IGPs

Surgical planning is the first step in a tumor resection surgery. Accurately locating the position of tumor and choosing the best craniotomy area is crucial for the whole surgical procedure. In conventional brain tumor resection, surgeons rely on pre-operative magnetic

resonance imaging (pMRI) or pre-operative computed tomography (pCT) to localize the position of the tumor. Unfortunately, even the experienced surgeons have difficulties accurately planning the craniotomy. Surgical errors can happen. For example, the tumor may not be fully removed, or surrounding healthy brain tissue can be damaged. With the fast development of 3D computer vision techniques and image-guided neuro-navigation system, the computer-generated 3D head model and cortical surface structure extracted from MRI can give straightforward visualizations of where the tumor is located and how it relates to surrounding structures. One realization of image-guided neuronativation uses a rigid frame attached to the patient's skull to provide a reference for image-to-physical registration, which is usually uncomfortable or painful (see Figure 2.2). This cumbersome frame is visible on the pre-operative images which are used to do registration. This stereotactic methodology has been widely-used in electrode placement [5], local chemotherapy [6], radiation therapy [7], and transplanting tissues into the brain [8].

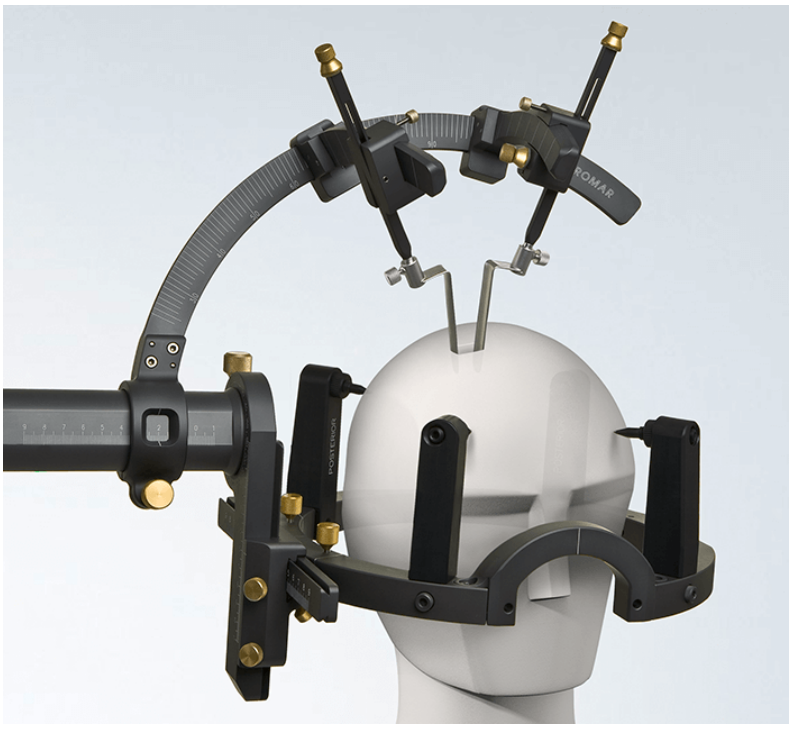

Figure 2.2: A rigid frame attached to the patient (from micromar.com).

Unlike classic stereotaxy where the physical position is determined by the preoperative images, researchers are thinking about tracking the surgical position in physical space and display it in image space. No matter how the implementations vary, there are three basic components that are necessary for conventional IGS:

- A three-dimensional localizer is needed to capture the physical position of patient.
- Image-to-physical registration is required to determine the relationship between physical space and image space.
- Displaying method to show the location in image space.

Later, researchers and surgeons were looking for frameless stereotaxy and interactive image-guided neurosurgery that is more convenient for patients [9, 10]. One method was to use an articulated arm [11]. The articulated arms using optical angle sensors are developed as localization system. However, the stiff arms between rotational joints made the arm too cumbersome.

Alternatively, other methods that could triangulate position have been used widely in image-guided procedures. The position of emitters can be accurately estimated by detector at know locations by the measurement of distance or angular information. The location and orientation of a rigid body that mounted three or more emitters can be uniquely determined in the space by detector. The problem of this localization system is that there must not be any obstacles between emitters and detector. Moreover, the detector is sensitive, which means sometimes it will not be very stable. In continuous recording, the localization and orientation data may become not applicable if the rigid body is placed in some extreme orientation. Although problems exist, optical tracking for localization is currently the predominant instrumentation used for image-guided procedures. Optical devices are provided by many commercial companies. Figure 2.4 shows an optical tracker Polaris Spectra and Figure 2.5 shows an optical stylus with optical reference targets shown, both from Northern Digital Inc. (Waterloo, Ontario, Canada). The tracking system represented by Figure 2.4

Figure 2.3: Articulated arm for minimally invasive surgery (from Unitrac).

and Figure 2.5 has a reported tracking accuracy of 0.25-0.3mm root mean square (RMS) for individual reference emitters [12].

Currently, surgeons use interactive image-guided neurosurgery to plan craniotomies. Typically, an image-to-physical registration is either performed by establishing correspondence using fiducials on the physical patient that can be digitized within the image volume and on the physical patient, or by swabbing the surfaces on the physical patient that can be registered to equivalent surfaces on the MR. Both use tools such as that shown in Figure 2.5. Once achieved, the stylus is then commonly held by the surgeon at key points on the scalp to estimate the area to plan craniotomy. By touching the head in various locations, the surgeon can determine the extent of the underlying tumor. Once achieved, the surgeon can then plan the craniotomy extent to ensure sufficient visualization of the tumor once the cranium is opened. Current commercial systems such as Brainlab Curve [13] and Medtronics Stealth [14] provide standard solutions for neurosurgery navigation. However,

Figure 2.4: Optical tracker Polaris Spectra (from NDI).

Figure 2.5: Optical stylus with optical tracker attached (from NDI).

these systems do not have mechanisms to account for nonrigid tissue deformations (known as brain shift), which commonly makes the navigation system not always accurate.

2.4 Brain Shift

Intra-operative soft tissue deformation, referred to as brain shift, compromises the application of current image-guided surgery navigation systems in neurosurgery. Earliest finding of deformation dates back to 1980s [15–17]. Kelly et al. [15] reported motion of brain structures while resection is performed. Both Koivukangas et al. [16] and Ryan et al. [17] claimed the discovery of brain deformation during the procedure but none of them had quantitative results. However, Hill et al. [18] accurately measured the deformation

of the dura and brain surface for 21 patients on their surgical resection. A sinking brain shift intra-operatively was measured approximately 1 cm. Later, Nabavi et al. [19] did a similar study with 25 patients in 0.2T intra-operative magnetic resonance imaging system, and they found surface deformations of approximately 2.5 cm. They also claimed that surface deformations occur mainly because of the cerebrospinal fluid (CSF) in the direction of gravity. Brain shift has been researched and measured for more than 20 years by a lot of groups [20–26].

2.5 Brain Shift Compensation

Both frame-based and frameless stereotaxy is based on a rigid-body image-to-physical registration, which works well on the initial phase of the surgical procedures. However, as the surgery is going on, brain shift is not accounted for by the navigational system, which makes the using of preoperative image data less accurate. Unfortunately, commercial IGS navigation systems do not have mechanisms to account for nonrigid tissue deformations, which commonly arise from cerebrospinal fluid drainage, tissue swelling due to edema, tissue contraction due to hyperosmotic drugs, or tissue retraction/resection [19]. Solutions like intra-operative magnetic resonance (iMR) imaging [27–34] (see Figure 2.6), intra-operative computed tomography (iCT) [35–41] (see Figure 2.7), and intra-operative ultrasound (iUS) [42–48] (see Figure 2.8) have been proposed to compensate for soft-tissue changes.

2.5.1 Intra-operative Magnetic Resonance (iMR)

To date, an iMR system is one of the most widely used solution for compensating brain shift. However, there are a number of disadvantages. First, an iMR system is a complex, expensive, and time-consuming addition to the operating room. The scanner as well as MR-compatible surgical instruments (non-metalic) are considerable financial burdens for most hospitals. Moreover, it requires equipment and devices that decrease the available

space of the operating room which also compromises the surgeon's access to the operating field. In some cases, either the patient will be moved to a specific room for the imaging or the iMR equipment will be moved (see Figure 2.6), which makes it almost impossible for frequent imaging. Special instruments, such as ferromagnetic implants, also need to be used. Another shortcoming of iMR is that the intra-operative MR images may be lower quality than preoperative counterparts because of the surgical environment and workflow.

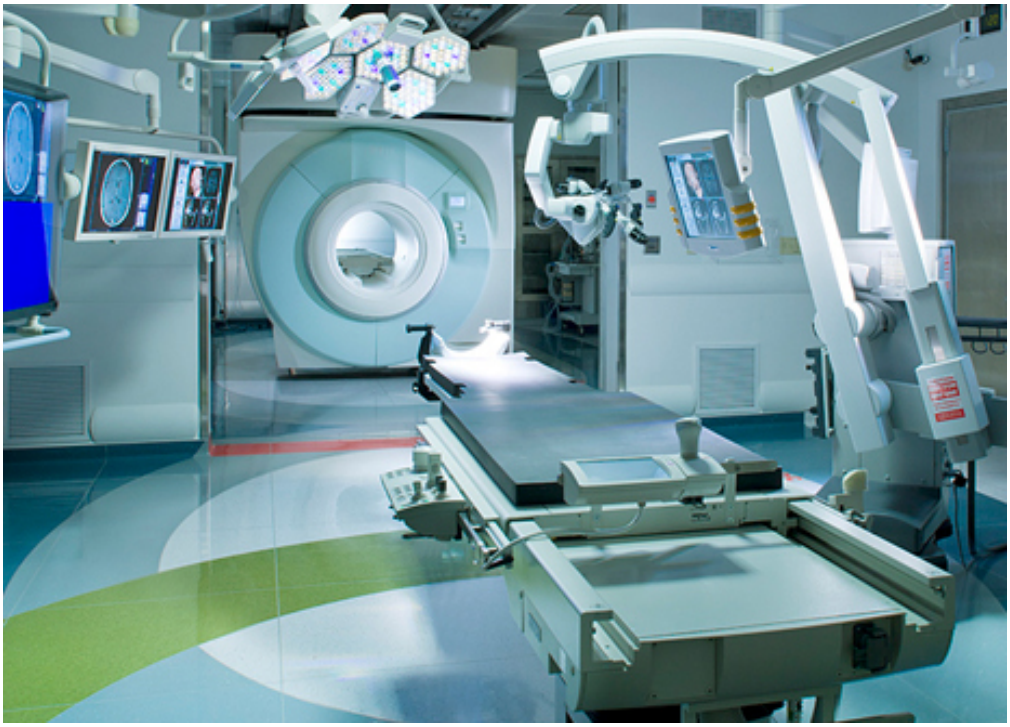

Figure 2.6: Intra-operative magnetic resonance (iMR) (from Colonialvision Healthcare).

2.5.2 Intra-operative Computed Tomography (iCT)

Similar to iMR, iCT is cumbersome, space-consuming, and too expensive for a number of hospital budgets. Both iCT and iMR have a limited number of scans possible during a case because the imaging process interrupts the surgical procedure. The lower soft tissue contrast of iCT makes it less useful for brain surgery. CT imaging perform well in spine surgery. Another major concern about using iCT system is the radiation. Repeated ex-

posure to X-ray radiation may be harmful to patients, which makes the iCT not generally adopted to correct for brain shift. The CT system is shown in Figure 2.7.

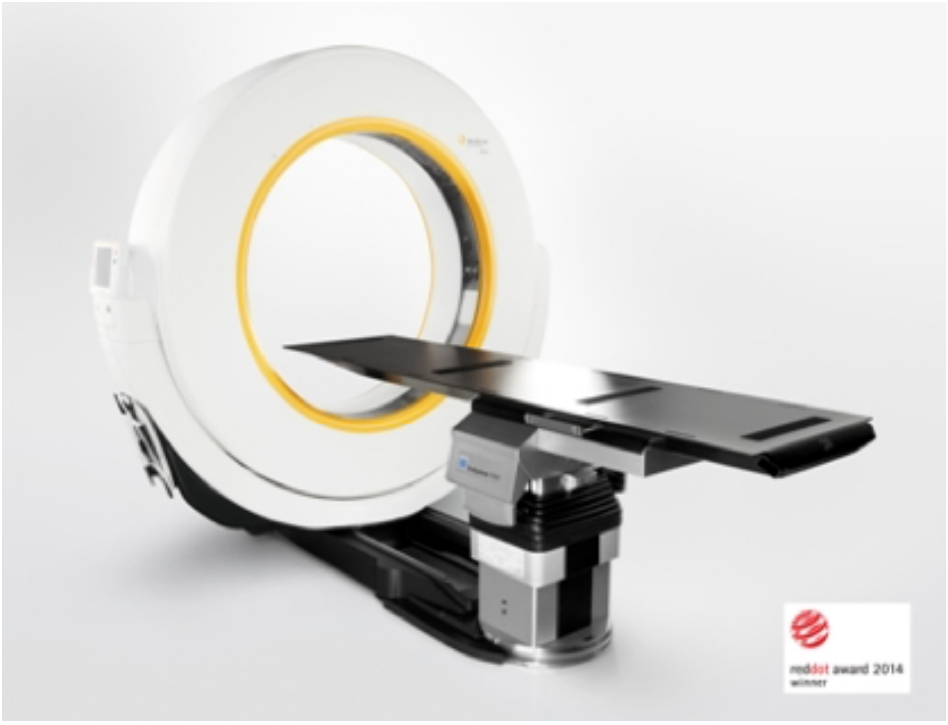

Figure 2.7: Intra-operative computed tomography (iCT).

2.5.3 Intra-operative Ultrasound (iUS)

Compared with iMR and iCT, iUS is low-cost, portable, ionizing radiation free, and compatible with existing surgical equipment. However, the main disadvantage compared to others is the poor image contrast and quality of iUS. In some cases, the tumor cannot be identified from surrounding tissues due to the low signal-to-noise ratio (SNR) during surgery. In addition, conventional iUS lacks 3D information and the tissue contact may also lead to additional cortical deformation. There are researchers that registered the iUS to preoperative MRI using vessel information [49], mutual information (MI) [50], or cross-correlation. Figure 2.8 shows a commonly-used ultrasound device (Philips Healthcare iU22 Ultrasound Machine).

Figure 2.8: Intra-operative ultrasound (Philips Healthcare iU22 Ultrasound Machine).

2.5.4 Model Updated Method

Deficiencies of iMR, iCT, and iUS have compelled researchers to look for alternatives. Another cost-effective method is to use sparse data acquired intra-operatively to drive a biomechanical model to update and register preoperative images to the intra-operative field. Sparse data, in this case, are those measurements of tissue deformations that can be obtained during the intra-operative procedure. While limited resolution MR, and CT could be considered a source of sparse data, conventionally, sources have resulted from those data modalities that could be routinely available and minimally disruptive to the surgical workflow, e.g. tracked pointer data, ultrasound imaging, laser range scanner data, or surgical microscope stereo-pair acquisitions. Once sparse data characterizing deformation is acquired, model-based compensation strategies can be constructed to account for positional changes of soft tissue. Miga et al. [51, 52] developed a finite-element model that can

be updated by using intra-operative data to estimate tissue motion. The proposed model-updated strategy also incorporated surgical effects such as the administration of mannitol, swelling, and the drainage of CSF [53]. Although the results were promising, more complex neurosurgical events of tissue retraction and resection were also desired. Later, Miga et al. [54, 55] proposed modeling strategy for retraction and resection based on previous conceptual framework [56]. This method was able to model a complete tumor resection as well as update preoperative images for use during surgery. The main concerns about the above strategies were in regards to time-consumption, and the complex prescription of boundary and internal forcing conditions. Dumpuri et al. [57, 58] proposed a constrained linear inverse model that can fit the sparse intra-operative data. The methodology allowed for extensive pre-computing of deformations which dramatically improved efficiency without compromising accuracy. Chen et al. [59] modifies Dumpuri's atlas-based solution to account for improved geometric specificity with the inclusion of dural septa. Later, Chen et al. [60] extended the approach of retraction and resection to make it equally amenable to fast computation. As the model-updated method is realized, one important aspect is the integration of that approach into the standard guidance platform technologies. Using the work above, Sun et al. [61] created a first realization of the novel integrated system for use in near real-time brain shift correction in OR. This realization consisted of a preoperative model development pipeline, a preoperative surgical planning GUI, and two intra-operative GUIs. The robust, simple, and minimally disruptive system is demonstrated to be a good alternative for iMRI system. This system was tested extensively in a recent 16-patient study by Miga et al. [62]. In the cases reported, brain shift was measured between 2.5-21.3 mm and after correction the mean remaining error was reported to be between 0.7-4.0 mm.

2.6 Surface Data Acquisition

While several possibilities exist, we have concentrated on data sources that are as minimally invasive to the intra-operative environment as possible. This has largely led us to

consider optical methods which can capture the changing shape of the brain surface quite easily. Laser range scanners (LRS) and stereoscopic microscopes are two alternative surface data acquisition techniques that meet this criterion.

2.6.1 Laser Range Scanners (LRS)

LRS is a lightweight, compact, and portable device that can be operated in the OR. It is equipped with a high-resolution camera that can acquire 3D cortical geometry and color image for texture. Miga et al. [63] registered the textured point cloud from LRS with preoperative MR using mutual information, they used both geometry and intensity information. Cash et al. [64] used both point-based and surface-based methods to register cortical surface from LRS to CT image volumes, and tracked with an optical localization system. They claimed the registration and tracking errors are consistently less than 2 mm. Similar works are in [65, 66]. Cao et al. [67, 68] compare different methods of image-to-physical such as skin marker point-based registration (PBR), face-based surface registration, cortical vessel-contour registration and so on. Ding et al. [69] proposed a semiautomatic method for the registration of intra-operative images with a LRS based on visualized vessels. Pheiffer et al. [70] designed and implemented a tracked single-CDD LRS that captured both geometric and color information with sufficient scanning and tracking accuracy (see Figure 2.9). However, performing a single LRS acquisition is more disruptive because it takes about 15 to 30 s and requires the surgical microscope to be moved away from the surgical field of view (FOV). Due to this, it is not common to perform acquisition every five or ten minutes due to the workflow inefficiency.

2.6.2 Stereovision (SV)

Both LRS and surgical microscope can be used in an operating room (OR) and generate three-dimensional (3-D) cortical surface cloud data as well as a texture map. Typically, the microscope is continuously used during the whole surgery. Thus, it can provide

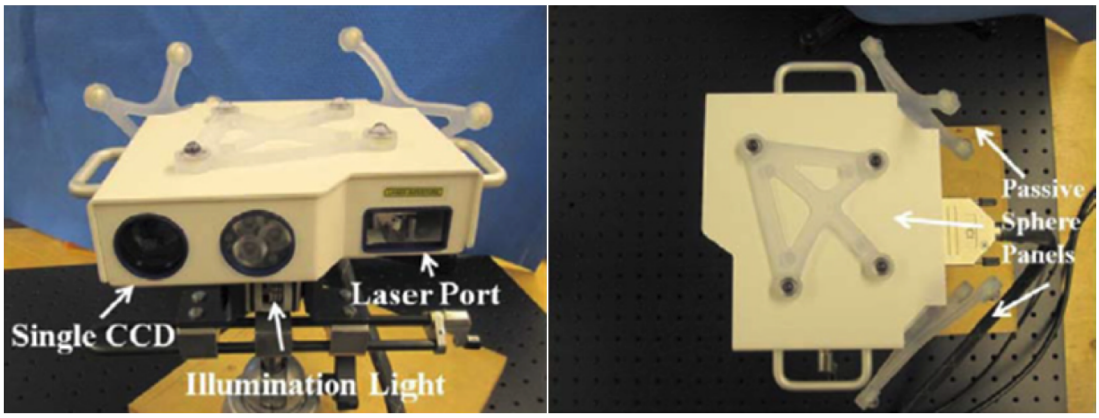

Figure 2.9: Laser range scanner (LRS) (Pheiffer et al., 2012).

high-resolution, consistent intra-operative information in near real time with very limited interruption to the surgical workflow (see Figure 2.10). Standard stereomicroscopes allow surgeons to appreciate the 3-D nature of their domain when performing surgery. This facilitates the physical execution of surgery. At the very beginning, Skrinjar et al. [71] proposed a compensation system guided by stereo-camera, and they also presented an algorithm to grow surface from stereo images with a pair of corresponding points in the left and right image as initial seed point [72]. Hai et al. [73–75] demonstrated that an operating surgical microscope coupled with stereo cameras can be used to efficiently estimate the cortical surface during surgery. Paul et al. [76] provided a surface registration method between distinct intra-operative surgical stages, which includes both textured cortical surface and video flow for intensity-based optimization. Ding et al. [77] tracked the cortical vessels in intra-operative microscope video sequences, and register them to the laser range images acquired during the procedure. Their method needs a certain amount of user interaction for selecting vessels. Ji et al. [78, 79] applied an optical flow (OF) motion tracking algorithm to register cortical surface in projection images. Different from [77], the optical flow algorithm does not need continuous video streaming or individual feature identification/tracking, but overlapping regions and physical feature correspondences in the projection images are necessary. Kumar et al. [80, 81] developed a non-contact intra-operative

microscope-based 3D digitization system to acquire video streams, estimate magnification, and reconstruct the 3D point cloud in near real-time. Since the microscope is not optically tracked, the transformations needed to compute tissue deformation cannot be estimated. Yang et al. [82] proposed a stereovision-based integrated system for point cloud reconstruction and simulated brain shift validation. With respect to tracked microscopes, once calibrated, these will typically track the focal point of the scope in 3-D space. This allows one to probe the tissue one point at a time to determine the associated imaging data.

Figure 2.10: Surgical microscope (Kumar et al., 2013) and stereo-pair cameras.

Chapter III

A NOVEL CRANIOTOMY SIMULATION SYSTEM FOR EVALUATION OF STEREO-PAIR RECONSTRUCTION FIDELITY AND TRACKING

3.1 Summary of Contributions

In this chapter, we have proposed and demonstrated a craniotomy simulation device that permits simulating realistic cortical displacements designed to measure and validate the proposed intra-operative cortical shift measurement systems. The device permits 3D deformations of a mock cortical surface which consists of a membrane made of a Dragon Skin high performance silicone rubber on which vascular patterns are drawn. We then use this device to validate our stereo pair-based surface reconstruction system by comparing landmark positions and displacements measured with our systems to those positions and displacements as measured by a stylus tracked by a commercial optical system. Our results show a 1mm average difference in localization error and a 1.2 mm average difference in displacement measurement. These results suggest that our stereo-pair technique is accurate enough for estimating intra-operative displacements in near real-time without affecting the surgical workflow.

3.2 Abstract

Brain shift compensation using computer modeling strategies is an important research area in the field of image-guided neurosurgery (IGNS). One important source of available sparse data during surgery to drive these frameworks is deformation tracking of the visible cortical surface. Possible methods to measure intra-operative cortical displacement include laser range scanners (LRS), which typically complicate the clinical workflow, and recon-

This chapter has been published in SPIE 9786, Medical Imaging 2016: Image-Guided Procedures, Robotic Interventions, and Modeling, 978612 (March 18, 2016 in San Diego, CA); doi:10.1117/12.2217301.

struction of cortical surfaces from stereo pairs acquired with the operating microscopes. In this work, we propose and demonstrate a craniotomy simulation device that permits simulating realistic cortical displacements designed to measure and validate proposed intra-operative cortical shift measurement systems. The device permits 3D deformations of a mock cortical surface which consists of a membrane made of a Dragon Skin high performance silicone rubber on which vascular patterns are drawn. We then use this device to validate our stereo pair-based surface reconstruction system by comparing landmark positions and displacements measured with our systems to those positions and displacements as measured by a stylus tracked by a commercial optical system. Our results show a 1mm average difference in localization error and a 1.2mm average difference in displacement. These results suggest that our stereo-pair technique is accurate enough for estimating intra-operative displacements in near real-time without affecting the surgical workflow.

Keywords: Craniotomy simulation, brain shift, intra-operative imaging, stereo-pair reconstruction, tracking, accuracy

3.3 Introduction

In traditional craniotomy, surgeons rely on pre-operative images, e.g., computed tomography (CT) and magnetic resonance imaging (MRI), to plan and execute the procedure. The development of computer modeling strategies permits addressing a major problem, which is the deformation of the brain that occurs as soon as the dura is opened. In the recent past, a method that permits updating preoperative image volumes to compensate for brain shift using sparse data acquired intra-operatively has been proposed [54]. It builds a finite-element model that incorporates tissue retraction and resection with high accuracy. The intra-operative imaging is used to update the preoperative image to evaluate the tissue deformation as well as guiding the neuro-navigation. The acquisition of intra-operative information that is required to drive these model-based compensation methods can vary in a number of ways, e.g. intra-operative MRI, LRS or stereo-pair images, all of which en-

hance the visualization of brain deformation during the surgery. However, there is always a tradeoff between obtaining more information and reducing the acquiring operation time. Intra-operative MR scanners are not common because they require operating rooms (OR) that are specially equipped. They also typically require moving the patient or equipment thus complicating the procedure and affecting the surgical workflow [31, 83]. LRS takes advantages of its lightweight and compact size which can be operated in OR. At our institution we have employed a tracked LRS that is equipped with a high-resolution digital camera that can acquire a 3D cortical surface as well as a color image of the field of view [63, 67, 84–86]. However, performing one LRS surface sweep takes about one minute during which the surgery needs to be interrupted. It is almost impossible to perform acquisition procedure every five minutes or ten minutes because of the inefficiency. In work [63, 67, 84–86], their solution is applying data collection using LRS only at the beginning and ending stage of the surgery, estimating the displacement of features on cortical surface between two LRS sweeps. Even though this operation affects little on the whole process of surgery, a substantial amount of intra-operative information is lost. Another method that uses stereo-pair images obtained from stereo-pair cameras or directly from microscope embedded came ras can also potentially provide 3D cortical surfaces in close to real time without disrupting the surgical workflow. In [80, 81], work has been done to evaluate the accuracy of stereo cameras but it was done on static phantoms. In this work, we evaluate the accuracy of stereo-pair-based surface reconstruction algorithms with a device we have designed to generate realistic cortical deformations. The remainder of this chapter describes both our device and its use for validating our stereo-pair method.

3.4 Methods

Stereo-pair images or video streams that are necessary for camera calibration and 3D point cloud reconstruction are acquired using software we have developed in-house for this purpose [81]. Our novel craniotomy simulation device shown in Figure 3.1 is designed to

permit in-plane stretching as well as out-of-plane deformation of a membrane to generate simulated brain shift. Ground truth displacements are measured with an optically tracked probe also shown in Figure 3.1. The membrane deformation computed using our camera-based systems is compared to displacements measured with the probe to assess its accuracy.

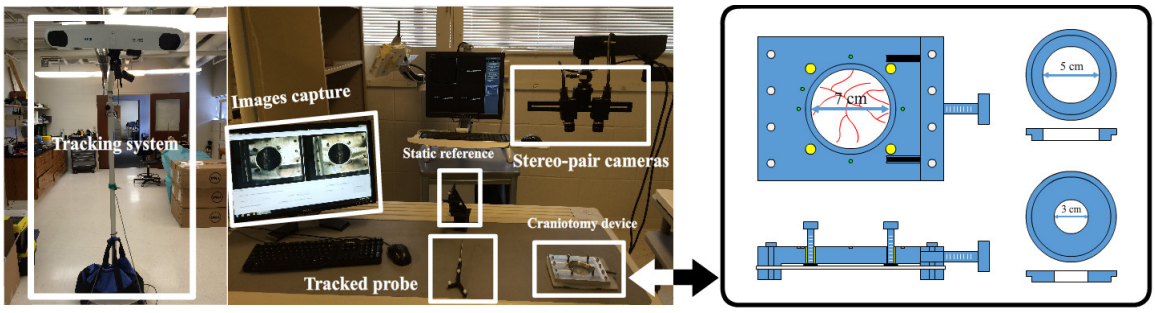

Figure 3.1: System overview and craniotomy device design .

3.4.1 Apparatus

As shown in Figure 3.1, our experimental setup consists of a pair of cameras, a monitor that shows the captured images, an optical tracking system with a static reference and a stylus, and our novel craniotomy simulation device. We use two Grasshopper IEEE-1394b (FireWire) digital cameras (GRAS-20S4C-C), which are equipped with a Sony ICX274 CCD with a resolution of 1624 x 1224. These cameras provided by Point Grey Research, Inc. (Richmond, British Columbia, Canada) can acquire videos at 30 frames per second (FPS). The optical tracking system is a Polaris Spectra manufactured by Northern Digital, Inc. (Waterloo, Ontario, Canada). It is used to measure the ground-truth displacement manually with a tracked probe. The tracking accuracy for a Polaris Spectra is reported to be 0.25-0.3 mm RMS for an individual marker tracked within its working volume. With respect to stylus point localization, the accuracy of these tools is typically configuration dependent and is estimated to be approximately 0.5 mm in our case [87]. Our novel device is designed to simulate realistic displacements occurring during surgery. As Figure 3.1 shows,

it has two circular rings inserts that can be placed in the device aperture to simulate different craniotomy sizes (at our institution the size of the craniotomy can vary substantially from surgeon to surgeon). The five hemispherical divots visible outside the main circle serve as fiducial points to register the mock cortical surface phantom device. The four screws on each side of the device act to clamp the silicon membrane. Using a lead-screw mechanism, the device clamp on the right side can be extended such that a systematic and even stretch of the silicon membrane can be imparted. This provides two cortical deformation behaviors typically seen in operating rooms, namely, change in lateral interpoint distances, and translation of some cortical surface laterally such that new structures become visible and some initially visible structures become obstructed with a translation under the bone. In addition to lateral motion, four additional medium-size screws are placed around the mock craniotomy and can push the membrane down more than 1cm to produce deformation patterns that are more complex than just stretching. More specifically, brain sag often manifests as a withdrawal of the brain surface into the cranium on average of 1cm (although it depends on patient head orientation). The membrane is marked with a realistic mock cortical vessel pattern and is made of Dragon Skin high performance silicone rubber.

3.4.2 Camera Calibration

Here, we rely on a classical and widely-used method [88] for camera calibration. This technique requires acquisition of a series of images from a calibration pattern. We have used a planar checkerboard pattern that has 8 by 6 internal corners with each square of size 13.5 mm as shown in Figure 3.2. About eighteen pairs of images acquired from the calibration pattern in various positions and orientations are required to calibrate the images. To facilitate acquisition, we have developed a user-friendly graphical user interface (GUI) [89]. It is designed to work on all USB, Point Grey Research or other IEEE-1394b (FireWire) digital cameras. h detected corners and stereo rectification pair with epipolar line draw

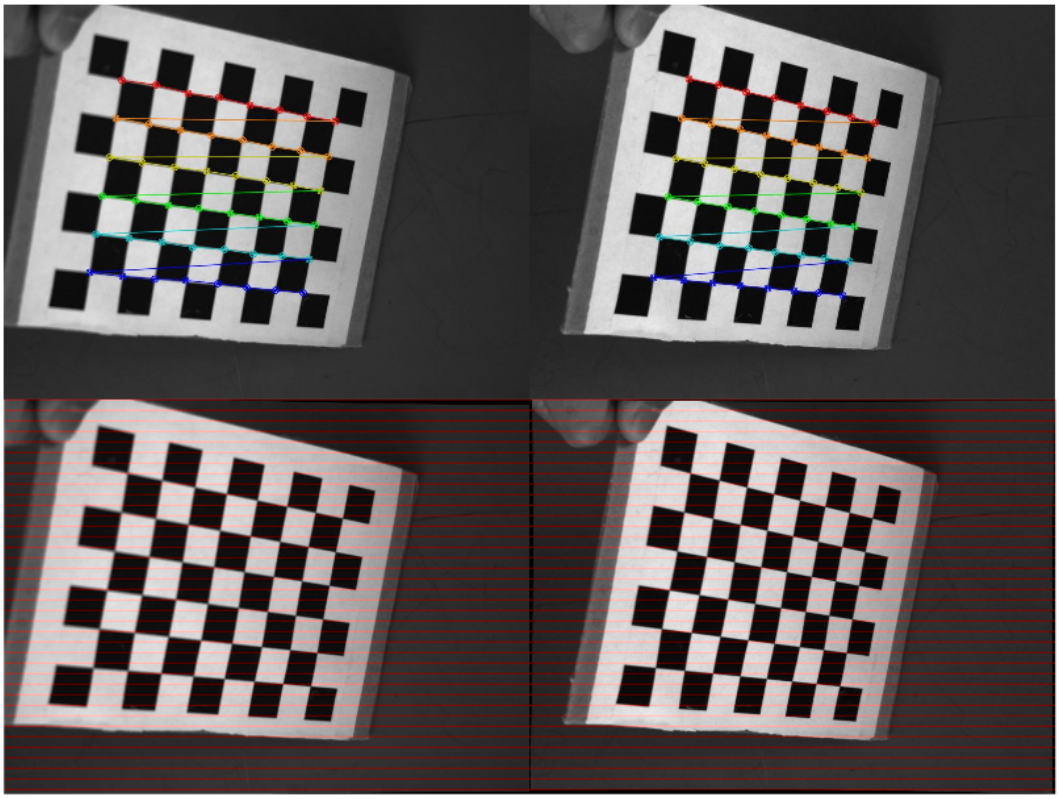

Figure 3.2: Checkerboard with detected corners and stereo rectification pair with epipolar line drawn in red.

In order to compute intrinsic and extrinsic parameters of stereo-pair cameras, the epipolar geometry based on pinhole models is built to search for corresponding points in stereo matching. In Figure 3.3, Image plane π_1 and π_2 are captured by two cameras whose center locates at point C_1 and C_2 respectively. The image point x_1 and x_2 represents the space point X in their image coordinates, which together are coplanar on epipolar plane pi as well as camera centers C_1 and C_2. The intersection of epipolar plane π with image plane π_1 and π_2 is epipolar line l_1 and l_2, while epipole e_1 and e_2 is the intersection point of joining the camera centers with the image planes. The fundamental matrix [90] is defined by mapping a point in left image to its corresponding epipolar line of right image, which can also write algebraic representation as:

$$l_2 = F\, x_1 \tag{III.1}$$

The point lying on line satisfies:

$$x_2{}^T\, l_2 = 0 \tag{III.2}$$

Substitute equation (1) in equation (2), then

$$x_2{}^T\, F\, x_1 = 0 \tag{III.3}$$

Equation (IV.1) demonstrates that can also match a point from left image to the right one. The calibration image pairs provide a number of correspondences which is used to solve F by a least squares method [88]. The accuracy of calibration procedure can be checked by computing the distance between the corresponding corners and the estimated epipolar lines because we know the corresponding corner lies on the epipolar line in theory.

3.4.3 Three-dimensional Reconstruction

The reconstruction procedure reprojects 2D image points to physical world positions. As shown in Figure 3.4, we have a parallel-aligned stereo pair π_1 and π_2 that are coplanar and collinear with each other. The principal rays from camera centers C_1 and C_2 perpendicular to the image planes intersect the planes on the principal points p_1 and p_2, which have been rectified to the same pixel coordinates in their respective left and right images. Image point x_1 and its corresponding point x_2 are collinear. The coordinates of point x_2 in right image is exactly the same as point x_2' in the left image, so the disparity d is defined as:

$$d = x_1 - x_2 \tag{III.4}$$

The depth Z of world point X can be computed by similar triangles using:

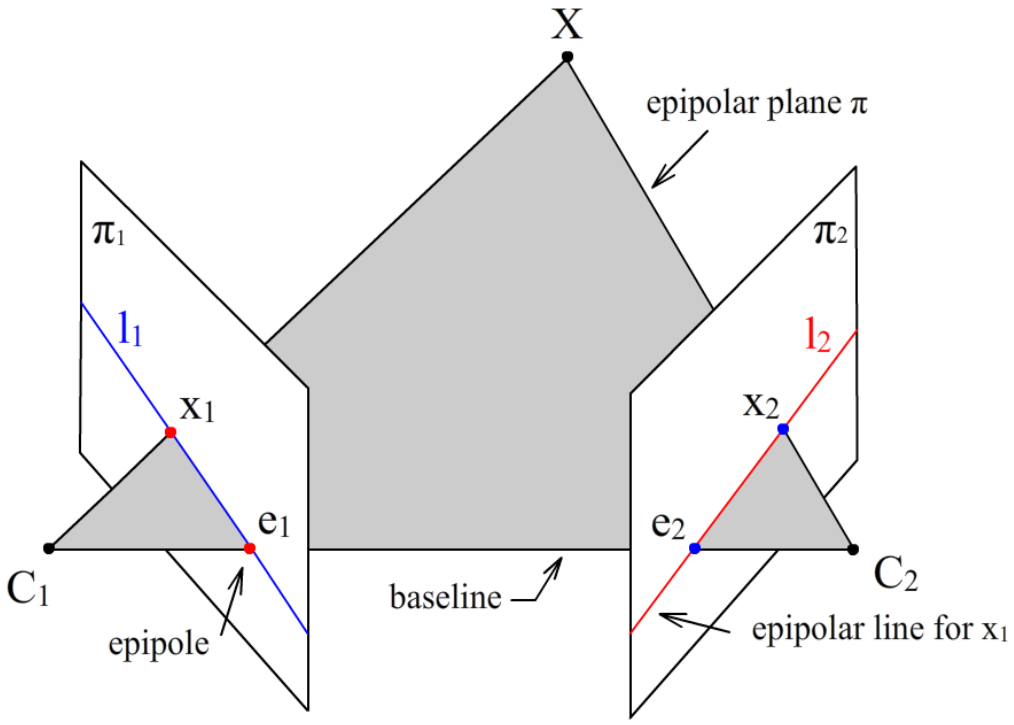

Figure 3.3: Epipolar geometry.

$$\frac{T-d}{T} = \frac{z-f}{f} => Z = \frac{fT}{d} \tag{III.5}$$

In Equation III.5, T is the horizontal distance between two camera centers C_1 and C_2, and f is the focal length. For computation efficiency, the reprojection matrix Q is defined as below:

$$Q = \begin{bmatrix} 1 & 0 & 0 & -c_{x1} \\ 0 & 1 & 0 & -c_{y1} \\ 0 & 0 & 0 & f \\ 0 & 0 & -\frac{1}{T} & \frac{c_{x1}-c_{x2}}{T} \end{bmatrix} \tag{III.6}$$

Here, point (c_{x1}, c_{y1}) is the principal point in left image, while c_{x2} is the x coordinate of

the principal point in the right image. In frontal parallel configuration of stereo pair, the two principal rays intersect at infinity, and then $c_{x1} = c_{x2}$, which makes the bottom right corner term in (IV.2) equal zero. The reprojection matrix Q reprojects a 2D homogeneous point (associated with disparity d) into a 3D point $(\frac{X}{W}, \frac{Y}{W}, \frac{Z}{W})$ in physical world by the following mapping:

$$Q \begin{bmatrix} x \\ y \\ d \\ 1 \end{bmatrix} = \begin{bmatrix} X \\ Y \\ Z \\ W \end{bmatrix} \tag{III.7}$$

In practice, the camera pair is seldom placed perfectly parallel-aligned, we need to mathematically rectify the left and right images into a coplanar and collinear configuration as well as synchronize two cameras in order to capture the image pair at the exact same time. There are mainly two different methods for rectification: one is Hartley's algorithm [91], which tries to find homographies that map the epipoles to infinity using just the fundamental matrix F. However, this method lacks sense of image scale because reconstruction result only depends on a projective transform, which means 3D objects with different scales may have the same 2D coordinates. The second one is Bouguet's algorithm [92, 93], which is a completed and simplified version based on [88, 94] that takes advantage of two calibrated cameras rotation and translation parameters to minimize reprojection distortions as well as maximizing the view overlap area. Here, we choose Bouguet's algorithm in our implementation.

In Figure 3.5, R is the rotation matrix from right image coordinates to the left one, then rectified rotation matrix R_1, R_2 and rectified camera matrix M_1, M_2 are computed by rotating the two principal rays parallel to each other and aligning the epipolar lines horizontally (as the green line shows). Known these matrices, the rectification map is constructed to rectify the image pair. After rectification is done, the disparity map is computed by find-

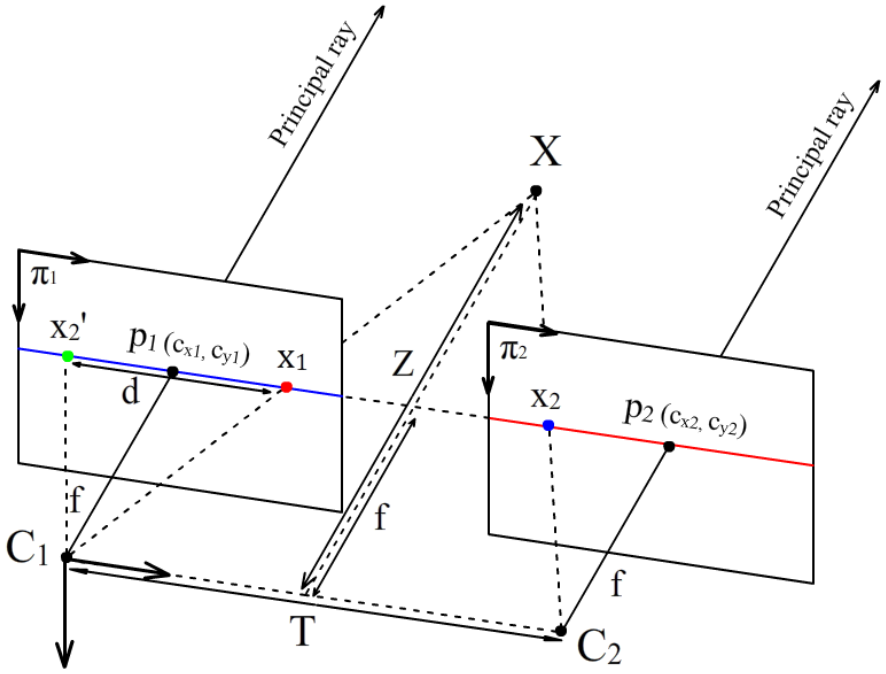

Figure 3.4: Reprojected triangulation of rectified stereo pair, and depth Z can be calculated by similar triangles.

ing the differences of x coordinates of the same features in rectified left and right images by applying block matching (BM) or semi-global block matching (SGBM) or other methods [95]. 3D point clouds are then reconstructed directly from the disparity map based on equation (IV.2) and (IV.3) using the Open Computer Vision Library (OpenCV) SDK [96].

3.4.4 Experiment Prototype

The accuracy of our camera-based surface reconstructing and tracking system was tested with our craniotomy simulation device as follows (also see Figure 3.6):

1. Calibrate the stereo-pair cameras using the checkerboard calibration pattern.

2. Place the mock cortical surface deformation device with clamped mock cortical sur-

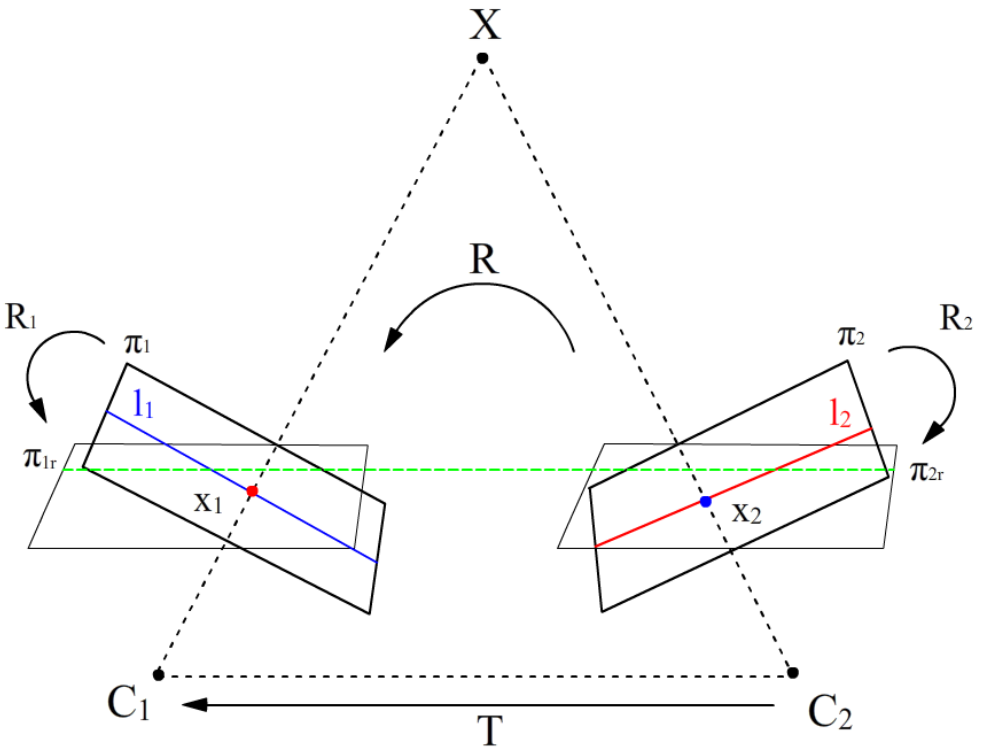

Figure 3.5: Mathematically adjust the stereo pair to a perfectly undistorted, row-aligned, frontal parallel configuration.

face under the camera pair, acquire images, and subsequently create a 3D point cloud.

3. Record the real world position of the five fiducial points around the mock craniotomy, as well as of 8 visible vessel target features on the membrane using the independent optically tracked stylus (one feature may disappear after stretching the device).

4. Take the device out of the field of view, and apply a stretch using the screw mechanism (Figure 3.6 b), then repeat steps 2 and 3.

5. Take the device out of the field of view, and apply the brain-sag simulated retreat of the mock brain surface using the four screws around the craniotomy (Figure 3.6 c), and then repeat step 2 and 3.

6. Once completed, the data above reflect three sets of optically digitized points (div-

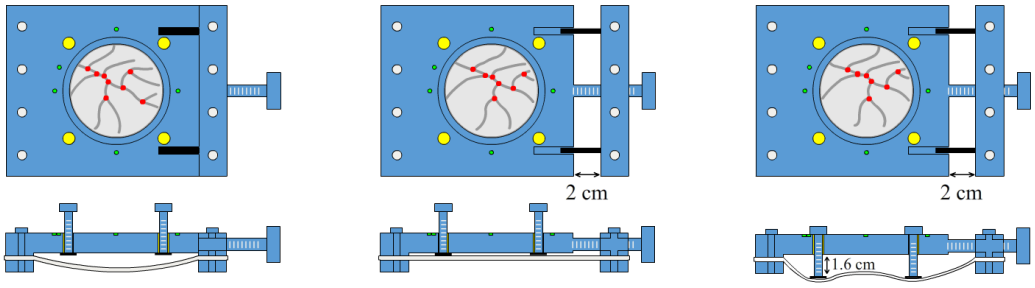

Figure 3.6: Experiment prototype of three states: baseline, stretch and stretch as well as sag.

ots and vessels) using the stylus, as well as three point clouds. Using the divots identified in the image, all data are registered to a common space (here, all datasets are registered to the baseline dataset acquired with the optical tracker). Position and displacement of vessel bifurcations measured by stylus and stereo pairs are then compared.

3.5 Results

By computing the absolute distance between detected checkerboard corners and their epipolar lines on the other image we estimate our calibration error to be 0.3 pixels. A 3D point cloud of the device reconstructed from a stereo pair as well as the disparity map is shown in Figure 3.7. Table III.1 reports differences in position and displacement for each landmark and each membrane state. Both the stereovision and tracking displacement is computed based on baseline state. Note that the row of target 1 is missing because stretching the membrane makes the feature near the border go out of view, which is reasonable since it may happen in real craniotomy. Mean position errors are approximately 1mm and mean displacement errors slightly above 1mm. These errors include the localization error associated with the optical tracking system and the error associated with registering the real world and the image spaces. By comparing known distances between landmarks on

the physical phantom and distances measured with the tracking system, we estimate the localization error of the optical stylus to be approximately 0.5mm, which is consistent with theoretical results [87]. A more rigorous study that will permit to estimate the localization error at the target points for our landmark and stylus configuration is ongoing. The displacement of the landmarks measured with the tracking system is shown on the 2D images in Figure 3.8 (top panels) and the corresponding 3D clouds are shown in the bottom panels. Red points indicates the position of eight features in baseline state, while green and yellow ones show their new places in stretch and stretch plus sag state respectively. We notice that there are only seven green and yellow points because of the stretching operation. The white arrows present the direction and magnification of the displacement from the baseline to each new state.

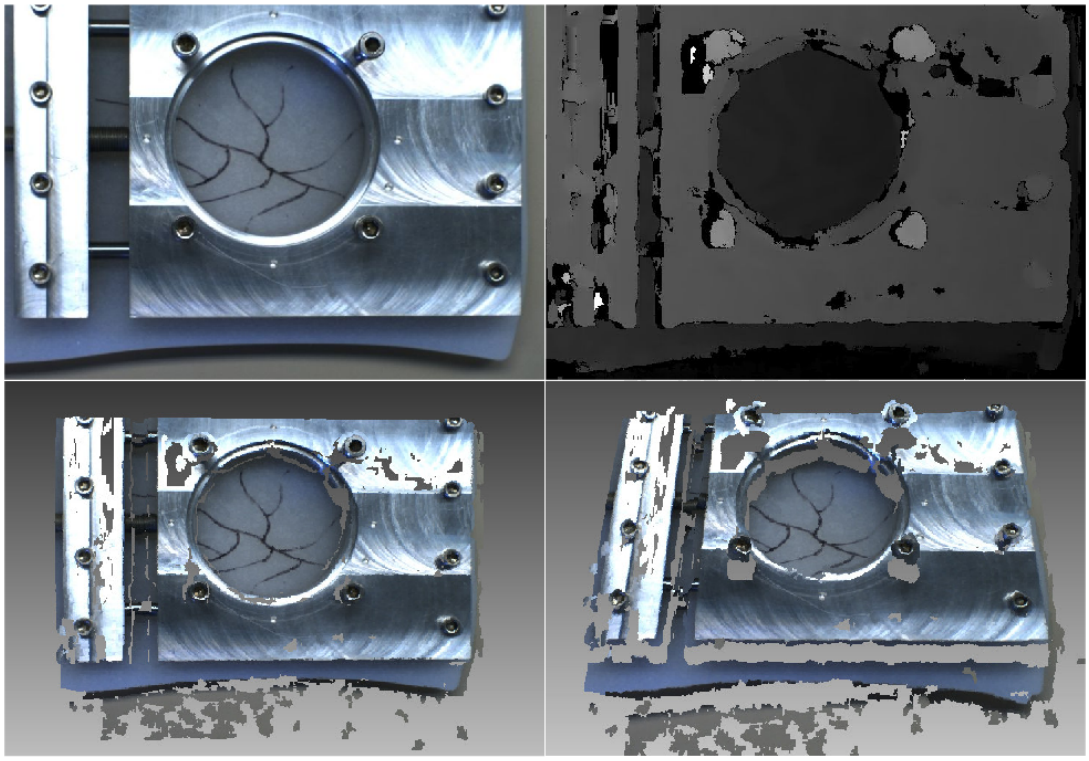

Figure 3.7: Craniotomy device with disparity image and point cloud reconstruction.

	Category	Stereovision Disp.	Tracking Disp.	Disp. Err	Local. Err
T2	Baseline	–	–	–	0.97
	Stretch	[-11.9 -0.3 -5.9]	[-11.8 -1.2 -5.3]	1.09	0.40
	Stretch+Sag	[-11.9 -0.6 -1.0]	[-11.4 -1.1 -0.7]	0.73	0.61
T3	Baseline	–	–	–	0.82
	Stretch	[-10.0 0.2 -6.2]	[-9.6 -1.4 -6.3]	1.64	0.96
	Stretch+Sag	[-10.0 -0.2 -1.1]	[-9.8 -1.2 -1.8]	1.19	0.84
T4	Baseline	–	–	–	1.29
	Stretch	[-9.1 0.9 -6.0]	[-8.1 -1.2 -6.2]	2.33	1.25
	Stretch+Sag	[-9.6 0.3 -0.5]	[-9.0 -1.29 -1.3]	1.80	0.84
T5	Baseline	–	–	–	1.30
	Stretch	[-8.5 0.7 -5.8]	[-9.0 -0.3 -5.5]	1.16	1.41
	Stretch+Sag	[-8.5 0.08 -0.05]	[-8.9 -0.2 -0.4]	0.53	1.21
T6	Baseline	–	–	–	1.21
	Stretch	[-6.7 1.4 -5.3]	[-6.3 -0.4 -5.6]	1.87	1.86
	Stretch+Sag	[-6.8 0.7 0.9]	[-6.4 0.03 1.3]	0.81	1.01
T7	Baseline	–	–	–	0.72
	Stretch	[-9.8 -0.7 -6.3]	[-9.4 -0.7 -5.6]	0.79	0.87
	Stretch+Sag	[-9.8 -1.1 -1.3]	[-9.4 -0.7 -1.2]	0.49	0.96
T8	Baseline	–	–	–	1.83
	Stretch	[-13.2 0.9 -5.0]	[-14.4 1.0 -4.3]	1.32	0.60
	Stretch+Sag	[-13.1 0.2 0.5]	[-14.3 0.4 1.7]	1.72	0.12
ME	–	–	–	1.24	0.99

Table III.1: Displacement, error of displacement and error of localization between stereovision and tracking.

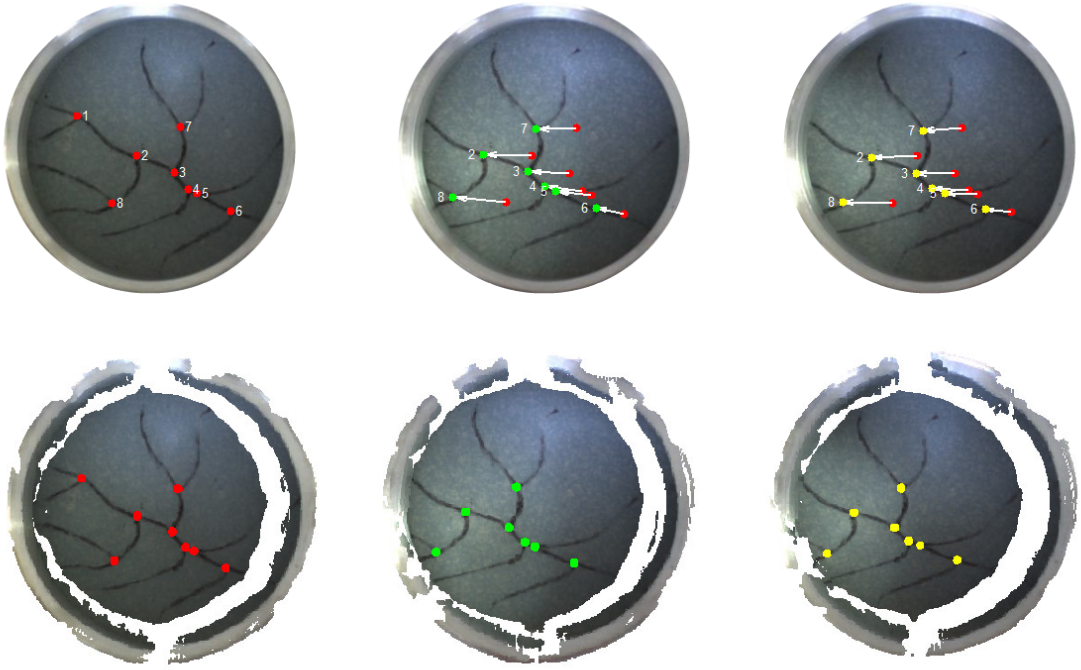

Figure 3.8: Displacement trajectories in 2D image (top) and corresponding 3D clouds (bottom).

3.6 Conclusions

We have built a novel craniotomy and cortical deformation simulation system that generates realistic soft tissue displacements. The device allows for measurements and comparisons between stereo-pair reconstructions and commercial tracking systems. The device can simulate known behaviors within the operating room theatre (namely lateral shift and sag). The different inserts designed allow for variable craniotomy size analysis that range from 3 to 7 cm. The comparison results indicate that the use of stereo-pair images captured from stereo cameras has the potential to gather valid intra-operative information without disrupting the surgery. This is the prerequisite for us to compensate brain shift using stereo-pair reconstruction fully-automatically in OR. We should note that while several groups are pursuing microscope driven stereo-pair cortical shift estimation, there is still a paucity of

validation with respect to independent tracking method comparisons under controlled conditions. To our knowledge, the construction of a device like this is completely novel. To sum up, the purpose of this work was to evaluate the stereo-pair reconstruction fidelity as well as the manually-designated brain shift tracking with stereo pair. Results we have obtained suggest that the deformation computed from 3D cortical vessel surface similar to the deformation measured with the ground truth tracking system. Our future work is to use stereovision as a substitute for LRS in our preoperative and intra-operative computational pipeline for brain shift correction [61].

Chapter IV

STEREOVISION-BASED INTEGRATED SYSTEM FOR POINT CLOUD RECONSTRUCTION AND SIMULATED BRAIN SHIFT VALIDATION

4.1 Summary of Contributions

In this chapter, we have proposed a GUI-based system that integrates all necessary functionality for reconstructing FOV of stereo-pair or microscope cameras including (1) capturing stereo-pair images or video streams, (2) extracting checkerboard corners, (3) calibrating stereo-cameras, (4) computing disparity, and (5) displaying point clouds. Moreover, the parameters associated with the disparity computation can be modified in an interactive GUI to improve the results. This reconstruction system is functional, user-friendly, and requires only minimal prior knowledge. By applying image-to-physical space registration, the stereoscopic microscope can be tracked and freely moved without disrupting the surgical procedure. The reconstruction accuracy and displacement comparison results suggest that this system could be used to gather cortical data to measure and compensate for brain shift during IGS. This would extend the capability of conventional navigation system.

4.2 Abstract

Intra-operative soft tissue deformation, referred to as brain shift, compromises the application of current image-guided surgery (IGS) navigation systems in neurosurgery. A computational model driven by sparse data has been proposed as a cost-effective method to compensate for cortical surface and volumetric displacements. In this work, we present a mock environment developed to acquire stereo images from a tracked operating microscope and to reconstruct 3D point clouds from these images. A reconstruction error of 1 mm is estimated by using a phantom with a known geometry and independently measured

This chapter has been published in J. Med. Imag. 4(3), 035002 (2017), doi: 10.1117/1.JMI.4.3.035002.

deformation extent. The microscope is tracked via an attached tracking rigid body that facilitates the recording of the position of the microscope via a commercial optical tracking system as it moves during the procedure. Point clouds, reconstructed under different microscope positions, are registered into the same space to compute the feature displacements. Using our mock craniotomy device, realistic cortical deformations are generated. When comparing our tracked microscope stereo-pair measure of mock vessel displacements to that of the measurement determined by the independent optically tracked stylus marking, the displacement error was approximately 2mm on average. These results demonstrate the practicality of using tracked stereoscopic microscope as an alternative to LRS to collect sufficient intraoperative information for brain shift correction.

Keywords: Brain shift, stereoscopic microscope, intra-operative imaging, stereopsis, reconstruction, tracking, accuracy.

4.3 Introduction

Image-guided surgery (IGS) [4] provides a standard of care platform for guiding surgeons during brain tumor resection. Unfortunately, commercial IGS navigation systems do not have mechanisms to account for non-rigid tissue deformations which commonly arise from cerebrospinal fluid drainage, tissue swelling due to edema, tissue contraction due to hyperosmotic drugs, or tissue retraction/resection [19]. Solutions like intraoperative magnetic resonance (iMR) imaging [27], intraoperative computed tomography (iCT) [36], and intraoperative ultrasound (iUS) [45] have been proposed to compensate for soft-tissue changes. However, deficiencies like ionizing radiation of iCT, high cost of iMR, and poor image contrast/quality of iUS have compelled researchers to look for alternatives. Another cost effective method is to use sparse data acquired intraoperatively to drive a biomechanical model to update and register preoperative images to the intraoperative field [54]. Laser range scanners (LRS) and stereoscopic microscopes are two widely used surface data acquisition techniques [63, 81]. Both devices can be used in an operating room (OR) and

generate three-dimensional cortical surface cloud data as well as a texture map. Typically, the microscope is continuously used during the whole surgery. Thus, it can provide high-resolution, consistent intraoperative information in near real-time with very limited interruption to the surgical workflow. Performing a single LRS acquisition is more disruptive because it takes about 15-30 seconds and requires the surgical microscope to be moved away from the surgical field of view.

Standard stereo-microscopes allow surgeons to appreciate the 3D nature of their domain when performing surgery. This facilitates the physical execution of surgery. With respect to tracked microscopes, once calibrated, these will typically track the focal point of the scope in 3D space. This allows one to probe the tissue one point at a time to determine associated imaging data. If one wanted to measure the optical field quickly, such as in measuring the distribution of deformations on the brain surface, the process of refocusing the focal point for each measurement would be highly impractical. The proposed work herein is focused at a tracked stereo-pair reconstruction; or put more simply, the system herein is focused at measuring the whole visible brain surface dynamically throughout surgery capturing multi-dimensional displacements. These measurements may subsequently be used within nonrigid image-to-physical registration methodologies to account for soft-tissue brain shift which can compromise neuronavigation systems. The proposed tracked stereo scope solution allows for those measurements potentially to be continually captured throughout surgery without disrupting workflow, and with optimal visibility of the tissue of interest. In recent work, we demonstrated using position-fixed stereo-pair cameras for surface measurements. This work used two identical Grasshopper digital cameras produced by Point Grey Research, Inc. (Richmond, British Columbia, Canada) and served as an initial testing prototype for our mock cortical surface environment [97].

Here, we have extended those approaches to a surgical microscope that is used clinically at our institution. We have developed an interactive environment that permits acquisition of stereo image capture from the microscope, calibration of the cameras, and adjustment

of parameters used for 3D point cloud reconstruction. We have also equipped the microscope with a rigid body tracking star (MICROSCOPE TRACKING ARRAY, Brainlab Inc., Westchester, IL) to permit tracking of the microscope position within an IGS system. We show that with this device we can register 3D point clouds that are acquired with the microscope in different positions thus permitting an intraopertaive calculation of cortical surface displacement. While the availability of microscope focal point tracking is possible with commercial IGS systems (although accuracy on these commercial systems is not widely reported), the implementation of a fully 3D tracked approach necessary for measuring full cortical surface field displacements is lacking. The methods we are utilizing for stereovision reconstruction are well-referenced and our goal is to explore this within the scope environment and within the context of brain shift measurement.

4.4 Methods

Section 4.4.1 describes the equipments used for data acquisition. Sections 4.4.2 and 4.4.3 explain the detail of stereovision techniques and integrated system, respectively. Section 4.4.4 shows the method of microscope tracking, and section 4.4.5 discusses the validation experiments.

4.4.1 Data acquisition

At Vanderbilt University Medical Center (VUMC) OPMI Pentero (Carl Zeiss, Inc., Oberkochen, Germany) surgical microscopes are routinely used during neurosurgery procedures (see Fig. 4.1 a). The scope used for this study is equipped with two charged-coupled device (CCD) cameras, Zeiss MediLive Trio, with a video frame rate of approximately 30 frames per second (FPS). The images or video stream in the field of view (FOV) can be displayed on a touchscreen monitor, controlled using a joystick, recorded, and exported by video output interface. Through an IEEE 1394 interface, captured data can be saved on a desktop or laptop. In our previous work, a user-friendly graphical user interface (GUI)

was proposed to facilitate the acquisition and was designed to be compatible with all USB, Point Grey Research or other IEEE-1394b (FireWire) digital cameras [97, 98].

Our novel craniotomy simulation device is designed to permit in-plane stretching as well as out-of-plane deformation of a membrane to simulate realistic displacements occurring during surgery (see Fig. 4.1 c). Two circular rings inserts can be placed in the device aperture to simulate different craniotomy sizes which can vary substantially in different cases. Outside the main circle lie five hemispherical divots that are used for registration with an optically tracked stylus, which permits tracking the deformations in our phantom setup without using the stereo-pair localization. Clamped by the four screws on each side of the device, the membrane inside the circle is made of Dragon Skin high performance silicone rubber and marked with a realistic mock cortical vessel pattern. Lateral shift can be simulated by extending the right side of the device and stretching the silicon membrane through a lead-screw mechanism. In addition to lateral motion, the membrane can be pushed down more than 1 cm by four additional medium-size screws placed around the main circle, which indicates that brain sag often manifests as a withdrawal of the brain surface into the cranium on average of 1 cm although it depends on patient head orientation. Figure 4.1 d is a stair-block phantom that is used for calibration and verification experiment. At the center of each block, there is one red disc with a dent in the circle center which can be digitized by a tracked stylus. Other parts of the phantom are painted non-reflectively in order to improve the performance of disparity computing.

4.4.2 Stereovision

The first step in stereo calibration is capturing images of calibration objects. Based on our experimental experience, taking 12 - 18 pairs of images usually produces good results. Using less pairs to calibrate does degrade robustness. We have several chessboards with different sized patterns. For this specific case, we use a planar chessboard pattern that has 8 x 6 internal corners with a block size 13.5 mm as shown in Fig. 4.2. The chessboard

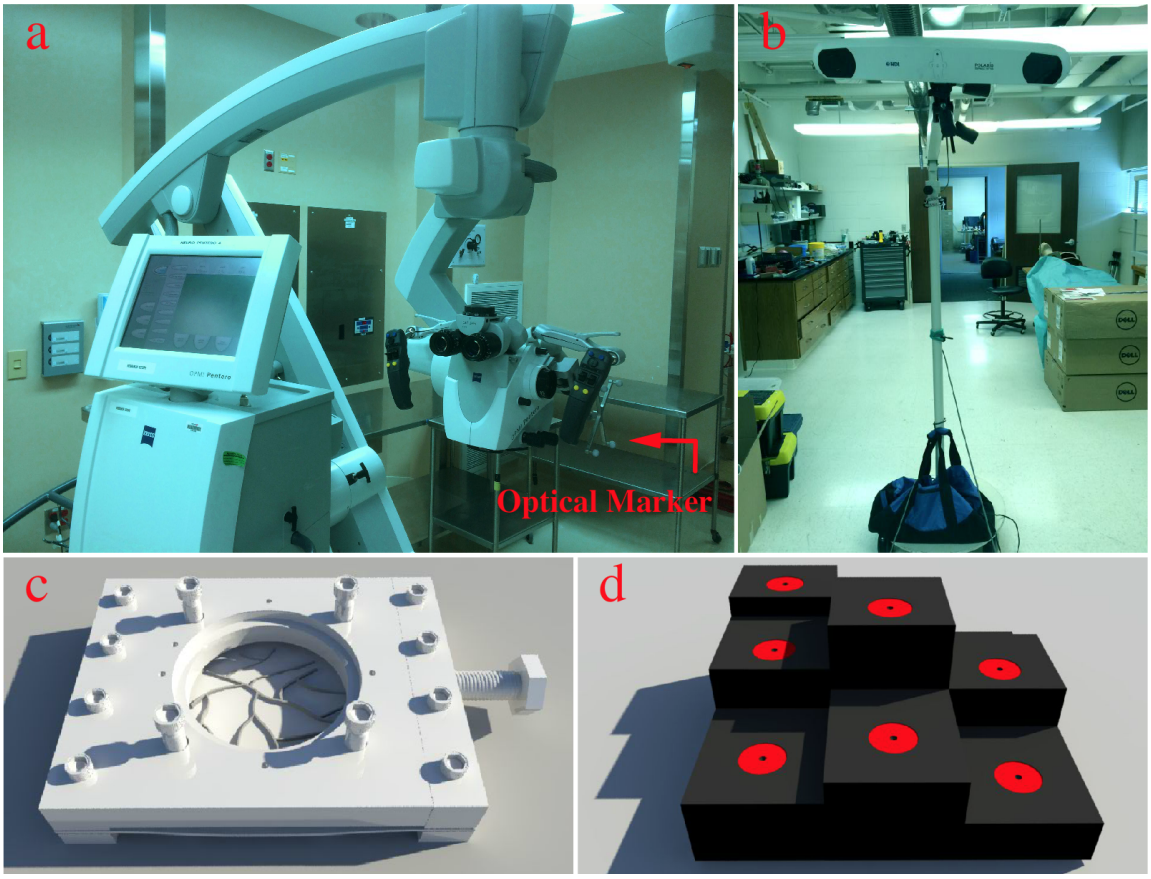

Figure 4.1: Surgical operating microscope with optical marker attached (a), optical tracking device (b), simulated craniotomy device (c), and calibration phantom (d)

images need to be captured in different positions and orientations that cover the whole field of view. In order to determine both the intrinsic and extrinsic parameters of the stereo cameras, a process of calibration is needed to find the relationship between camera and world coordinate system. In our work, we rely on a classical and widely-used method [88] for camera calibration, which builds the epipolar geometry based on the pinhole model to search for corresponding points in stereo matching. The fundamental matrix F, which encodes the epipolar geometry of two views, is defined by mapping a point in the left image x_1 to its corresponding epipolar line l_2 in the right image. For the corresponding point x_2 in the right image lying on line l_2, the following equation is satisfied:

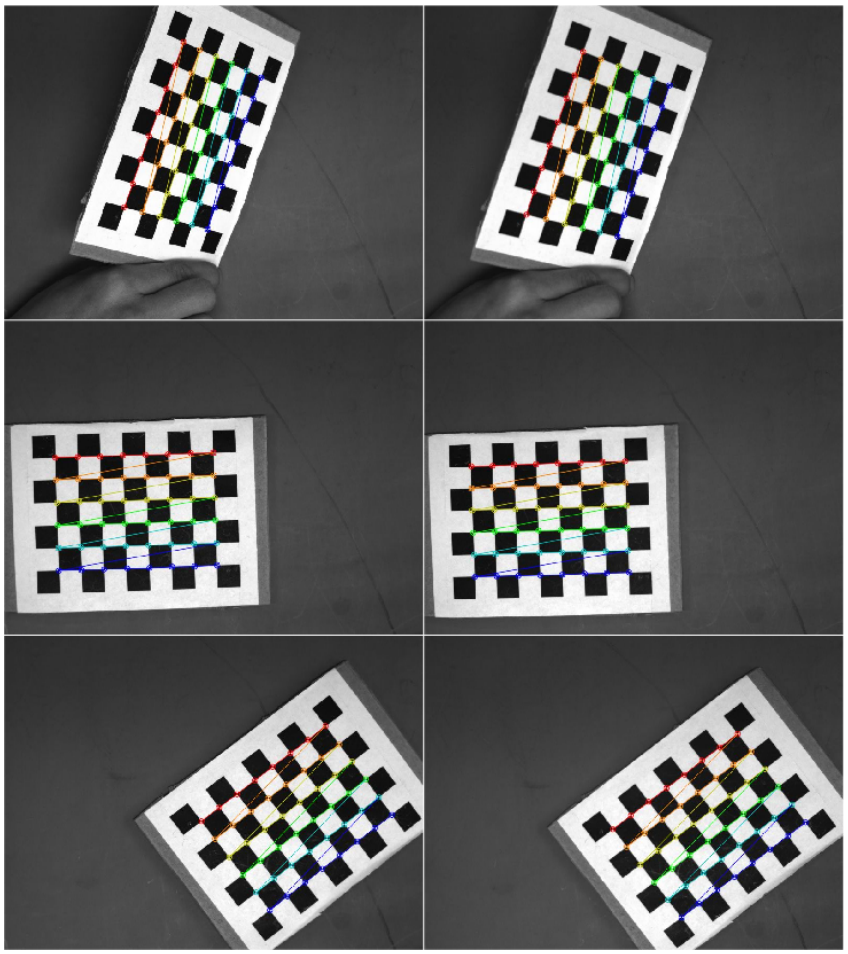

Figure 4.2: Three pairs of stereo images placed at different positions with corner detected

$$x_2{}^T \, F \, x_1 = 0 \tag{IV.1}$$

The image pairs of the checkerboard pattern provide a number of correspondences which are used to solve F using a least squares method [88]. Then the camera matrix of each camera can be retrieved using the fundamental matrix F. The accuracy of calibration is evaluated by computing the distance between the corresponding corners and the estimated epipolar lines, since in theory the corresponding corner lies on the epipolar line.

The ultimate aim of the reconstruction process is to reproject 2D image points to physical world positions. The perspective reprojective matrix Q is defined below:

$$Q = \begin{bmatrix} 1 & 0 & 0 & -c_{x1} \\ 0 & 1 & 0 & -c_{y1} \\ 0 & 0 & 0 & f \\ 0 & 0 & -\frac{1}{T} & \frac{c_{x1}-c_{x2}}{T} \end{bmatrix} \tag{IV.2}$$

where point (c_{x1}, c_{y1}) is the principal point in left image, f is the focal length (when we reproject the left image, f is the focal length of the left camera, and vice versa, for the other), and T is the horizontal distance between the two cameras centers C_1 and C_2. c_{x2} is the x coordinate of the principal point in the right image. The bottom right corner $(c_{x1} - c_{x2})/T$ is equal to zero if two principal rays intersect at infinity in a frontal parallel configuration. A 2D homogeneous point (associated with disparity d) can be transformed into a 3D point $(X/W, Y/W, Z/W)$ in world space by the following mapping:

$$Q \begin{bmatrix} x \\ y \\ d \\ 1 \end{bmatrix} = \begin{bmatrix} X \\ Y \\ Z \\ W \end{bmatrix} \tag{IV.3}$$

where w is the extra dimension in projective geometry. The image acquisition interface guarantees simultaneous capture of stereo pair, however, the left and right images are not perfectly parallel-aligned. Image pairs thus need to be rectified before computing disparity. Hartley et al. [91] have proposed an algorithm that find homographies that map the epipoles to infinity using just the fundamental matrix F. The main drawback of this method is the ambiguity in image scale, which can lead to inaccuracy in the size of the reconstructed 3D objects. Another algorithm has been proposed by Bouguet [92], which takes advantage of two calibrated cameras rotation and translation parameters to minimize reprojection distortions as well as maximizing the view overlap area. In this work, we have used Bouguet's approach. After the rectification process is completed, the disparity map can be

computed by finding the difference in x coordinates of the same features in the rectified left and right images. A number of algorithms have been proposed to calculate the disparity map, e.g., block matching (BM) [99], semi-global block matching (SGBM) [100], and a variety of other algorithms that have been evaluated and compared on an on-line platform [95, 101]. Considering simplicity, potential for near real time performance, and availability of open-source libraries such as Open Computer Vision Library (OpenCV)[96], we choose the BM approach for our stereo reconstruction algorithm. Most stereo matching algorithms are challenged by uniform texture-less areas and regions with depth discontinuities. One possible solution is to use post-filtering [102] to align the disparity map edges with source image. This has been adopted here within OpenCV. Figure 4.3 compares the disparity map result, the upper row shows the results with stereoBM alone while the lower row shows the results with stereoBM and post-filtering.

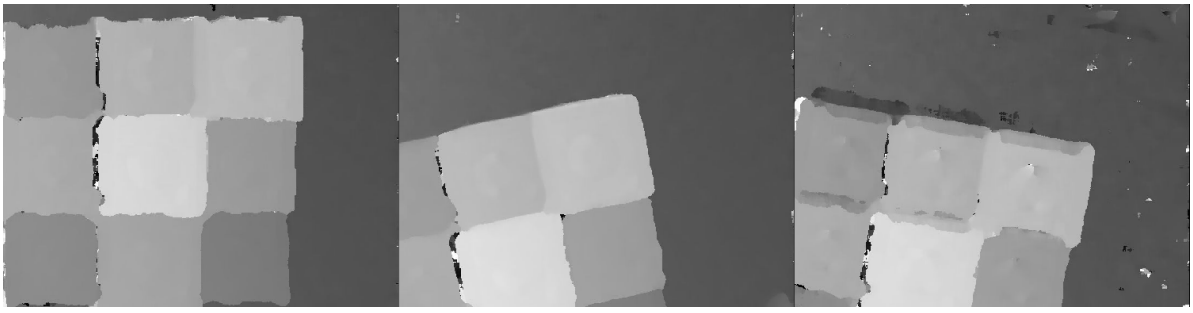

(a) StereoBM

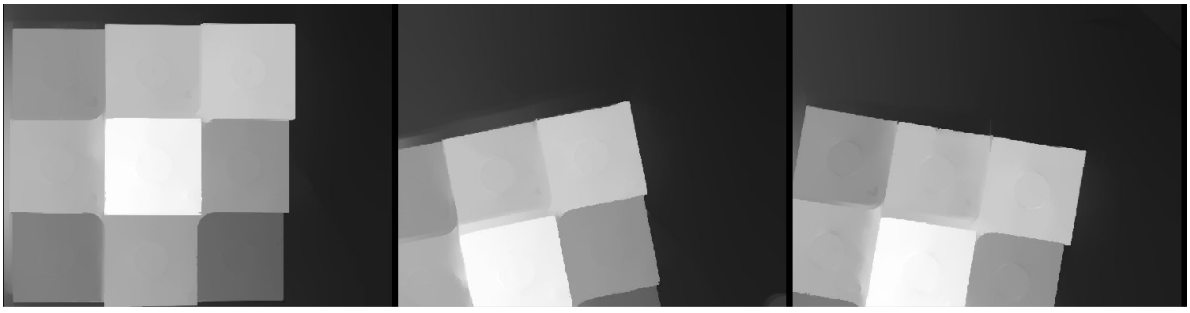

(b) StereoBM with post-filtering

Figure 4.3: Compare the disparity map with and without post-filtering

4.4.3 Integrated System

Point cloud reconstruction from microscopic stereo-pair images requires several steps: camera calibration, image rectification, disparity computation, and 3D point cloud reconstruction. Each of these steps may require parameter adjustments to produce acceptable results. To facilitate the process and make it achievable by users that are not experts in computer vision, we have developed an interactive environment. This environment includes a GUI through which parameters can be adjusted using check-boxes, spin-boxes, and line-edit widgets. Intermediate and final results are also shown. This GUI is written in C++ using Qt [103] and can be run on Windows and Linux platforms. We used the OpenCV library [96] for the computer vision algorithms, and the PCL library [104] was used to display and process point cloud data.

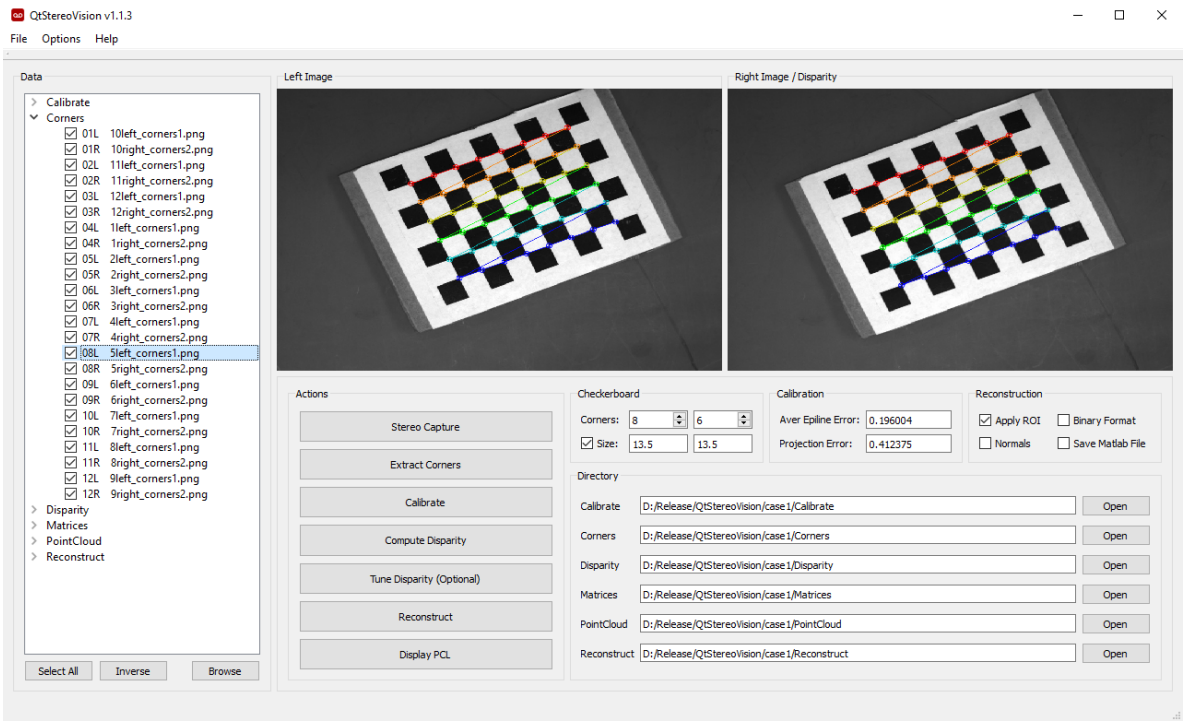

Figure 4.4: Integrated reconstruction software: main window

Figure 4.4 shows the main window of the software. On the left side of the interface is a tree-view structure used to select the input images, the output point clouds, as well as

some intermediate results. Moving to the right, a display area facilitates visualization of the stereo-pair images (left and right), and the panel below contains the series of actions and options necessary to perform the point cloud reconstruction. The first step involves stereo capture of a calibration checkerboard pattern, and the user is guided through the process. The next step is the localization of the corners in the checkerboard images, and the calibration of the stereo cameras using the method described in [88].

Once the calibration is complete, the output camera matrices are used to rectify left and right images. The disparity map can then be computed using either a block matching (BM) or a semi-global block matching (SGBM) algorithm [95]. Both BM and SGBM algorithms use nine parameters that can be adjusted. These can be adjusted using sliders while showing the disparity image produced by the current parameter values (see Fig. 4.5a). Note that all parameters for computing disparity maps begin with default values, which in many instances work quite well. When adjustments are needed, the user interface we have developed to achieve rapid tuning, Fig. 4.5a has been enormously helpful. Once the disparity image computation is deemed acceptable by the user, the point cloud can be computed for each disparity image (see Fig. 4.5b). After computing the reconstruction [90], the display panel is invoked to immediately provide a visualization of the point clouds.

4.4.4 Microscope Tracking

Microscope tracking can be performed via the use of a rigidly attached optically tracked reference body, a calibration procedure to compute the transformation between the coordinate system specified by the rigid tracking body, and the coordinate system of the reconstructed stereo-pair point cloud [64]. We use a Polaris Spectra optical tracking system (see Fig. 4.1 b) developed by Northern Digital, Inc. (Waterloo, Ontario, Canada) which has a reported tracking accuracy of 0.25-0.3mm RMS [105]. A commercially available rigid body reference with microscope mounting attachment (MICROSCOPE TRACKING ARRAY, Brainlab Inc., Westchester, IL) was employed to facilitate tracking of the surgical

microscope.

The setup for microscope tracking calibration is sketched in Fig. 4.6 (a). To summarize, the goal of the microscope tracking calibration is to determine the rigid body transform that provides a mapping between the coordinate system of the reconstructed stereo-pair point cloud (X_{cam}) and the coordinate system of the rigid body attached to the surgical microscope (X_{star}). This calibration transform ($T_{cam-star}$) is computed using a calibration phantom that is comprised of a series of fiducial disks that can be localized in both the reconstructed stereo-pair point cloud space and the coordinate system space of the microscope rigid body. The fiducial points are located in the reconstructed stereo-pair space via computation of disk centroids from the reconstructed point cloud. The fiducial point locations in the microscope rigid body space are determined via an optically tracked probe that can digitize the individual fiducial points relative to the microscope rigid body within the optical tracking system. Once these individual fiducial points have been localized in each space, a point-based registration [106] is computed to determine the camera calibration transform ($T_{cam-star}$).

4.4.5 Validation Experiments

The validation experiment includes two parts: microscope tracking validation and vessel displacement validation. The aim of the microscope tracking validation is to ensure that the calibration transformation ($T_{cam-star}$) is accurate via the transformation of a series of point cloud reconstructions, acquired at different microscope locations, to a reference coordinate space (see Fig. 4.6 (b)). At an initial position of the surgical microscope ($X_{cam,1}$), the tracked location of the scanner was recorded ($T_{star-opt,1}$), and a stereo-pair reconstruction was performed of the calibration phantom. With the phantom and optical tracking system in a fixed position, the surgical microscope was then moved to a second position ($X_{cam,2}$). Again, the tracked location of the scanner was recorded ($T_{star-opt,2}$), and a stereo-pair reconstruction was performed. Given the recorded data from the two locations, the fixed

microscope calibration transformation ($T_{cam-star}$) and the fixed optical tracking coordinate system (X_{opt}), the stereo-pair reconstructed point clouds acquired at the two microscope locations can be transformed into the same space using the following equations:

$$X_{opt} = [T_{star->opt,1}\ [T_{cam->star}\ X_{cam,1} \tag{IV.4}$$

$$X_{opt} = [T_{star->opt,2}\ [T_{cam->star}\ X_{cam,2} \tag{IV.5}$$

The steps are as follows:

1. Place the scope at base position, then place the calibration phantom under the scope. Reconstruct the point cloud of the phantom.

2. Digitize the centroids of the nine disks and record the position of the scope using the optical tracking system. The transformation matrix can be computed.

3. Move the scope to another position, while keeping the phantom static. Reconstruct the phantom and record the scope position.

4. Repeat step 3.

5. Use the transformation matrix from step 2 to transform the point cloud in step 3 and 4 back to base position and then evaluate the error.

For the vessel displacement computation, we use the craniotomy device (described in section 4.4.1) to simulate brain shift via three states (baseline, stretch, and sag as shown in Fig. 4.7). The experimental steps are as follows:

1. Set the craniotomy device in the baseline state and place it under the scope.

2. Reconstruct 3D point cloud of the device and record the ground truth positions of vessel features marked on the membrane using optical tracking system.

3. Move the scope to a new position, and apply a 2 cm horizontal stretch (lateral shift) using the screw mechanism. Then repeat step 2.

4. Move the scope to another new position, and using the four screws around the craniotomy to displace the membrane downward by 1.6 cm (this simulates sag). Then repeat step 2.

5. Using the previous transformation matrix to transform point cloud in step 3 and step 4 to base space. The movement of features marked on the membrane can be computed after the application of the tracking transformations.

To validate our system, the deformations are recorded using the optically tracked stylus. This serves as the ground truth that can be subsequently compared to the tracked microscope stereo pair measurements.

4.5 Results

Result for the stereo-pair camera calibration experiment are shown in the GUI (see Fig. 4.4). The average epiline error is 0.2 pixels, and the stereo projection error is reported as 0.41 pixels. Knowing the geometry of the calibration phantom, a reconstruction error of approximately 1 mm is estimated by systematically comparing the distance between nine divots. Since the microscope is tracked, the transformation between point clouds generated via scope acquisitions at different positions can be computed. We reconstructed the point cloud of the calibration phantom by moving the scope to three positions (see Fig. 4.8 (a) (b) (c)).

By applying the transformation matrix to the second and third point clouds (highlighted in yellow and blue, respectively, in Fig. 4.8), these two point clouds can be transformed into the same space as the initial point cloud (see Fig. 4.8 (d) (e)). Figure 4.8 (f) shows the results of registering all three point clouds together. The mean distance error is 0.64 mm in the x direction, 0.89 mm in the y direction, and 2.92 mm in the z direction. These errors are

caused by reconstruction error and tracking error. The displacement is computed by registering the simulated vessel features on the simulated craniotomy device to the same space (baseline state) shown in Fig. 4.9. Note that feature No.1 is not included in the results because it is no longer visible following the stretch (lateral shift) operation of the craniotomy device, which can also happen in actual surgeries when part of the brain slides past the craniotomy. As each measurement is independently taken and as our goal is to measure the widest distribution of shift on the surface, it will not impact the results much besides one less measurement. The difference between displacement in stereopsis (measured in 3D point cloud) and tracking system (ground truth) is calculated as displacement error and is found to be approximately 2 mm on average (see Fig. 4.10).

4.6 Discussions

The phantom experiments performed for the purpose of validating the tracking calibration for the surgical microscope use three different microscope positions. In fact, we can continuously acquire stereo pair data and render 3D point clouds in a consistent space. In our experience within the operating room, the scopes are positioned quite similarly in space with only small changes from a practical use standpoint. However, for the work herein, while we chose only three microscope positions, we did purposefully position broadly across the mock-OR space for testing(as compared to its in vivo counterpart use which is typically more limited). The experiments yield a number of error metrics that provide some insight into the range of possible error sources that are contributing factors. These contributing factors include the error due to the stereo-pair reconstruction process, manual error associated with the fiducial digitization and centroid extraction, sub-optimal calibration phantom design and the tracking error associated with the rigid body attachment to the microscope and the tracked stylus.

The stereo-pair reconstruction error highly depends on the quality of the disparity com-

putation. Camera calibration affects the rectification step, which is critical for computing disparity. The scope tracking error is computed by comparing the point clouds that are transformed to the same scope coordinates. The X, Y, and Z direction mean distance errors are computed and the results show that the error in the Z direction is higher than in the other two directions. This may be due to the error in estimating depth from disparity. The point cloud reconstruction is more accurate in the horizontal direction than in the vertical direction. Considering that the maximum height difference of the steps on the phantom is nearly 50 mm (larger than the normally reported brain deformation), the mean distance error is, to some degree, acceptable. We also note that stereo reconstruction techniques are challenged by sharp edges such as the steps on the phantom. We expect that our reconstruction error would be smaller with a phantom that would have smoother edges as would the cortical surface.

Moreover, the error of the tracking system itself and the localization error associated with the use of a tracking stylus also contribute to the calibration error of the surgical microscope. Error associated with the tracking system used in these experiments are reported by the manufacturer and are within an acceptable range. However, any error associated with the calibration files generated for the tracking of the rigid body attached to the microscope as well as the tracked probe can be potential sources of error. Finally, any manual localization inaccuracy in the digitization of the points on the calibration phantom with the optically tracked probe can introduce errors. With respect to conventional image guided neurosurgery, accuracy of 1-2 mm is certainly a target goal to strive for (note, this is the typical range of practically tracked tools). While 2-3mm is not ideal, we would suggest that the accuracy is clinically relevant as brain shift that routinely occurs in tumor resection surgery is on the order of 1-2 cm. Therefore, the accuracy of this system is sufficient to provide some benefit to soft-tissue deformation correction IGS systems. We do however acknowledge that more work is needed to improve the fidelity but the work here is highly encouraging.

The main goal of this work is to demonstrate the ability to take advantage of stereovision-based techniques to track tissue deformations with arbitrary movement of the surgical microscope. While the results presented indicate that the presented method of microscope tracking calibration is promising, there are a number of avenues for improving the calibration results. Primarily, refinement in reconstruction techniques should facilitate more accurate calibrations. Additionally, the use of an optimally designed calibration phantom would facilitate more accurate results as well. Finally, our calibration method is only useful for fixed microscope setting where the focal length and zoom factor cannot change during the whole procedure. Typically, when magnifications are changed, surgeons are navigating deeper into the brain tissue. In our experience, tissue features for stereo-pair reconstruction are not readily present as the tissue is invaded. In fact, when navigating deep into the tissue, typically the common focal point localization associated with commercial tracked scopes is all that is needed, i.e. make the microscope essentially similar to a tracked stylus. With that said, we note clearly here that this routine function does not diminish the work presented herein. More specifically, with a single tracked focal point, it would be impractical to refocus the scope on each tissue feature to continually track deformations. With that understanding and in considering measuring deformations of the feature-rich cortical surface, in our experience this can be achieved by coming back to the original field of view with the near-original magnification to make measurements off the visible cortical surface at the start and at different times during surgery. However, the ability to recalibrate at any time, including when the OR field is sterile, is an important feature to a generalizable framework. We are working toward a solution which combines tracked stylus localization and collocated stereo-pair point reconstruction object that essentially allows for very fast calibration. Future methods will entail the ability to generate calibration data that allows the use of multiple microscope settings throughout the surgical procedure.

4.7 Conclusions

In this chapter, we have proposed a GUI-based system that integrates all necessary functionality for reconstructing FOV of stereo-pair or microscope cameras including (1) capturing stereo-pair images or video streams, (2) extracting checkerboard corners, (3) calibrating stereo cameras, (4) computing disparity, and (5) displaying point clouds. Moreover, the parameters associated with the disparity computation can be modified in an interactive GUI to improve the results. This reconstruction system is functional, user-friendly, and it requires only minimal prior knowledge. By applying image-to-physical space registration, the stereoscopic microscope can be tracked, and freely moved without disrupting the surgical procedure. The reconstruction accuracy and displacement comparison results suggest that this system could be used to gather cortical data to measure and compensate for brain shift during image-guided surgery. This would extends the capability of conventional navigation system.

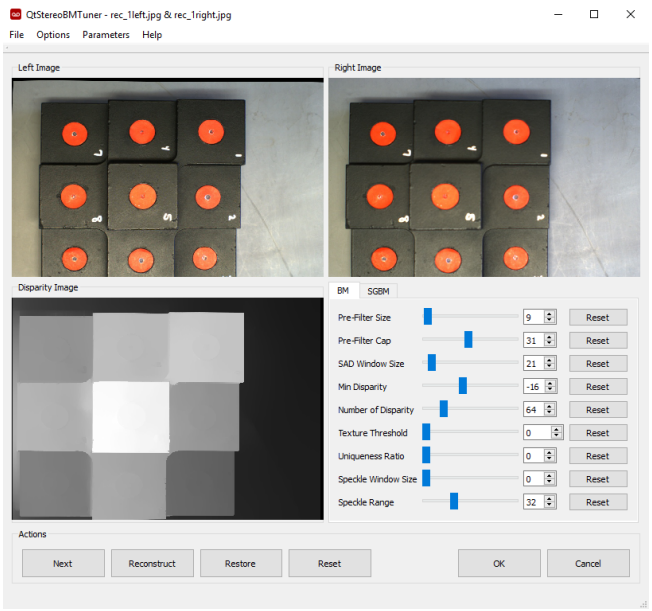

(a) Disparity tuner panel

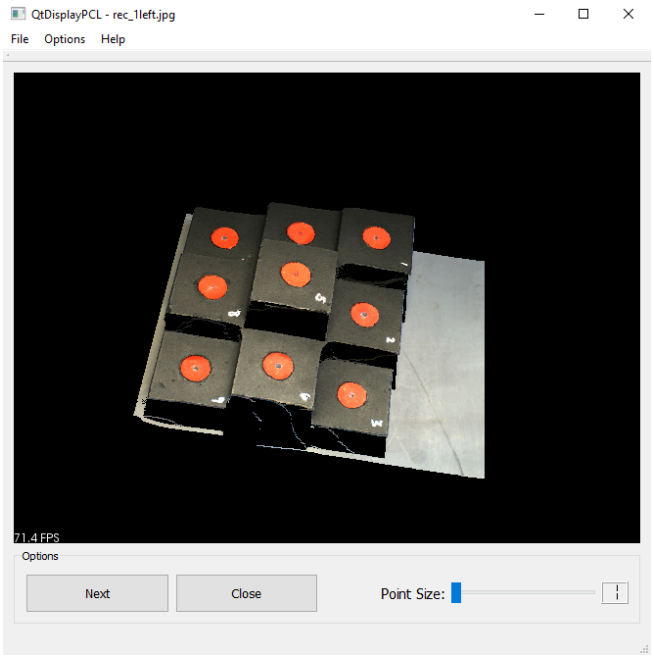

(b) Point cloud display

Figure 4.5: Integrated reconstruction software: (a) disparity tuner panel, and (b) point cloud display window

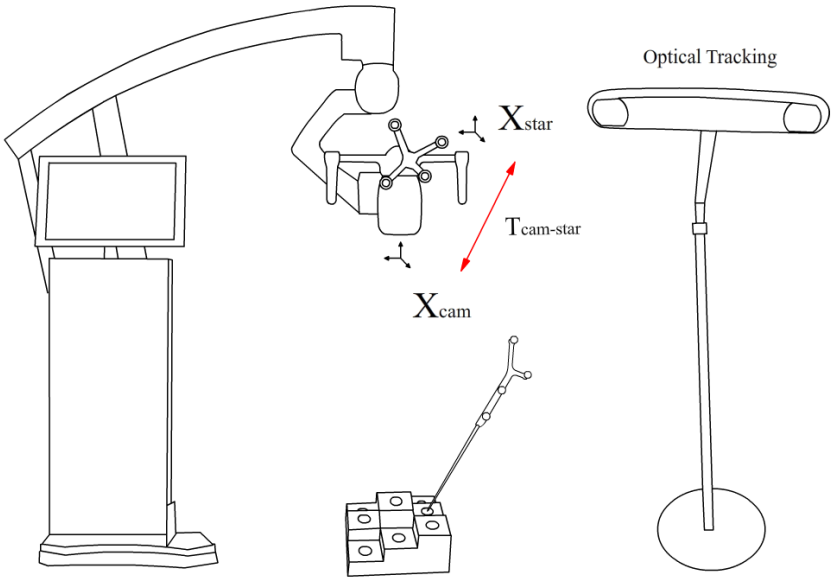

(a) Calibration procedure

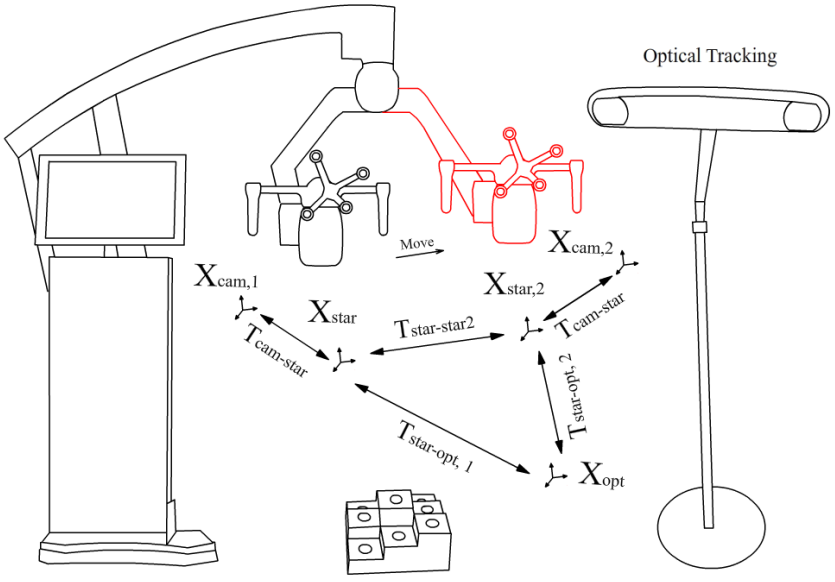

(b) Tracking experiment

Figure 4.6: The setup of calibration procedure and tracking experiment

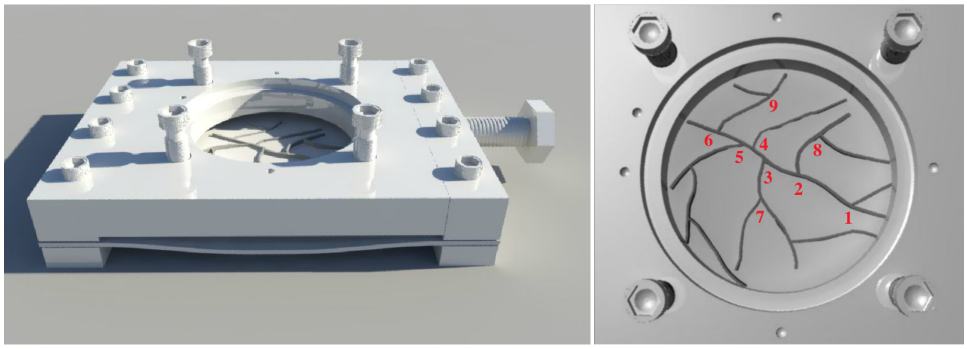

(a) Baseline

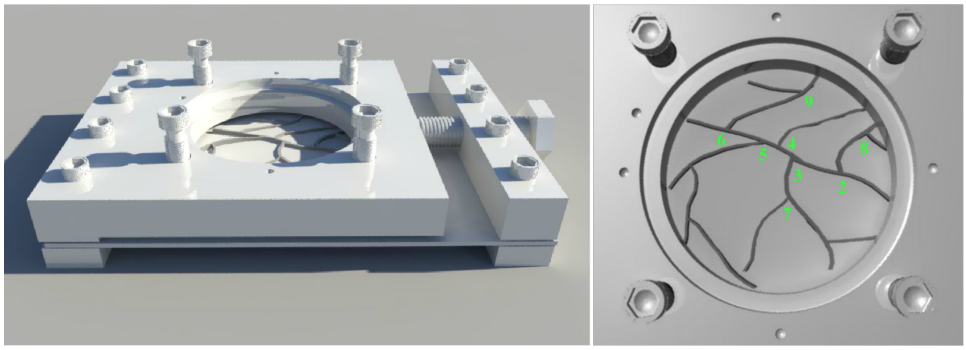

(b) Stretch (Lateral Shift)

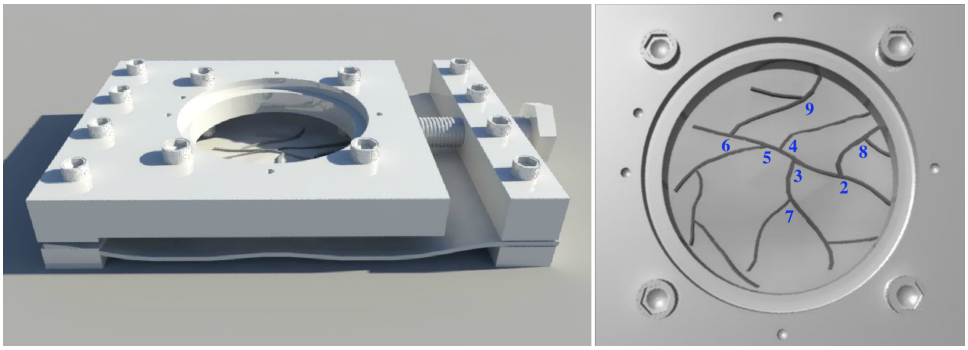

(c) Stretch + Sag

Figure 4.7: Three states of generating simulated brain shift: baseline, stretch (lateral shift), stretch as well as sag

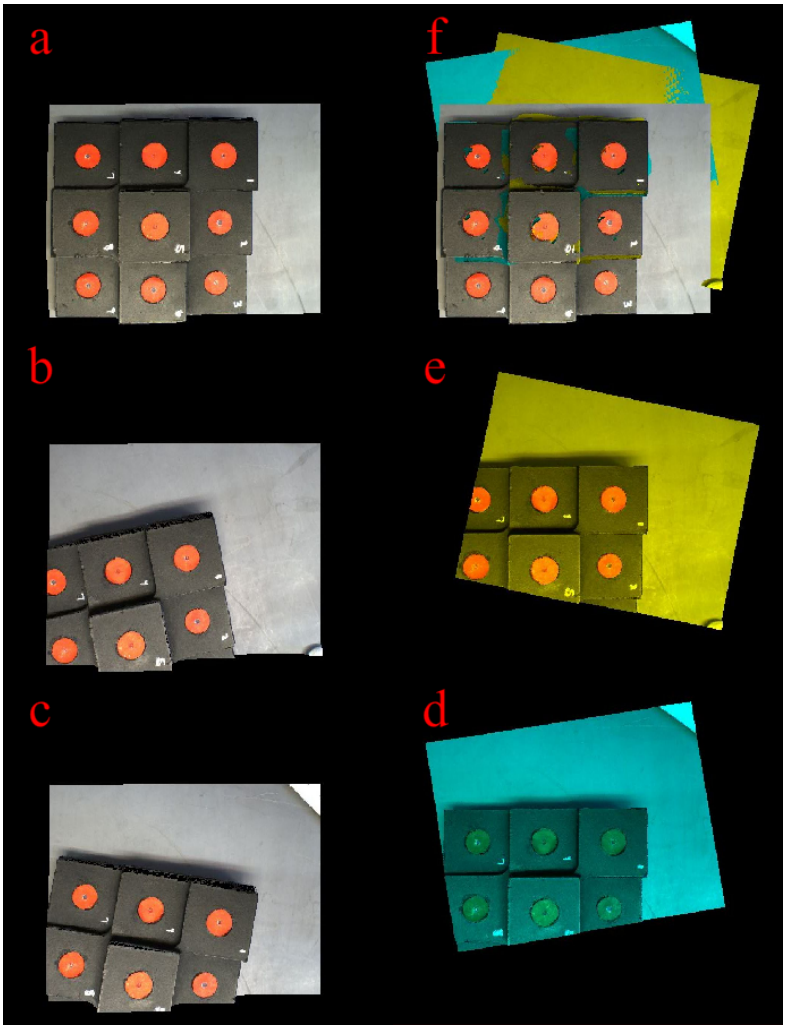

Figure 4.8: (a,b,c) are stereo-pair derived point clouds from three different microscope positions, respectively, (d) is the point cloud from (b) aligned to the coordinate reference of (a), (e) is the point cloud from (c) aligned to the coordinate reference of (a). Finally, (f) is the overlay of all clouds (a,b,c) to the reference of (a).

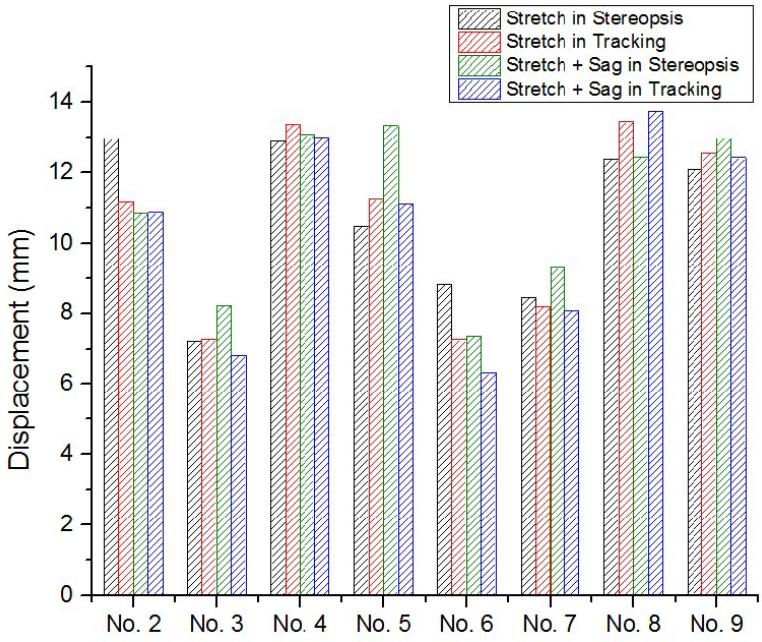

(a) Displacement

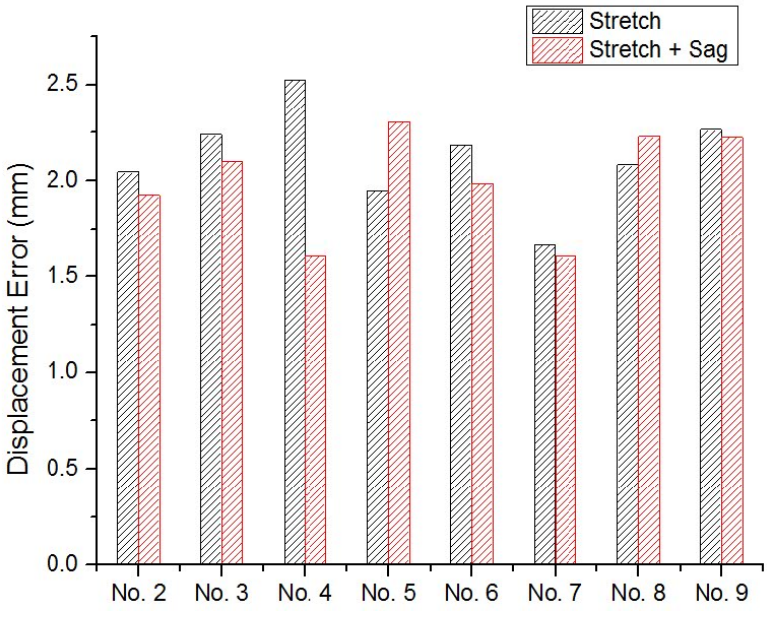

(b) Displacement error

Figure 4.9: Bar of displacement and displacement error

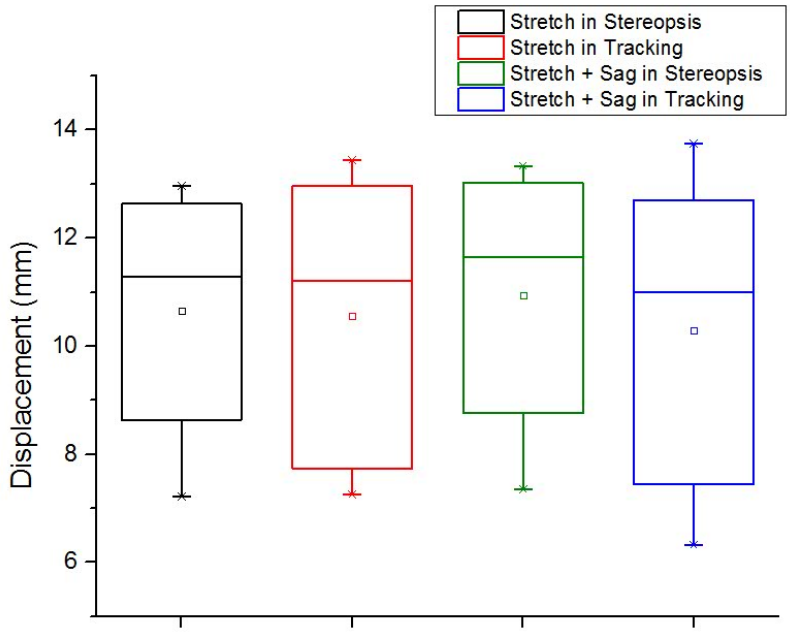

(a) Displacement

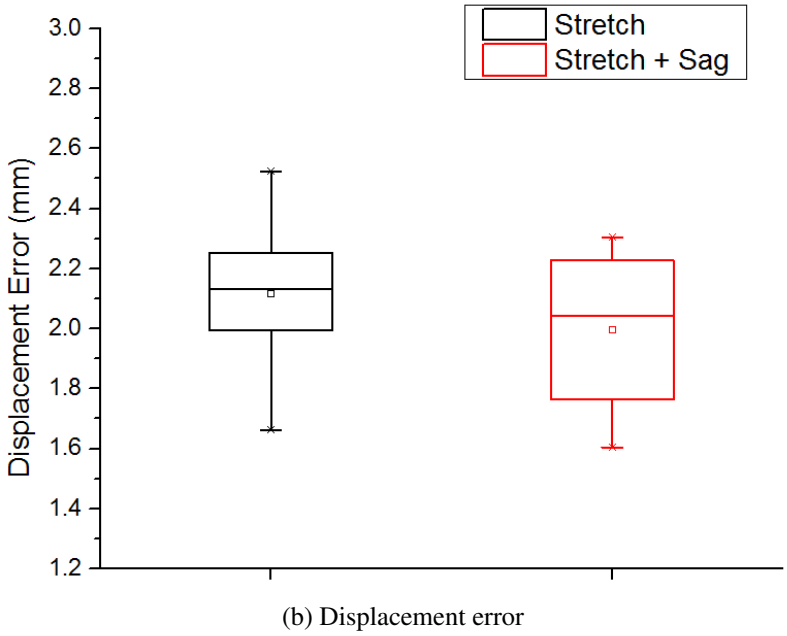

(b) Displacement error

Figure 4.10: Box plot of displacement and displacement error

Chapter V

DEVELOPMENT AND EVALUATION OF A 'TRACKERLESS' SURGICAL PLANNING AND GUIDANCE SYSTEM BASED ON 3D SLICER

5.1 Summary of Contributions

This chapter demonstrates the feasibility of using a trackerless image-guided system to plan craniotomy. A well-developed interactive extension of 3D slicer can simplify the procedure of pre-operative planning and provide reliable craniotomy path. The work herein when combined with our cortical surface registration, cortical deformation measurement methods, and finally computational brain shift prediction framework is a powerful paradigm that could potentially eliminate the need for conventional tracking technology and usher in integrated more nimble vision-based guidance systems for neurosurgery.

5.2 Abstract

Conventional optical tracking systems use cameras sensitive to near-infrared (NIR) light and NIR illuminated/active-illuminating markers to localize instrumentation and the patient in the operating room (OR) physical space. This technology is widely-used within the neurosurgical theatre and is a staple in the standard of care for craniotomy planning. To accomplish, this planning is largely conducted at the time of the procedure in the OR with the patient in a fixed head orientation. In the work presented herein, we propose a framework to achieve this in the OR without conventional tracking technology, i.e. a 'trackerless' approach. Briefly, we are investigating an extension of 3D slicer that combines surgical planning and craniotomy designation in a novel manner. While taking advantage of the well-developed 3D slicer platform, we implement advanced features to aid the neurosurgeon in planning the location of the anticipated craniotomy relative to the pre-operatively

This chapter has been published in Journal of Medical Imaging, 6(3), 035002.

imaged tumor in a physical-to-virtual setup, and then subsequently aid the true physical procedure by correlating that physical-to-virtual plan with a novel intra-operative MRI-to-physical registered field-of-view display. These steps are done such that the craniotomy can be designated without use of a conventional optical tracking technology. To test this novel approach, four experienced neurosurgeons performed experiments on five different surgical cases using our 3D Slicer module as well as the conventional procedure for comparison. The results suggest that our planning system provides a simple, cost-efficient, and reliable solution for surgical planning and delivery without the use of conventional tracking technologies. We hypothesize that the combination of this craniotomy planning approach and our past developments in cortical surface registration and deformation tracking using stereo-pair data from the surgical microscope, may provide a fundamental new realization of an integrated 'trackerless' surgical guidance platform

5.3 Introduction

In conventional image-guided surgery (IGS), the patient's tumor is estimated at the time of surgery in the operating room physical space using optical tracking technologies and image-to-physical registration methods. More specifically, an image-to-physical mathematical transform is determined by identifying corresponding features in both the patient's images and on the physical patient in the OR. Once this registration is done, a tracked physical stylus can be used to navigate on and within the cranial surface by showing the magnetic resonance image (MRI) slices on a display that correspond with the stylus tip interacting with the patient in physical space. Typically, neurosurgeons will use this conventional image-guided setup to plan a craniotomy that is dependent on tumor location and other anatomical considerations. This typically involves using the guidance display (facilitated by the optically tracked stylus) to provide assistance with marking the spatial extent of the planned craniotomy on the physical patient. More specifically, optical tracking consisting of a camera and tracked stylus is used to localize physical points which

correspond to image-based counterparts. These points are used to provide a relationship between image and physical patient space. With respect to the display, the conventional display consists of a four-panel arrangement of images with sagittal, axial, coronal slices and a fourth panel that is commonly an isometric view. Once the craniotomy designation is complete, the guidance system is removed from the immediate patient space and usually not utilized again until the cortical surface is presented. As surgery progresses, the guidance system can be used again to monitor progress.

Previous work by Miga et al. [63] demonstrated how pre-operatively MR-imaged cortical surfaces could be aligned to 3D textured point clouds collected intra-operatively. In subsequent work by Sinha et al. [66], they demonstrated how 3D textured point clouds could be used to track cortical surface deformations. Recently, in work by Yang et al. [82, 97, 107], the ability to use a surgical operating microscope equipped with a pair of stereo-cameras to monitor deformations using computer vision techniques was demonstrated. More specifically, using a mock deformable cortical surface phantom, surface deformations were measured using an optically tracked surgical microscope (i.e. via NIR tracking, the scope focal point is akin to a physical stylus) and then compared to an approach that utilizes sequential stereo-pair reconstructions [98, 108] with a fixed visible target reference in the microscope field of view (effectively a "trackerless" measurement approach). This body of work only focused on characterization after the craniotomy was performed and assumed that conventional image-guided approaches were to be used to plan the craniotomy. In this investigation, we demonstrate a method that allows a craniotomy to be planned without the use of the conventional tracking approach. The purpose of providing the conventional approach within this work is to specifically compare neurosurgical craniotomy-preparation to our proposed novel approach. This work is the last step needed to realize a complete 'trackerless' methodology, for neurosurgical procedures without conventional tracking, i.e. a 'trackerless' approach.

5.4 Methods

5.4.1 Interactive Extension

3D Slicer [109] is an open-source, integrated medical processing platform for surgical guidance. It is widely-used in clinical research applications since it provides many modules of common data processing for guidance environments. It also facilitates the development of new research functionalities and abstractions by clinical researchers. Our proposed 'trackerless' surgical image-guided system is an interactive extension of 3D Slicer using Python. The module has the following components: (1) the 3D view of the patient brain and tumor is rendered using OpenGL, (2) the main user interface is developed by Qt [103], and (3) all data is processed using VTK [110] and ITK [111] libraries. All of these can be easily accessed, modified, and integrated with common Python scripting, broadening the feasibility of using this module in a clinical setting.

The developed module has been customized for neurosurgery by: (1) providing a user-friendly interface for planning neurosurgical procedures, (2) importing and integrating relevant pre-operative data seamlessly, (3) creating a patient image data navigation environment using a computer-generated virtual stylus, (4) allowing for the visual integration of a pre-operative textured point cloud of the patient's physical head and corresponding image data for planning, and (5) most importantly facilitating the determination of the craniotomy. The navigational environment proposed is to guide the craniotomy location and extent without the use of conventional tracking technology. The interactive extension (represented in Figure 4.1) can be separated into distinct platform features and it has functionality over conventional guidance displays because of the provided assistance using the virtual representation [112].

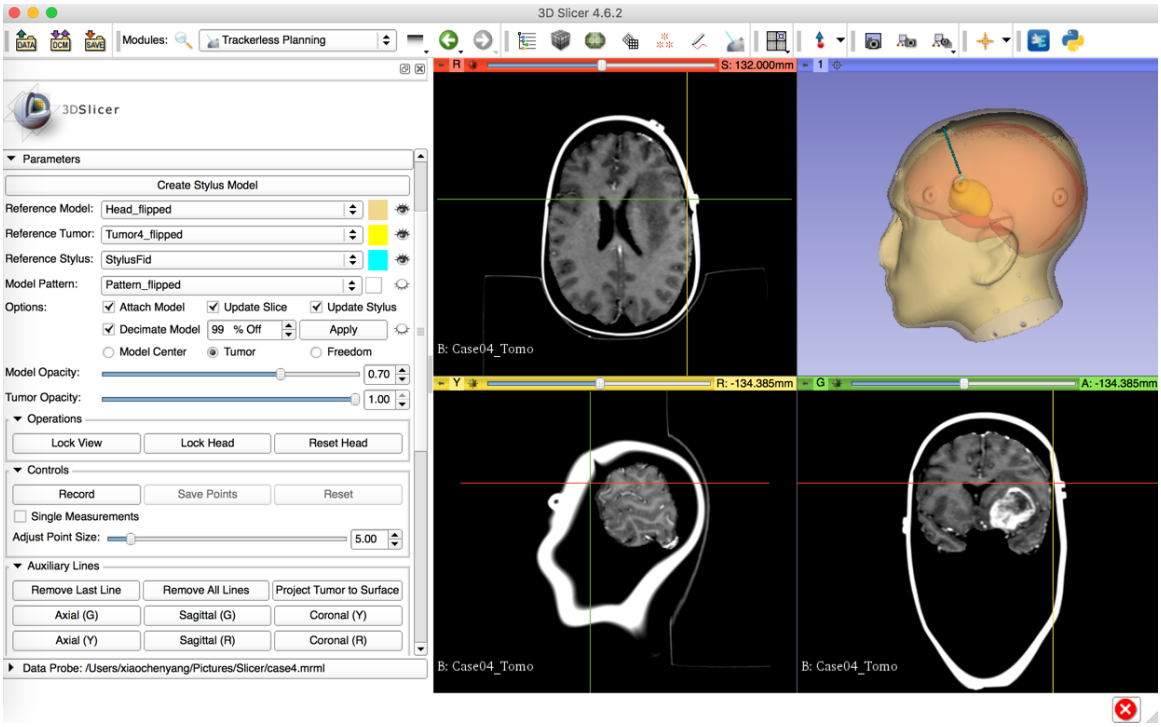

Figure 5.1: Overview of the 'trackerless' surgical planning extension. The virtual stylus and traditional three-panel display of the MRI mirrors the display in the conventional approach.

5.4.1.1 Simulation of the stylus in the OR

An important feature of the 'trackerless' surgical planning extension is the ability to freely navigate and visualize the patient's pre-operative MRI without tracking technology, in a manner similar to current conventional craniotomy planning. To accomplish this, a virtual form of conventional planning was created. A virtual stylus, similar to the real physical stylus on the physical patient, is used to provide a reference on the patient's virtual head as it relates to the underlying extent of lesion (pre-operative MRI). Rather than registering the physical patient in the OR to the pre-operative images in order to plan the craniotomy (conventional IGS), a realistic virtual environment is provided to accomplish the goal without the patient. Given the functionality of 3D Slicer for conventional IGS investigations, it was a natural choice to facilitate this planning phase. The 3D view can be freely controlled, i.e.

rotating (yaw, pitch, and roll) and zoom. In addition, the color and opacity of the model can be adjusted according to user (neurosurgeon) preference. The opacity changes allow one to virtually interact with the head model in either a way analogous to the OR setting (no visually observable reference to tumor), or in a novel way enabling the neurosurgeon to take advantage of the added subsurface visualization cues as in Figure 4.1 (top right panel).

5.4.1.2 Simulation of conventional display in the OR

The next aspect that must be matched, with respect to conventional craniotomy planning, is that the MRI must be actively updated when moving the virtual stylus in a manner similar to that in conventional planning, i.e. with each virtual movement, the display can perpetuate the MRI anatomy visualization in its cardinal planes (axial, coronal, sagittal). This complete virtual guidance system function is a core functionality to our 'trackerless' intra-operative craniotomy designation approach. Traditionally, this is done by registering the pre-operative MRI image to physical space, allowing the physical stylus to navigate the image space while physically touching the patient's head surface. In our configuration, the virtual stylus is driven by the computer mouse, so there is no need for image-to-physical registration. 3D Slicer has added functionality, standard on most image processing platforms, which allows the user to more directly interact with the different MRI views independently. This allows lesion extent to be determined in image-space with the corresponding update of the virtual stylus position such that image-space can provide a position to be marked for the craniotomy plan on the head surface. More specifically, as a surgeon would choose to designate locations using the MR images, the virtual stylus is automatically controlled to be at the closest point on the head surface in the model to assist in virtual craniotomy demarcation. In conventional IGS systems, and as alluded to above, the standard IGS procedure is that physical space stylus positioning by the surgeon facilitates image space extent observations. While the virtual platform also allows for this, it does also allow for the counterpart whereby positioning in the MRI images facilitates a virtual stylus

position on the virtual head surface. Figure 4.1 shows the more traditional planning display approach whereby digitization by the virtual stylus on the head surface is propagating to the appropriate image cardinal planes within the MR images.

5.4.1.3 Adding capabilities for assisting in craniotomy designation

While crosshair interrogation of the patient MRI is utilized extensively in conventional guidance displays, i.e. if a point on the head is designated with tracked stylus, the cross-sectional images in the cardinal planes are displayed with cross-hair on the image surface border. As indicated above, we also project the cross-hairs in their proper 3D orientation on the virtual physical model. As shown in Figure 5.2, we use these cross-hair lines on the head model surface to assist the neurosurgeon determining the extent of the tumor boundary.

This extension facilitates a means to designate the tumor boundary accurately on the virtual surface of patient's head. Clearly, the tumor can also be viewed in the planning extension by adjusting the opacity of head model. Through consultation with the neurosurgeons participating in this study, we found that there are additional MR-identified brain features that surgeons use to assist in craniotomy planning versus just the segmented enhancing tumor provided by typical image processing techniques. Typically, surgeons account for major landmarks and structures to avoid during their craniotomy planning as well. As an example of labeling tumor extent in the module, in Figure 5.2 the boundary of the tumor was determined by checking the axial and coronal view of the MR images. Figure 5.2 (a) and (b) show the front boundary while (c) and (d) show the back boundary of the tumor. The intersection of the axial view (cross-hair of yellow and green line) can be added on the 3D view. Once the boundary is determined, a green dot landmark can be marked on the boundary place, as shown in Figure 5.2 (d). Similarly, the top and bottom boundary can be decided by scrolling the coronal view of the MR image. After four boundary landmarks are marked using the techniques in Figure 5.2, the virtual stylus is placed at

the center of these four points and the tumor location can be projected to the head surface. This projects a cluster of yellow lines from the tumor to the stylus direction (see Figure 5.3 a and b) which provides an accurate boundary border of the tumor on the virtual head surface. This provides the neurosurgeon with a visual reference of the tumor, including size and location on the virtual patient's head. The final craniotomy contour plan is decided by the surgeon from the information provided with the projection serving typically as a guide in the ultimate craniotomy designation.

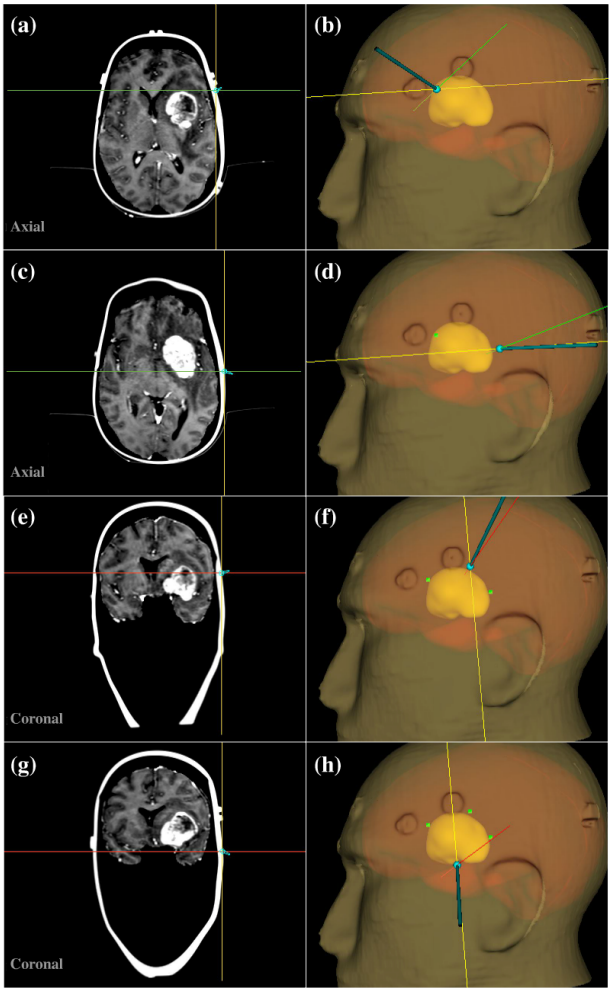

Figure 5.2: Visualization of determine boundary landmarks for tumors: (a), (b) the anterior boundary; (c), (d) the posterior boundary of the tumor; (e), (f) the superior boundary; and (g), (h) the inferior boundary. In every pair of images, the crosshairs on the MRI correspond to the stylus position on the virtual head.

5.4.1.4 Freehand craniotomy designation

In the 'trackerless' planning tool protocol relayed above, the neurosurgeon now has display information that provides landmarks and a projected tumor location on the patient's virtual scalp. These are essential guides to aid in designating the craniotomy plan. The planning approach, quite simply, is a freehand drawing on the surface (like is done in the real OR) facilitated by effectively coupling the virtual stylus as shown in Figure 5.3 (c) to the surface where planning information is present. The planning phase is completed by saving the craniotomy contour which can subsequently be reloaded in 3D Slicer for future use for the craniotomy designation on the physical patient just prior to the start of the procedure.

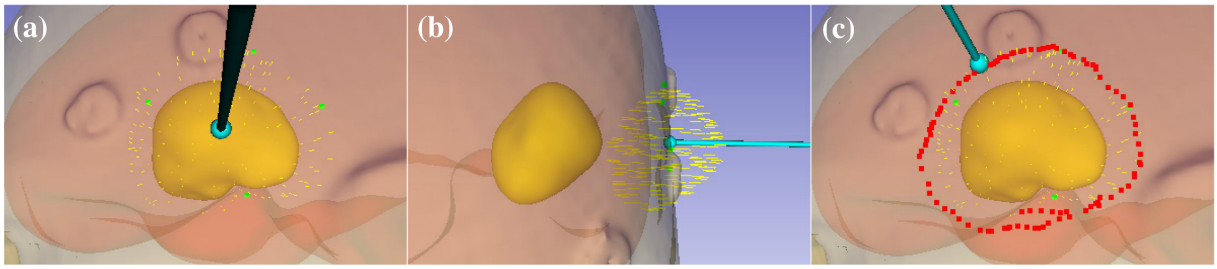

Figure 5.3: (a, b) Project tumor to surface and (c) draw craniotomy contour virtually.

5.4.1.5 Translating from virtual planning to physical surgical guidance

To move from planning to execution, the application will integrate the virtual head surface to the physical patient's acquired three dimensional textured point cloud (3DTPC). The 3DTPC can be provided by a variety of low-cost technologies, for example, laser range scanner. Other technologies such as stereo-pair technologies [113] and structured light [114] are also under investigation. Here, the DAVID SLS-3 3D scanner (DAVID Vision Systems, Koblenz, Germany) is used to scan the patient's head. Once a 3DTPC of the patient's head can be acquired, an iterative closest point registration can be performed to align with MRI Image. In the past, we have done extensive work with an optically

tracked laser range scanning technology [67] that studied the use of face-based textured point clouds to perform a face-based registration for use within conventional IGS systems. Here, we use similar orbital/head-surface registration methods as was in [61, 67]. Conventional guidance provides a link between the MR-image and physical OR space using optical tracking technology. The 3D texture-to-MR alignment in our method is also a form of image-to-physical space representation. In our approach, we add distinct markings in a grid-like fashion on the patient prior to acquiring the 3D textured point cloud of their head as physical reference (all without conventional tracking technology). One additional benefit to this method is that with no need for tracking technology, this process can be done any time prior to the procedure after the patient imaging is acquired, e.g. in the patient's room while waiting to be transported to the operating room (provided surfaces are prepared for surgery). Conventional guidance platforms require a geometric reference to be attached to the patient so that tracking equipment can be moved around the operating room without losing patient reference. As a result, craniotomy planning must be performed at the time of surgery. This is not the case for the methodology proposed in this investigation. Additionally, the texture provides a real physical space representation of the actual patient to the projected craniotomy plan provided by the aforementioned steps. Figure 5.4 (a) shows the textured pattern of our mock patient scanned by a 3D structured light scanner. This represents the mock physical patient with physical pattern overlaid on the patient's head. Figure 5.4 (b) shows the segmentation and mesh reconstruction of the head, brain, and tumor from MR image. Figure 5.4 (c) shows the registration result of the 3DTPC scan of the head and head surface derived from MR. Figure 5.4(d) overlays an example of a virtual planning craniotomy contour onto the head surface model. This is an example of a 3DTPC-to-MR reference display that the surgeon could use as a reference to mark the physical patient's craniotomy in the OR without tracking technology. More specifically, within the operating room, the reference shown in Figure 5.4 (d) display could be provided to the surgeon while the patient head is fixed. The patient's head would still have all tex-

tured information. Using Figure 5.4 (d) display, the surgeon could then use the texture landmarks as a reference to transfer the virtual craniotomy to the physical patient, all performed without conventional tracking. In summary, rather than the conventional tracking providing the link, texture references become the link.

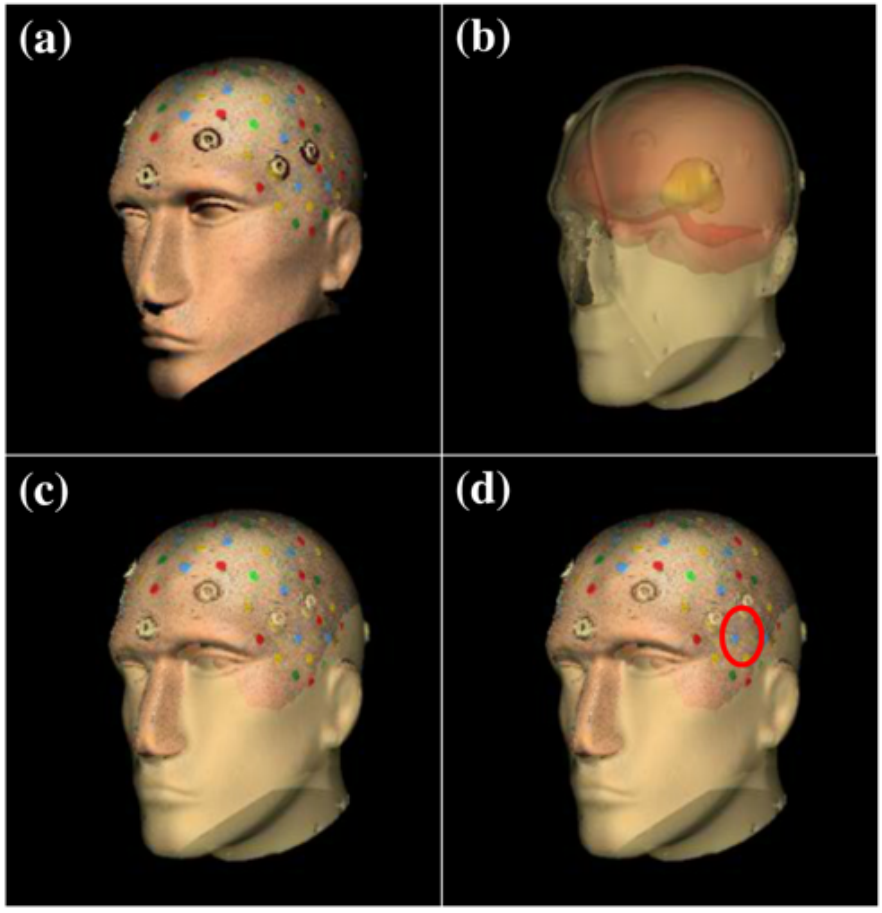

Figure 5.4: (a) Textured scan model from a 3D structured light scanner. (b) Mesh segmentation reconstruction from MR image. (c) Register textured scan model and mesh reconstruction together. (d) Overlay the virtual planning contour onto the registered head surface model.

5.4.2 Experiments

We designed an experiment to test the proposed 'trackerless' craniotomy planning versus conventional craniotomy planning. The experimental system involves a head-shaped

phantom with real clinical MR pre-operative brain scans appropriately scaled and positioned within the head representing a surgical candidate. In order to evaluate the performance of this 'trackerless' surgical image-guided system extension, we compared it with the conventional procedure that employs standard optical tracking instrumentation. Note that the surgeon performed the conventional and trackerless approach on different days and with at least a week in between visits. This was done to avert possible bias associated with the order of performed planning type, i.e. conventional or trackerless.

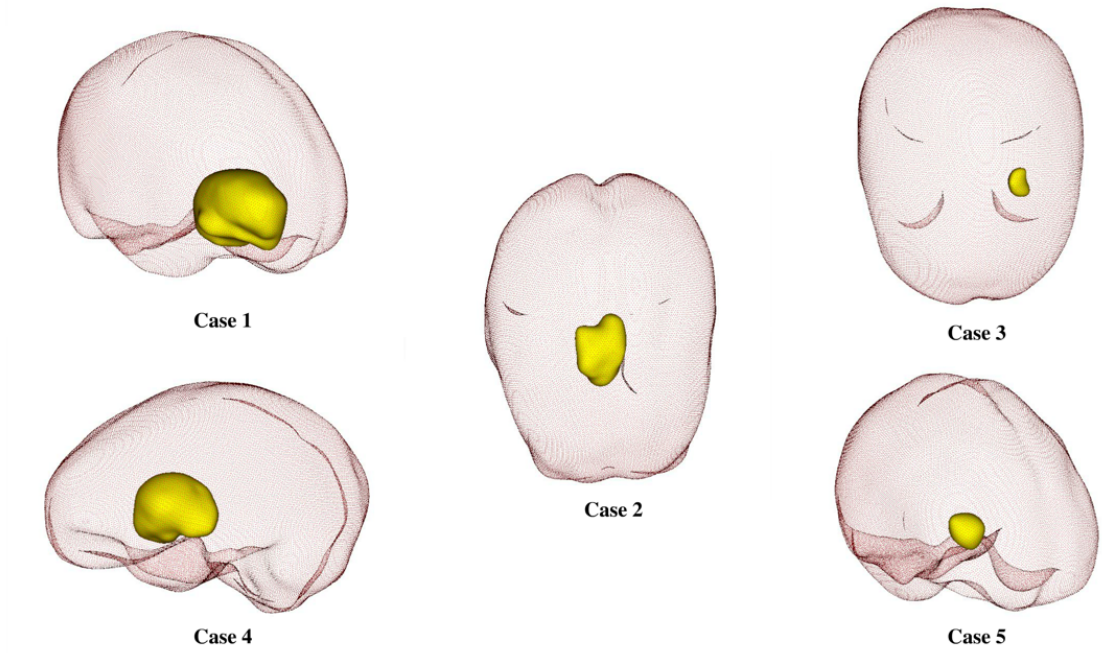

Figure 5.5: Five cases of clinical patient data for experiment showing different tumor presentations.

5.4.2.1 Conventional approach description

As a control to compare to, we recreated conventional plans with our mock OR. In this approach, the neurosurgeon begins by examining a given patient case on 3D Slicer to visualize the tumor size and location. Using this knowledge, the neurosurgeon chooses a suitable orientation for the physical phantom head. Image-to-physical space registra-

tion is then performed using the Fiducial Registration Wizard (SlicerIGT extension [115]), OpenIGTLinkIF [116], and the PLUS toolkit [117] (an application that streams live tracking data to 3D Slicer). This point-based registration begins by selecting the center points of the attached MR-visible fiducials on the mock head surface and virtual image volume. Within the mock OR, the corresponding fiducials are digitized using a Northern Digital Polaris Spectra (NDI, Waterloo, Ontario, Canada). These fiducial centers are also digitized in 3D Slicer on the virtual image using OpenIGTLinkIF and the PLUS toolkit. Following rigid registration, the neurosurgeon uses the conventional image guided display and stylus to designate surface landmarks and visualize the extent of the tumor on the surface of the physical head. The neurosurgeon then draws the craniotomy contour on the surface of the head with a marker using the traditional guidance display to assist. Then, the neurosurgeon uses the digitizing stylus to trace the craniotomy contour drawn with the marker to quantify the planned craniotomy size and location for comparison with 'trackerless' approach. Our custom OpenIGT extension collects the digitized points in physical space and transforms them to image space providing a contour that represents a conventional craniotomy approach in image space. This is done for all five patient cases (Figure 5.5).

5.4.2.2 'Trackerless' approach description

For every case (5 total), the neurosurgeon is also asked to plan a tumor resection procedure using our 3D Slicer module on a day other than the conventional planning. This procedure starts with the case being uploaded into 3D Slicer and with the neurosurgeon viewing the fused image data in order to establish a geometric understanding of tumor size and location. Next, the virtual stylus and traditional cross sectional display (Figure 4.1) is used by the neurosurgeon to virtually plan the patient's craniotomy. The neurosurgeon uses the record function to trace a contour for the craniotomy using the cross-sectional display and landmarks as a guide. After craniotomy planning is achieved, the 3D scan of physical head with a physical pattern (Figure 5.4 a) is registered to image space (Figure 5.4 b)

using a surface based registration and the head geometries (Figure 5.4 c). Figure 5.4 (d) shows the registered overlay of the 3D physical head textured point cloud, the image volume, and the virtual craniotomy as planned in our module. The 3DTPC-to-MR overlay is provided in a display for reference at the time of a free-hand designation of the craniotomy in physical space. More specifically, the neurosurgeon can then, without the utilization of a conventional tracker, use the visible physical pattern on the physical patient head to reproduce the virtual craniotomy on the physical mock patient head, i.e. the texture provides the physical reference for drawing the proposed virtual craniotomy on the physical head. This 'trackerless' experiment workflow is summarized in Figure 5.6.

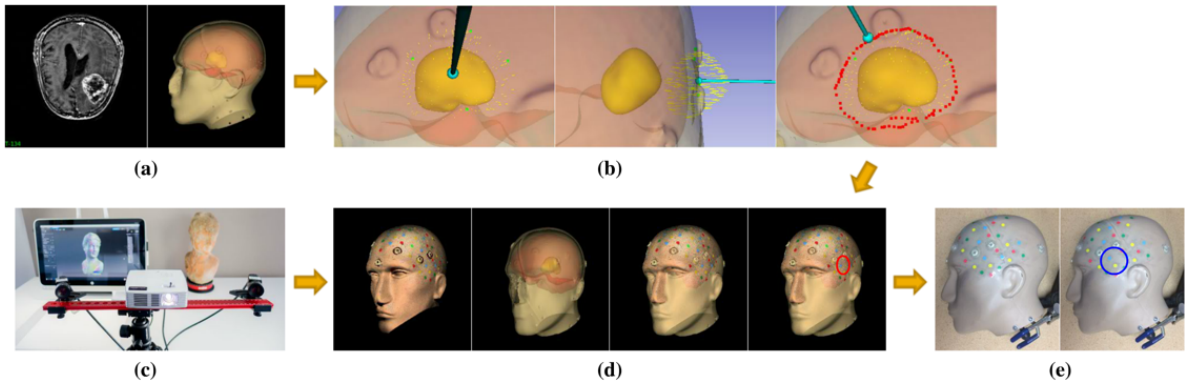

Figure 5.6: Trackerless experiment workflow. (a) Segmentation and mesh reconstruction from MR imaging data. (b) Virtual plan using our novel 'trackerless' planning system. (c) Scanning head phantom using structured light scanner [118]. (d) Register textured 3D scan model and head surface model from MRI together, and overly virtual plan contour onto the texture. (e) Neurosurgeon translates the virtual plan onto the physical head by referencing the texture dots.

5.5 Results

Using imaging data from five clinical cases that underwent resection at Vanderbilt University Medical Center (VUMC) retrieved under IRB approval (shown in Figure 5.5), the framework could be challenged under conditions involving different tumor sizes and located positions. All four experienced neurosurgeons completed conventional and virtual

craniotomy planning on the phantom manikin head. Of note, the five patient MRIs from these real surgical cases were scale-adjusted and merged into the manikin head image set and in appropriate anatomical locations for the purpose of integrating real brain and tumor presentations. Using the digitized craniotomies, the results across surgeons and cases were compared. Figure 5.7 shows the results from each trial. The green area patch is the craniotomy planned using the conventional guidance approach. The red contour represents the planned craniotomy using the virtual stylus approach. Recall, this approach is essentially the equivalent of the conventional approach but performed completely in the virtual environment. The blue contour represents the surgeons' attempt to designate the craniotomy in its true physical space using our novel 3D point cloud texture-to-MR overlay (e.g. Figure 5.4 d) as the only guiding reference only ('trackerless'), i.e. the free-hand transfer of an observed virtual craniotomy onto the mock physical patient. It should be noted that after the surgeon created the free-hand contour, the contour was digitized with a conventional tracking technology to facilitate the comparison in Figure 5.7. The quantitative metrics of comparison were the difference between centroid positions of the 'trackerless' and conventional craniotomy and area percent differences (calculated by $(|A_{trackerless} - A_{conventional}|)/A_{trackerless}$ where A is the area of each respective craniotomy region) of each case from all four neurosurgeons. The purpose of the first metric is to quantify the degree of co-localization between 'trackerless' and conventional craniotomy placement. The purpose of the second metric is to quantify the percent difference in planned conventionally-derived craniotomy size relative to the 'trackerless' realized. These metrics are plotted in the bar graphs of Figures 5.8 and 5.9 respectively, which demonstrates the virtual-to-physical craniotomy contour fidelity. The clinical contour fidelity can be evaluated by comparing virtual craniotomy planning and conventional craniotomy planning.

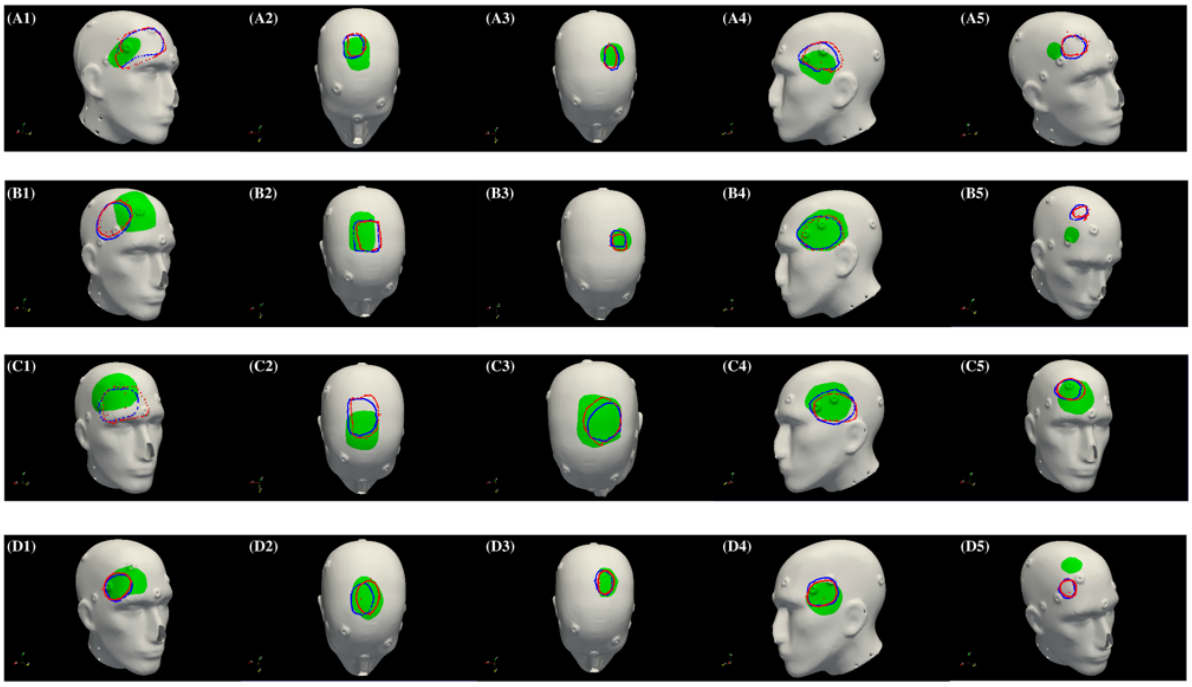

Figure 5.7: Comparison results of our novel approach, and conventional localization method in five clinical cases integrated with head phantom performed by four experience neurosurgeons (A-D). The green patch represents craniotomy planned with conventional approach. The red contour is craniotomy plan with virtual stylus planner. The blue contour is the transfer of that craniotomy plan to the physical mock subject using novel 3D point cloud texture-to-MR display and free-hand designation.

5.6 Discussion

The goal of this work is to allow the surgeon to plan a craniotomy for neurosurgery without using conventional guidance in current clinical practice. Observing Figure 5.7, we see qualitative agreement between red (virtual craniotomy using our novel display) and blue contour (designation of craniotomy plan free-hand on mock physical subject using our novel 3DTPC-to-MR display). This demonstrates that the 'trackerless' platform can be used to translate a virtual plan to a physical outcome of craniotomy designation effectively. The difference between that plan and the conventional approach (compare red/blue contour to the conventionally determined green region) is relatively consistent among cases 2, 3, and 4. However, case 1 and 5 are less consistent. Our initial hypothesis to explain the

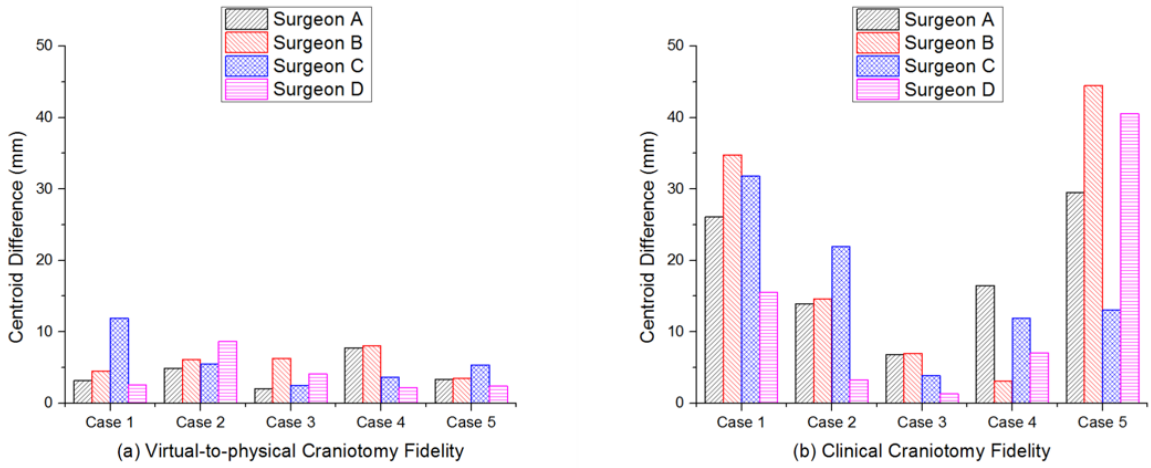

Figure 5.8: Bar plot of craniotomy planning regarding differences in centroid location expressed as a distance for each case with each neurosurgeon. (a) virtual-to-physical craniotomy centroid location difference between virtual planned contour and the translation of that contour on the physical head. (b) clinical craniotomy centroid location difference between virtual planned contour and conventionally planned contour.

disagreement was that when surgeons perform the virtual planning on a 2D screen, they may have lost the sense of the 3D nature of the physical head (see Figure 5.10a). As a consequence of the results, we simulated a real operating room in the virtual planner, we added a clamp and surgical bed, allowing the head to rotate in the range of the clamp (see Figure 5.10b). We performed another round of virtual experiment with this new version of virtual interface. Since one of the surgeons left our hospital during the experiment, the other three neurosurgeons were asked to perform this experiment. Figure 5.11 shows the comparison results of virtual planning contour with and without the clamp and surgical bed in the same five clinical cases. The red contour is craniotomy plan with virtual planning system. The purple contour is the craniotomy plan with new virtual planning system with the clamp and bed. Notice that the purple contour is once again consistent with the red except for cases 1 and 5, this suggests that adding clamp and surgical bed was not a strong influence. As additional investigation into this behavior of these two cases, neurosurgeons were asked to perform one more round of virtual and conventional planning only on case

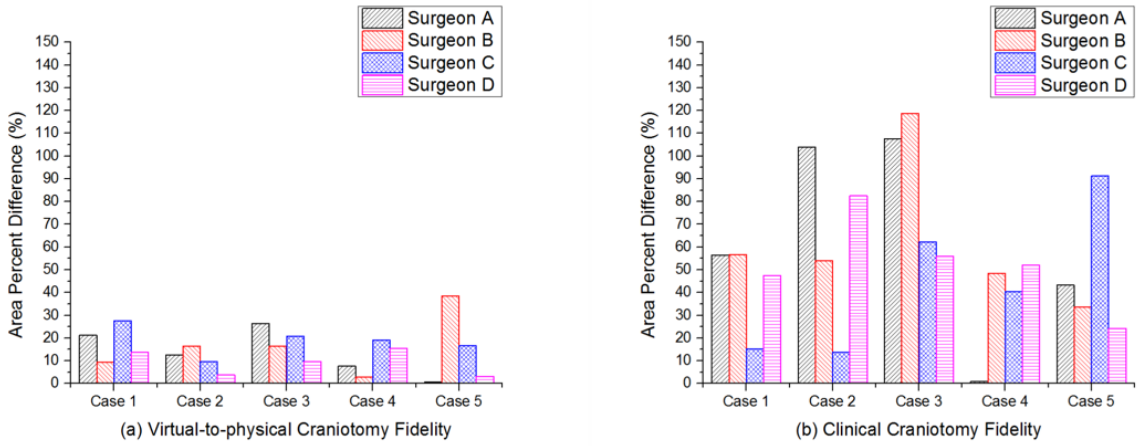

Figure 5.9: Bar plot of craniotomy planning area percent difference for each case with each neurosurgeon. (a) virtual-to-physical craniotomy area percent difference between area enclosed by virtually planned contour and the area enclosed by physical head counterpart. (b) clinical craniotomy area percent difference between area enclosed by virtually planned contour and conventionally planned counterpart.

1 and 5. Figure 5.12 compares three different rounds of virtual and conventional planning of case 1 and 5 for three of the surgeons. The conventionally planned craniotomy size and location (green patch) of case 1 is relatively consistent, while somewhat less consistent in case 5. With respect to the correlation with the virtual craniotomy plan, there is certainly more overlap between virtual and conventional plan for case 1. Case 5, however, has considerable more discrepancies (for example Figure 5.12 A5c, D5a, and D5b).

To further analyze, follow-up interviews were conducted with physicians to discuss the choices made with respect to their planning results. In preliminary experiment [119], the conventional approach was from a previous study conducted approximately one year prior [120], and the neurosurgeon claimed that his preferred surgical approach had since changed with respect to that presentation. In the extended experiment presented here, all the surgeons repeated the conventional planning. However, despite the explanation for the discrepancy and the repeating of the conventional planning, the results still appeared to undergo a similar discrepancy. One of the senior neurosurgeons, with more than 20 years

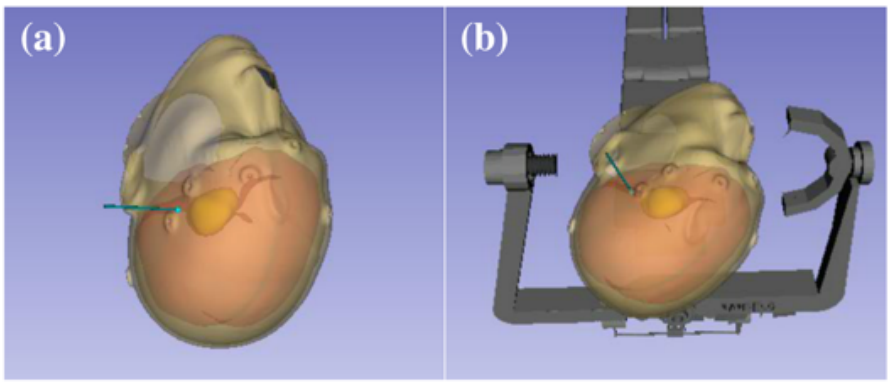

Figure 5.10: (a) Virtual planning system interface. (b) New virtual planning system adding clamp and bed to simulate real operating room.

of experience, provided his interpretation of the case 1 and 5 results. The tumor positions of case 1 and 5 make tumor localization difficult. Case 5, specifically, will not appear on all three planar views of the MRI. The neurosurgeon indicated that seeing the tumor on at least two planar views improved the craniotomy planning. This may had contributed to the differences in the planning for case 5. In case 5, the tumor was often only visible on one or two of the MRI planes. Figure 5.13 shows two examples of the virtual stylus positions in case 5. When the virtual stylus is placed on the right side, the tumor is only shown on sagittal view (see Figure 5.13a). However, moving the virtual stylus to the bottom left, the tumor is only visible in the axial slice (Figure 5.13b). As a result of this variability in determining tumor extent from imaging data, there is increased variability when planning on a small tumor when compared to planning with a larger tumor (compare case 1 and 5 in Figure 5.12). The surgeon's conclusion was that the discrepancies in case 1 and case 5 are due to a lack of anatomical landmarks (dural septa, tissue, ventricles, etc) near the two tumors. As a result, the plan for the craniotomy varied. This contrasts with cases 2 and 3 that have a dural septa reference and have a distinct trajectory for resection. What is clear is that neurosurgeons take into account various anatomical landmarks to optimize patient outcomes. In addition, a craniotomy position is selected to achieve the best tumor exposure for resection while minimizing patient harm. In case 1 and 5 there were multiple

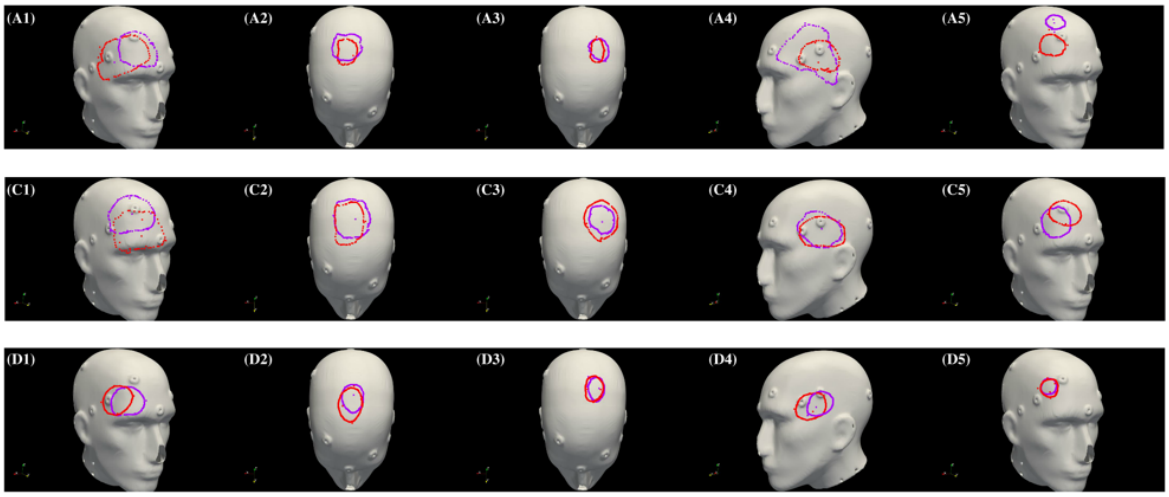

Figure 5.11: Comparison results of virtual planning contour with and without clamp and surgical bed in five clinical cases integrated with head phantom performed by three experience neurosurgeons A, C, and D (Neurosurgeon B has left). The red contour is craniotomy plan with virtual planning system. The purple one is the craniotomy plan with new virtual planning system that adds clamp and bed.

trajectories that could do this and perhaps multiple safe and effective approaches to these tumors.

There were other observations as well. Figure 5.7 also shows that some surgeons prefer different sizes of craniotomy. For example, surgeon C always plans a bigger craniotomy as compared to other surgeons. There is considerable debate in the neurosurgical literature about the appropriate size of a craniotomy. The general consensus is that the opening should allow the entire tumor to be safely visualized and resected. However different surgeons may have specific preferences beyond this practice. For example, some tumor surgeons may prefer to identify margin by separating along surgical tissue planes between the tumor and healthy brain wherever possible before removing the bulk of the tumor. Others may prefer to make a smaller approach and internally debulk the tumor before altering the surgical angles and visualizing each margin.

Another interesting finding in the preliminary experiment is that the conventional guidance method consistently provided a larger craniotomy plan. However, with the extended

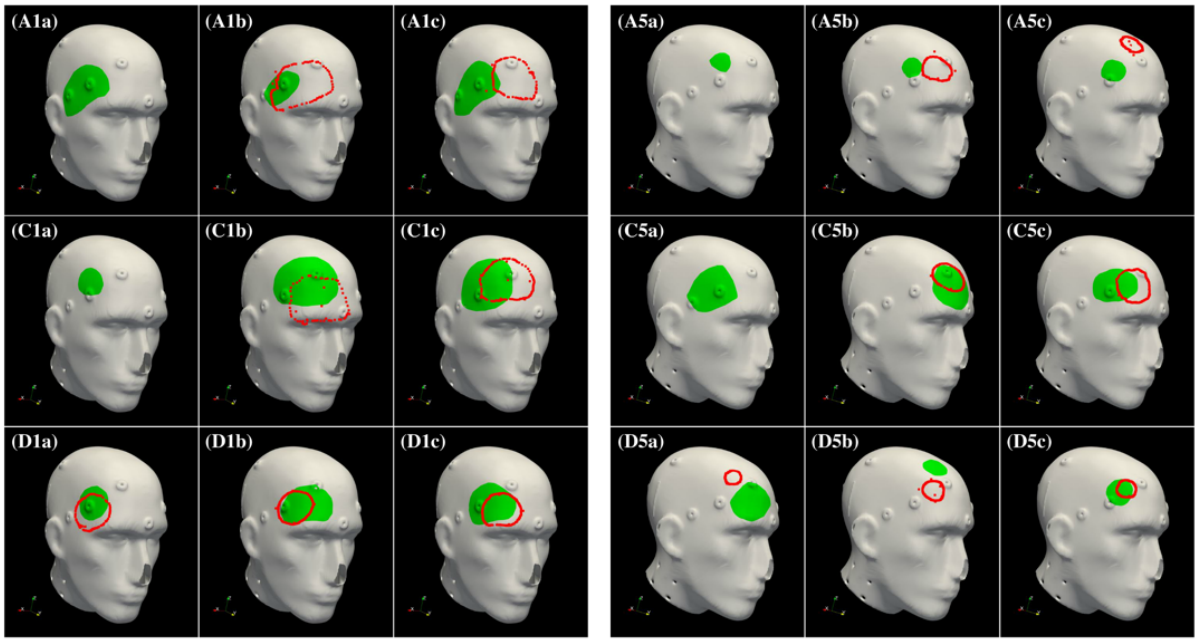

Figure 5.12: Comparison between different results of conventional planning (green area) with virtual planning (red contour). (a) Three plannings of case 1 from Neurosurgeon A, C, and D. (b) Three plannings of case 5 from Neurosurgeon A, C, and D. (Note that Surgeon A and C did not plan virtually on the first round, so there are no red contours on A1a, A5a, C1a, and C5a.)

experiment results in Figure 5.7, this finding is not repeated. Overall, the size of virtual planning and conventional contour is quite consistent. The main drawback of the proposed virtual planning system is that the anatomical structure is not obvious compared with conventional planning. In addition, it should also be stated that, as this is a new technology, undoubtedly there are still training effects as the platform itself represents a very different means of planning as well as interacting with the physical anatomy. However, in consideration of its advantages like consistent planning contours, intra-operative workflow efficiencies, and the 'trackerless' planning strategy, the participating surgeons were enthusiastic that this virtual planning method could be an alternative to conventional planning, with perhaps a noted strength for junior resident training.

While the above discussion is quite encouraging, there are certainly limitations to the

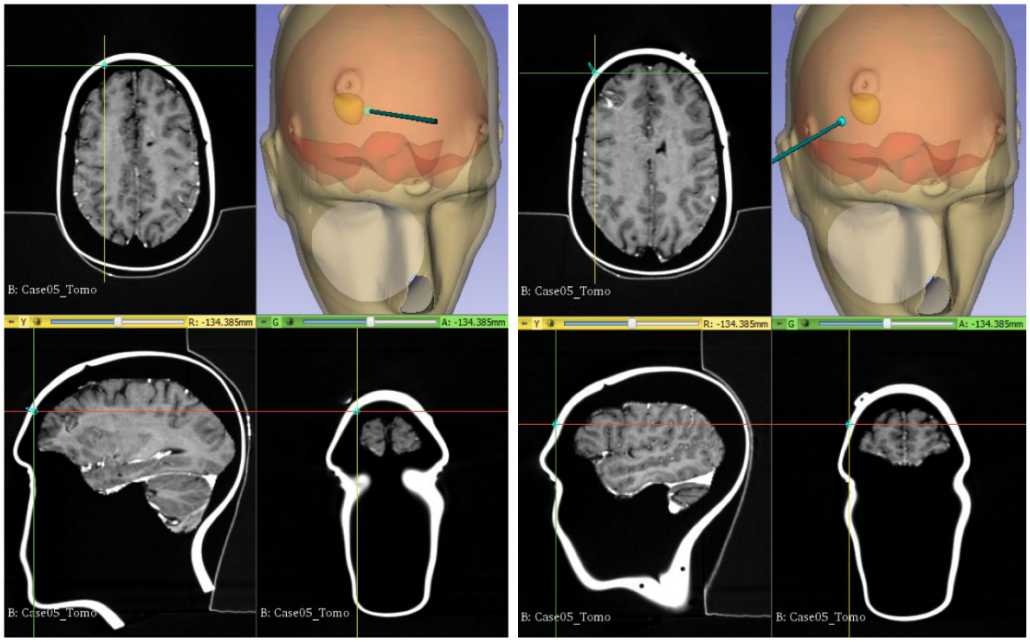

(a) **(b)**

Figure 5.13: Three image views (axial, sagittal, and coronal) and 3D view of case 5 with different location of virtual stylus. (a) Place the virtual stylus at the right side of the tumor, then the tumor is only shown on the sagittal view. (b) Place the virtual stylus at the bottom left of the tumor, and then the tumor is only shown on the axial view.

study that must be acknowledged as well as considerations from the perspective of clinical utility. Beginning with the former, it must be acknowledged that while each of the 5 cases utilized represent real pathologies and involve patients that underwent neurosurgical resection, the impact to the experiments of scaling these neuroanatomical presentations to within our phantom head cannot be ascertained. For example, if the scalp-to-brain distance became too excessive in the scaling process such that it was not realistic, the effect of such a variation on the fidelity of our results or its potential effect on clinical translation are unknown. Similarly, the phantom head is rigid as compared to the deformable patient scalp. The influence that deformability on digitization in either the conventional or 'trackerless' method is unknown. Lastly with respect to the study reported herein, it must be noted that our head presentation mock surgery setup, while similar to the operating room, still represents a considerable difference when compared to head fixation with the Mayfield clamp

which is routinely used in the neurosurgical theatre. It should be noted that none of our participating surgeons complained of these aspects, once the final mock system for testing was realized. Moving on to clinical considerations, there are several to contemplate. First, the approach would likely require a considerably shaved scalp in the region of the craniotomy, and could potentially be more extensive. From a cosmetic perspective, this could be a concern. Second, presentations that require a prone patient may be more challenging. Third, with respect to the task of creating textures to allow planning, best practices are uncertain (e.g. optimal distribution of texture, method of applying, etc.). A fourth and more intriguing aspect to consider is altering of workflow with the approach, with the 'trackerless' potentially being an improvement. More specifically, the 'trackerless' planning could be initiated at almost any time prior to surgery (assuming preoperative/diagnostic MR images are available). Theoretically, a structured light scanner is highly portable and could be used in the patient's room. Assuming a prepared scalp, textured fiducials could be applied on visible scalp areas or even inked as is commonly done. The image-to-physical registration (as shown in Figure 5.4 and 5.6) could be done immediately. The physician could plan the craniotomy in the patient's room and even share with the patient their decisions. The only requirement would be that the craniotomy texture on the patient could not be removed prior to presentation in the Mayfield clamp to preserve the plan. This should not be a problem as conventional craniotomies are planned with the scalp intact and before constructing the sterile site. It is reasonable to assert that the 'trackerless' approach would result in a better workflow and be less encumbered for 3 reasons: (1) registration between patient-textured surface and MR could be done before the patient gets to the OR, (2) similarly, the craniotomy plan could be done prior to the OR, and (3) if done prior to the OR, no registration process with a stylus has to be performed at all in the OR thus saving considerable time. If found acceptable, it would be intriguing to compare these approaches.

5.7 Conclusions

The chapter demonstrates the feasibility of using a 'trackerless' surgical image-guided system to plan and execute a craniotomy for neurosurgery. Overall, the virtual craniotomy plan provided by the approach was consistent with the conventional one. The interactive extension of 3D Slicer shown here can simplify the procedure of pre-operative planning by removing the need for conventional tracking and provide a reliable craniotomy contour. The work herein when combined with our cortical surface registration [63], cortical deformation measurement methods [66, 121], and finally computational brain shift prediction framework [62] is a powerful paradigm that could potentially eliminate the need for conventional tracking technology and usher in integrated more nimble vision-based guidance systems for neurosurgery.

Chapter VI

QUANTITATIVE MEASUREMENT OF THE CORTICAL SURFACE USING STEREO-PAIR RECONSTRUCTION WITHOUT CONVENTIONAL TRACKING TECHNOLOGY

6.1 Summary of Contributions

In this chapter, we have proposed a workflow to measure the intra-operative cortical surface using stereo-pair reconstruction without conventional tracking technology and performed model correction based on the displacement vectors. The 3D cortical surface point clouds are reconstructed from the surgical microscope pre- and post tumor resection. The same vessel feature points are designated on both cortical surface once they are registered without the need of tracking system so that the shift can be calculated. For comparison purposes, the displacement vectors are also computed via microscope tracking registration, and from the optical tracking system (use as ground-truth). All three methods are compared together after running the model correction. The comparison results demonstrate the feasibility of our method. By combining with the trackerless craniotomy planning and image-to-physical registration, the whole soft tissue shift compensation procedures can be performed without an optical tracking system.

6.2 Abstract

Intraoperative tissue deformation that occurs after brain craniotomy compromises the accuracy of modern image-guided surgery (IGS) systems. One cost-effective solution to compensate for brain shift is the utilization of a computational model-based approach leveraging intraoperatively acquired sparse data to update a pre-operative MR image of the brain. In this chapter, we propose a pipeline for quantitatively measuring intra-operative movement of the cortical surface based on stereo reconstruction from an operating microscope

without a conventional tracking system. To simulate intraoperative brain shift, a mock soft tissue phantom submerged within fluid was enclosed within a mock cranium which subsequently underwent drainage simulating conditions of brain sag. Prior to drainage, an initial reconstruction of the cortical surface was performed immediately after mock craniotomy through a stereo operating microscope. Subsequent to drainage, a second reconstruction was performed to track the subsequent motion of the cortical surface. At each stage, feature points were identified on the cortical surface and their ground truth positions were measured using an optical tracking system. The displacement error between our trackerless framework and the conventional tracking method is estimated to be 1.5 mm on average. Also, the residual error and percent correction from running the model correction are similar to the results of conventional tracking method. This demonstrates the feasibility to compensate the soft tissue shift during the tumor resection without any conventional tracking technology.

6.3 Introduction

Tumor resection surgery is currently the standard of care for brain tumor treatment. The goal is maximal tumor volume removal while minimizing the damage to the surrounding healthy tissue. Before the advent of modern medical imaging techniques, it had been difficult to estimate the size and location of the tumor. The developments of contrast agent-enhanced computed tomography (CT) and magnetic resonance imaging (MRI) have yielded the field of image-guided procedures (IGPs) that are now a standard navigation solution in modern day brain tumor surgery [3, 4]. However, surgical errors, such as incomplete resection or inadvertent damage to healthy brain tissue, can happen in the presence of brain shift when traditional procedures that rely on pre-operative magnetic resonance imaging (pMRI) or pre-operative computed tomography (pCT) to localize the position of tumor fail to account for such intraoperative changes. The fast development of three-dimensional computer vision techniques that extract cortical surface structure from optical microscope

data and correlate to the MRI counterpart could provide valuable information to assist in visualization of tumor and its relation to surrounding structures. In addition, contemporary localization systems that use optical tracking and sophisticated platforms have been developed for image-guided procedures. These platforms using optical tracking uniquely determine the position and orientation of intraoperative objects though affixed rigid bodies that consist of three or more trackable emitters. With respect to the accuracy of optical tracking devices, for example, Northern Digital Inc. (Waterloo, Ontario, Canada) reported a tracking accuracy of 0.25-0.3mm root mean square (RMS) for the tracking for individual targets [12].

In conjunction with these optical tracking devices, these platforms also consist of visualization displays. Using localization and imaging data, surgeons are able to perform an image-to-physical registration by establishing correspondence among fiducials that can be digitized both on the MRI image volume and physical patient, or by swabbing surfaces on the physical patient and their counterpart surface on the MRI. Once achieved, informative displays can be rendered in real time during surgery to assist in navigation. A consequence to these powerful platforms has been that neuronavigation is currently a standard of care in neurosurgery, and several commercial systems are available on the market such as Brainlab Curve [13] and Medtronic Stealth [14]. As alluded to above, one major concern of these systems in recent years is the recognition of the presence of brain shift during surgery and the challenge in compensating for that within navigational systems. Brain shift itself is a multi-cause event, typically arising from cerebrospinal fluid drainage, tissue swelling due to edema, tissue contraction due to hyperosmotic drugs, or tissue retraction and resection [19]. Brain shift was first identified and measured in the1980s [15–17], in a range from several millimeters up to 25 mm. Solutions like intra-operative magnetic resonance (iMR) imaging [27, 28], intra-operative computed tomography (iCT) [35, 36], and intra-operative ultrasound (iUS) [42, 43] have been proposed to compensate for brain deformation. However, deficiencies such as the high cost of iMR, ionizing radiation of iCT, and poor image

quality of iUS urge researchers to find alternative solutions. Miga et al. [51, 54, 55] proposed a cost-effective method that utilizes sparse data acquired intra-operatively to drive a biomechanical model to estimate tissue motion and update pre-operative image data.

Intra-operative surface data acquisition has been found to be an important component to driving the model updated method. In order to capture the changing shape of the brain surface, researchers have investigated the use of laser range scanners (LRS) [63, 65]. However, performing a single LRS acquisition takes about 15 to 30 seconds and the surgical operating microscope needs to be moved away from the surgical field of view (FOV). To address these workflow inefficiencies, newer techniques have been developed that extract the intra-operative surface data from the surgical microscope that is used continuously during the whole surgery [72, 75, 79]. In our previous work [82, 97, 98, 107, 108], we developed a stereovision-based integrated system that can reconstruct the 3D cortical point cloud based on the stereo-pair images extracted from the microscope. We also investigated the registration between reconstructed cortical surface geometries using microscope tracking [82] and rigid landmarks registration [97], and validated simulated brain shift with an optical tracking system. In this work, we demonstrate a framework whereby deformation-corrected image guided neurosurgery can be performed using stereo-pair microscope technology without the need for conventional optical tracking.

6.4 Methods

6.4.1 Pre-operative

Prior to surgery, patients typically receive standard contrast-enhanced pre-operative MRI or CT scans. From these images, a 3D head model can be reconstructed from the image data and also the brain and tumor model can be segmented. These reconstruction and segmentation operations were achieved in a custom surgical planning software [122]. Figure 6.1 shows the screenshot of the custom software interface that displays the three

views of the MRI image of the patient. The tumor is marked using contouring tools in each slice of the axial view so that the 3D tumor model can be extracted from the MRI. Similarly, the brain model can also be reconstructed and separated by marking the brain boundary on each slice. This collection of contours can be then used to create a 3D brain geometric model as shown in the lower right panel of the display in Figure 6.1.

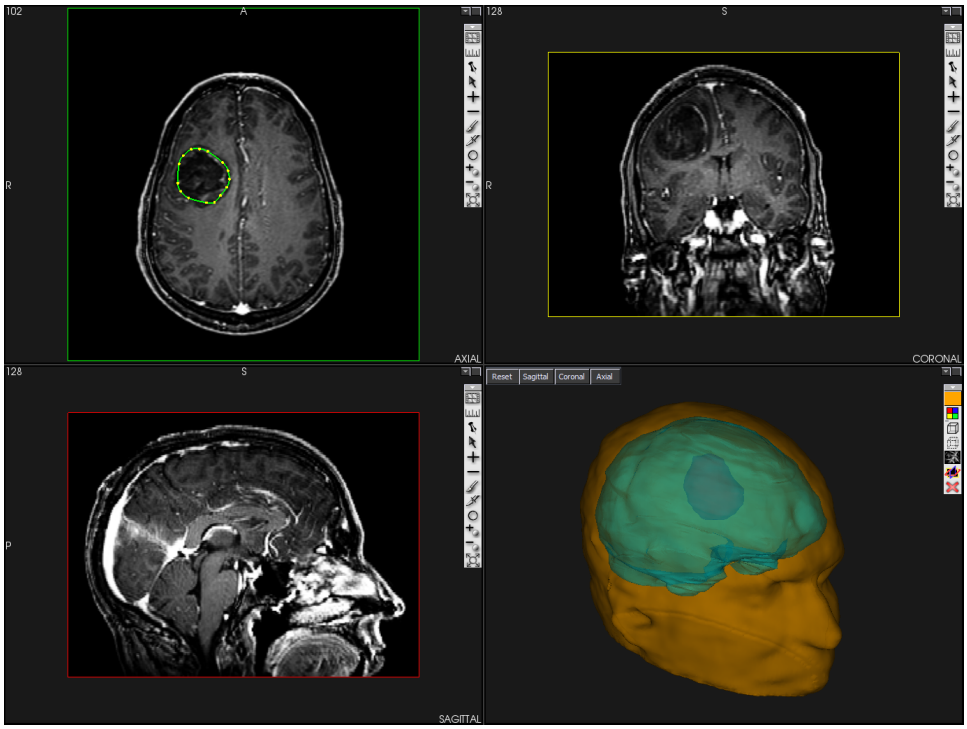

Figure 6.1: Screenshot of the surgical planning software interface displaying the three views of the MRI image data: axial, sagittal, and coronal. The tumor area is marked with the contouring tools in the axial view (top left). The separated 3D head, brain, and tumor model are rendered in the bottom right window with different colors.

The head phantom we use in this work has been directly 3d-printed from the segmented pre-operative MRI scan of a volunteer. As shown in Fig 6.2, the whole head was cut into two parts and printed separately. The lower part was printed in an ivory color material, while the upper part has been printed in black. The circular hole on the upper part was created to simulate the craniotomy. Four yellow circle adhesive markers were placed around the craniotomy and used as the rigid landmarks attached for a constant visible physical

reference to the rigid bone. Inside the head phantom is a polyvinyl alcohol (PVA) phantom (Flinn Scientific, Inc., Batavia IL) enclosed in rubber-like membrane. With respect to the phantom, a 7% solution of PVA with two freeze-thaw cycle is used to generate the brain phantom (balloon) [123]. To simulate the presence of cortical vessels visible upon craniotomy, vessel features were directly drawn on the surface of the balloon and numbered in a different color. Since the head phantom already has the craniotomy, there is no need to determine the craniotomy contour. In the context of a real clinical case, our previous work [112, 119, 124] involving a novel planner had used computer vision approaches to enable the planning of a patients craniotomy during image-guided neurosurgery without the need of conventional tracking technologies.

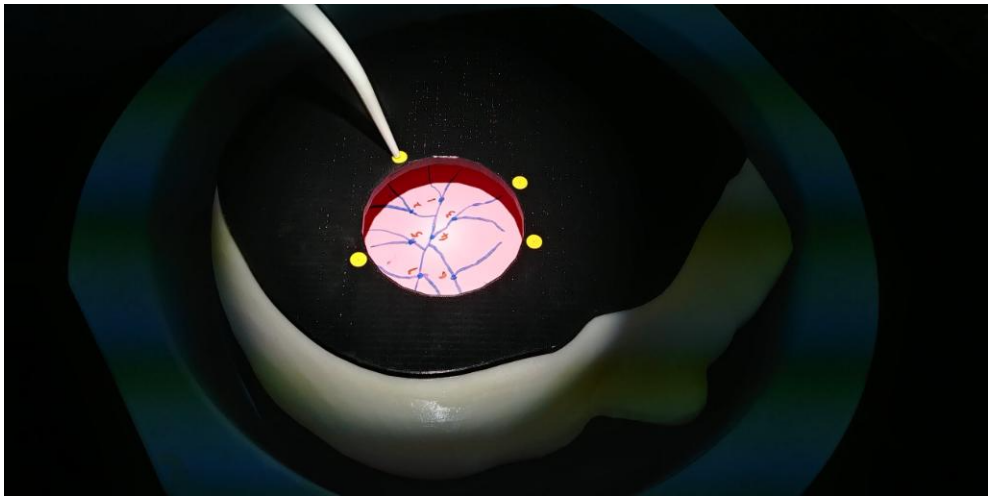

Figure 6.2: The 3d-printed head phantom with craniotomy designated and surrounding fiducial makers in microscope operating field. Inside the head phantom is the membrane-enclosed polyvinyl alcohol (PVA) phantom. The vessel features can be visualized on the surface of the phantom and numbered in a different color.

6.4.2 Mock Intra-operative Procedure

After the craniotomy contour is determined, surgeons can perform a craniotomy, open the dural septa, and expose the cortical surface. Additionally, a surgical operating microscope, e.g. OPMI Pentreo (Carl Zeiss, Inc., Oberkochen, German), can be manipulated

by the surgeons to observe the region of interest (ROI). The microscope is equipped with two charged-coupled device cameras (Zeiss MediLive Trio) with a video frame rate of approximately 30 frames per second. It also has a touch screen monitor (controlled using a joystick) that can display the video stream or images captured by the stereo-pair cameras. For this work, the graphic data was transported to a computer through an IEEE-1394b (FireWire) cable. In order to facilitate the acquisition of the image data, a user-friendly customized graphical user interface (GUI) was developed for this work [98].

Reconstruction of cortical surface geometry requires several steps: stereo camera calibration, image rectification, disparity computation, and 3D point cloud reconstruction. In our previous work [82], we developed a stereovision based integrated system that can perform all these steps in an interactive environment. This software system is written in C++ using Qt [103] with libraries such as Open Computer Vision Library (OpenCV) [96] for computer vision algorithms and Point Cloud Library [104] for display and process point cloud data. The microscope is calibrated using checkerboard at a prescribed focal length and zoom setting that covers the whole cortical surface field of view. The checkerboard pattern on the image pairs provide a number of correspondences that can be used to solve the fundamental transformation matrix [88]. The intrinsic and extrinsic parameters of the cameras can be computed based on the fundamental transformation matrix so that the stereo-pair images can be rectified. The disparity map can then be calculated by finding the differences of horizontal direction of the same features in the rectified left and right image pair using block matching (BM) algorithm [92]. Once achieved, the 3D point cloud can be reconstructed from the disparity map directly based on a projected triangulation method that is already implemented in the OpenCV SDK [96]. The 3D position of the vessel feature points that drawn on the balloon surface can be acquired directly from the reconstructed cortical surface.

Measuring the whole cortical surface movement directly with minimal workflow disruption is a challenging task. To address this, the displacement of sparse vessel features was

used to estimate tissue shift. In this work, the vessel feature points were directly imprinted on the brain phantom. In order to simulate the gravity-induced brain shift (the loss of CSF drainage during neurosurgery and subsequent brain sag), the head phantom was filled with water to submerge all except the top surface of the brain phantom. As drainage ensued simulating the CSF counterpart, a reduction in buoyancy forces ensues and the mock brain begins to deform under its own weight in the direction of gravity, very similar to the clinical equivalent.

To measure changes, 3D cortical surface point clouds were reconstructed both before and after shift occurs from the surgical microscope. These two sets of point-cloud were not in the same space since the microscope is moved during the surgical procedures. Registration between the pre- and post cortical surface geometry is necessary for the vessel displacement computation. Here, we used the surrounding visual fiducials within the microscope field of view as proposed in previous work [97]. In this work, the rigid landmarks were achieved using the four yellow adhesive markers on the cranial surface and served as a rigid reference allowing for absolute brain shift measurements. For comparison purposes, the microscope tracking registration was also performed here to register the reconstructed point cloud together. To realize this, an image-to-physical registration was performed using a Polaris Spectra optical tracking system developed by Northern Digital, Inc. (Waterloo, Ontario, Canada) to register the physical head of the patient directly to the MRI head model. Several anatomical feature points were designated on the physical head using a tracked probe on the bridge of the nose, left eyebrow, right eyebrow, root of the nose, and forehead area. These feature points serve as correspondences for an initial point-based registration and then followed with an ICP for the refinement [61]. This process aligns the patient physical head with the MRI image data. Figure 6.3 shows the process of the registration. The monitor displays the interface of image-to-physical registration in a neuronavigation guidance system. Both the pre- and post cortical surface were transformed to the image space by optically tracking of the microscope in lieu of the visi-

ble reference markers. More specifically, an optically-tracked reference body (Microscope Tracking Array, BrainLab Inc., Westchester, Illinois) was attached on the microscope so that the physical position in the world coordinate system could be known via an optical tracking system (see Fig. 6.3). This allows the cortical surface point clouds reconstructed before and after brain shift to be transformed into the same space as described in detail in a previous publication [82]. For additional comparison purposes, each of the vessel features was also separately digitized using an optically tracked stylus in direct contact with the features before and after mock shift, which served as ground-truth values.

Figure 6.3: The experiment settings in the operating room (OR). The phantom is placed under the surgical operating microscope. A tracked rigid body tracking star is attached on the microscope to permit tracking of the microscope position. The monitor displays the interface of image-to-physical registration in a neuronavigation guidance system.

After the pre- and post cortical surface geometry were registered into the same space, the displacement of the designated corresponding vessel feature points can be calculated. Based on two registration methods (rigid landmark registration and microscope tracking registration) that align the pre- and post cortical surface, two sets of the shift were measured; the ground-truth displacement was assumed to be the direct measurement using the optically tracked stylus. These intra-operative measurements, specifically three sets

of intra-operative displacement vectors (i.e. through methods of rigid landmark registration, microscope tracking registration, and optically tracked stylus), were used to drive a finite element methods (FEM) based modeling approach to compensate for brain shift [51]. More specifically, the patient-specific finite element mesh was generated based on the surface mesh from the volume segmentation. The information about the head orientation, size and location of the craniotomy were included to produce the boundary conditions. Then, the atlas (collection of deformations) was pre-computed using the model with driving conditions associated with brain sag which in this case represents a reduction of buoyancy forces associated with the fluid-submerged mock brain tissue (performed by draining the surrounding fluid from the brain phantom enclosure). The measured intra-operative displacements were used and an inverse solution was applied to minimize the least-squared error between model predictions and measurements [125]. More details about the correction methods used in this work were described in previous publication [126]. To validate the quality of the model prediction, each set of the vessel feature displacements were used as the input data source to drive the pre-computed atlas deformation. For validation, ground truth measurement was compared to their model predicted counterparts generated via different methods, namely rigid landmark registration and microscope tracking registration.

6.4.3 Experimental Procedure

The PVA phantom experiment was performed in the operating room (OR) at Vanderbilt University Medical Center (VUMC). Figure 6.3 shows the experiment setting in the OR. The intra-operative procedure steps are as follows:

1. With phantom secure, perform face-based surface registration using custom registration software.

2. Acquire unobstructed stereo pair images (record zoom and focus), and record microscope position from optically attached reference target.

3. Digitize the four adhesive markers (rigid landmarks) around craniotomy and seven vessel feature points on the mock phantom with tracked stylus.

4. Fill phantom with mock CSF fluid until the phantom is near completely submerged.

5. Move microscope to another position.

6. Repeat step 2 and 3.

7. Calibrate the stereo-pair cameras using the checkerboard calibration pattern.

We note that rather than beginning with the submerged phantom and draining the phantom, performing the drainage effect in reverse was a simple way to avoid excess phantom handling. In order to compute all three forms of displacements, the post-processing protocol steps are shown as below:

1. Reconstruct the pre- and post cortical surface point cloud respectively.

2. Designate the four adhesive markers around craniotomy and seven vessel feature points from both pre- and post cortical surface point cloud.

3. Compute the vessel feature displacements based on the rigid landmark registration.

4. Use the four adhesive markers to calculate the microscope tracking transform matrix, transform the pre- and post cortical surface to same space and compute the vessel displacements based on microscope tracking registration.

5. Calculate the vessel feature displacements directly from the measurements of optical tracking system.

6. Run the image correction pipeline using all three sets of vessel feature displacements respectively.

6.5 Results

The stereo-pair cameras of the microscope were calibrated using a planar checkerboard that has 8 by 6 corners with a block size 7 mm. The chessboard images needs to be placed in different positions and orientations that cover the whole field of view. The average epiline error is 0.3 pixels, and the stereo-projection error is reported as 0.4 pixels. Figure 6.4 shows the displacement vector of each vessel feature point: blue vectors are calculated by registering the reconstructed point clouds using rigid landmarks registration (see Figure 6.4 a), while red arrows are using microscope tracking registration (see Figure 6.4 b). The use of ground truth values from the tracking system are drawn in green in both of the left and right figures. Table VI.1 shows the displacement value of ground-truth (measured from tracking system), displacement calculated from point cloud based on rigid landmarks registration (RLR) and microscope tracking registration (MTR) respectively. The mean error of displacement of using rigid landmarks registration is about 2.1 mm, and using microscope tracking registration is approximately 4.7 mm. Table VI.2 shows the model performance and displacement data from three sets of data (via NDI tracking system, rigid landmark registration, and microscope tracking registration). The residual error and percent correction of model prediction are calculated by comparing to each model driving measurement. All model predictions are compared to measurement via NDI (used as ground-truth) so that the residual error and percent correction are shown. These results demonstrate that the deformation-corrected image guided neurosurgery can be performed using stereo-pair reconstruction without the need for conventional tracking.

6.6 Conclusions

In this work, we proposed a workflow to measure the intra-operative cortical surface using stereo-pair reconstruction without conventional tracking technology and performed

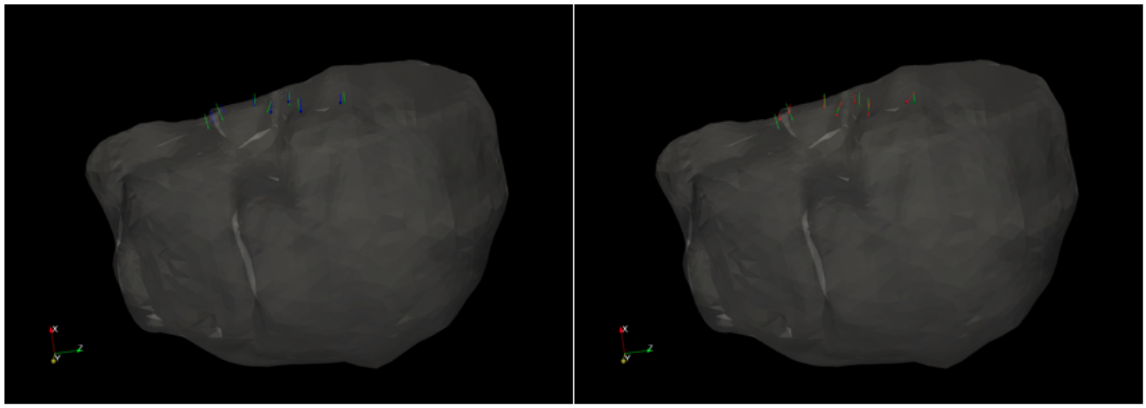

Figure 6.4: The displacement vector of each vessel feature point. The ground truth values from tracking system are drawn in green. (a) Blue vectors are calculated by registering the reconstructed point clouds using rigid landmarks registration. (b) Red vectors are using microscope tracking registration.

model correction based on the displacement vectors. The 3D cortical surface point clouds are reconstructed from the surgical microscope pre- and post tumor resection. The same vessel feature points are designated on both cortical surface once they are registered without the need of tracking system so that the shift can be calculated. For comparison purposes, the displacement vectors are also computed via microscope tracking registration, and from the optical tracking system (used as ground-truth). All three methods are compared together after running the model correction. The results indicate that our trackerless method performs close to the displacement directly measured from tracking system (used as ground-truth), and better than values based on microscope tracking registration. The errors of the trackerless method mainly come from the point cloud reconstruction and rigid landmark registration. The process of calculating microscope tracking accumulates more error so that it performs worse than trackerless method. To reduce the error, we can improve the quality of cortical surface reconstruction and minimize the registration error. Overall, the comparison results demonstrate the feasibility of our method. By combining with the trackerless craniotomy planning and image-to-physical registration, the whole soft tissue

Table VI.1: The displacement value of ground-truth (measured from NDI tracking system), displacement calculated from point cloud based on rigid landmarks registration (RLR) and microscope tracking registration (MTR) respectively. The angle between vectors and magnitude of difference are also calculated (All metrics are in mm unit except for angle that is in degree).

Target	Disp. via NDI	Disp. via RLR	Angle	Error	Disp. via MTR	Angle	Error
1	[2.0, 0.4, 3.4]	[0.7, 0.7, 3.5]	19	1.3	[-2.0, 3.7, 3.0]	67	5.2
2	[2.1, 0.6, 3.9]	[2.5, 0.8, 4.8]	1	1.0	[-0.9, 1.9, 6.3]	36	4.0
3	[2.3, 1.2, 4.8]	[1.2, 0.2, 3.1]	10	2.2	[-1.6, 0.5, 3.7]	48	4.1
4	[3.6, 1.0, 2.6]	[3.2, 1.0, 3.7]	13	1.1	[-2.4, 3.4, 4.9]	75	6.8
5	[2.6, 0.9, 4.8]	[-0.4, 0.0, 4.2]	35	3.1	[-1.9, 1.2, 5.1]	48	4.5
6	[1.0, 0.5, 7.0]	[1.8, -0.7, 3.2]	25	4.0	[-1.8, 1.6, 3.6]	37	4.5
7	[1.3, 0.8, 5.8]	[1.6, -0.1, 3.8]	13	2.2	[-2.0, 0.9, 3.2]	44	4.2
Mean Error	-	-	-	2.1	-	-	4.7

shift compensation procedures can be performed without an optical tracking system.

Table VI.2: The model performance of displacement data from NDI tracking system (used as ground-truth), displacement calculated from point cloud based on rigid landmarks registration (RLR) and microscope tracking registration (MTR) respectively. The model driving measurement of each set are compiled into the atlas so that model predictions are calculated. Residual error of model prediction (average residual error $\pm$ standard deviation of the error), percent correction of model prediction (average percent correction $\pm$ standard deviation of percent correction) are listed. The model prediction values are also compared to the measurement via NDI stylus points (ground-truth), and residual error, and percent correction are shown (All metrics are in mm unit except for percent correction that is in percentage).

Metrics	Disp. via NDI	Disp. via RLR	Disp. via MTR
Model Driving Measurement	5.4 ± 1.1	4.3 ± 0.8	5.2 ± 1.1
Residual Error of Model Prediction	2.5 ± 1.4	1.7 ± 0.5	2.2 ± 0.6
Percent Correction of Model Prediction (%)	53.3 ± 26.9	60.7 ± 10.9	57.8 ± 11.1
Measurement via NDI (Ground-truth)	5.4 ± 1.1	5.4 ± 1.1	5.4 ± 1.1
Residual Error	2.5 ± 1.4	2.8 ± 1.6	3.4 ± 1.4
Percent Correction (%)	53.3 ± 26.9	47.4 ± 29.3	36.0 ± 25.4

Chapter VII

POTENTIAL ALTERNATIVE COMPUTER VISION APPROACHES & EXTENDED APPLICATION - INITIAL EXPERIENCE WITH USING A STRUCTURED LIGHT 3D SCANNER AND IMAGE REGISTRATION TO GUIDE BEDSIDE SUBDURAL EVACUATION PORT SYSTEM (SEPS) PLACEMENT

7.1 Summary of Contributions

This chapter evaluates the feasibility and accuracy of a bedside navigation system that relies on visible light-based 3D scanning and image registration to a pre-procedure CT scan. The information provided by this system may ease the selection of optimal burr hole location for SEPS placement, compared to selection based on measurements by hand. In Part 1, the accuracy of this system was evaluated with a rigid 3D printed phantom head with implanted fiducials. In Part 2, the navigation system was tested on 3 patients who underwent SEPS placement. The error in registration of this system was less than 2.5mm when tested on a rigid 3D printed phantom head. Fiducials located in the posterior aspect of the head were difficult to reliably capture. For the 3 patients who underwent Subdural Evacuation Port System (SEPS) placement, the distance between anticipated SEPS burr hole location based on registration and actual burr hole location was less than 1cm. A bedside cranial navigation system based on 3D scanning and image registration has been demonstrated with acceptable accuracy. Such a system may increase the success rate of bedside procedures, such as SEPS placement. However, technical challenges such as the ability to scan hair and practical challenges such as minimization of patient movement during scans must be overcome.

This chapter is an extended application of the interactive extension proposed in Chapter V. And it is a collaborative work with Dr. Hansen Bow who is currently a neurosurgery resident at Department of Neurological Surgery, Vanderbilt University.

7.2 Introduction

Evacuation of a chronic subdural hematoma (CSDH) is one of the oldest and most effective procedures in neurosurgery [127]. Although this procedure is most commonly performed in the operating room, bedside drainage without the use of general anesthesia has been utilized in select patients since the 1970s [128]. A more recent advance in bedside CSDH evacuation involves the subdural evacuation port system (SEPS, Medtronic, Inc.), which was introduced in the early 2000s [129]. SEPS utilizes a twist drill burr hole, through which a hollow screw is then threaded and connected to a Jackson-Pratt style suction reservoir. Purported benefits of this system include the treatment for elderly and sick patients who would otherwise not tolerate general anesthesia [130], decreased bleeding, decreased total treatment cost, and decreased hospital length of stay [131].

The optimal location for burr hole and screw placement is the point of greatest thickness of the subdural collection [129, 130]. Identifying this location on the patient's scalp based solely on the pre-procedure CT scan and anatomical landmarks can be challenging, especially for junior neurosurgery residents who most frequently perform these procedures [132]. To improve the accuracy of this procedure at our institution, a fiducial is often affixed to the patient's head at the proposed burr hole location. A pre-operative CT scan is then obtained, and the location of the fiducial is compared to the location of maximal CSDH thickness. Adjustments are then made to the proposed burr hole location prior to the actual bedside surgical procedure. Although this method increases the accuracy of burr hole placement, it requires an additional CT scan and delays care.

This chapter presents a preliminary evaluation of both the accuracy and clinical workflow of using a visible light-based 3D scanner and image registration to guide SEPS placement. The information that is generated from this system is similar to that of a CT scan with a fiducial placed at the proposed burr hole location. Benefits of this system compared to obtaining a second CT scan with fiducial placement may include decreased cost to the healthcare system, avoidance of radiation exposure, and expedited neurosurgical interven-

tion.

7.3 Methods

Testing of the navigation system consisted of two parts. The first part assessed the accuracy of registering a visible light-based 3D scan to a CT scan in an ideal, simulated setup. A 3D printed plastic head phantom with implanted fiducials was used to evaluate the error between marked locations on the 3D scan and the actual locations on a CT scan. The second part focused on the feasibility and accuracy of using the navigation system on three patients with CSDHs who underwent SEPS placement. The IRB approved this study under 45 CFR 46.110 (F)(1), (5), and (6), as the study posed minimal risk to participants.

7.3.1 Part 1: Accuracy Evaluation Using a Plastic Head Phantom With Implanted Fiducials

A 3D printed hollow plastic head was created using the methods described in a prior publication [133]. In brief, a CT scan of a ”normal” person’s head was obtained from an online DICOM image library (OsiriX, Pixmeo, Bernex, Switzerland). The 2-dimensional DICOM images were converted into 3D-printable format and printed on a 3D printer. Seven 3mm diameter titanium screws were driven into each side of the head (Figure 7.1a, 7.1b). Four were implanted superior to the superior temporal line, with the remainder implanted in the temporal bone. No screws were implanted in the midline or posterior fossa, as these are unlikely locations for a CSDH. A CT scan was obtained of the head at 0.8mm slice thickness and reconstructed in 3D using Invesalius 3.0 (Invesalius, Information Technology Center Renato Archer, Amarais, Brazil) (Figure 7.2a).

Ten 3D scans using the visible light-based DAVID SLS-3 3D scanner (DAVID Vision Systems, Koblenz, Germany) were obtained of the right side of the head (Figure 7.2b). The scanner works by projecting various patterns of light through a standard multimedia projector. A camera at a fixed distance and angle with respect to the projector captures

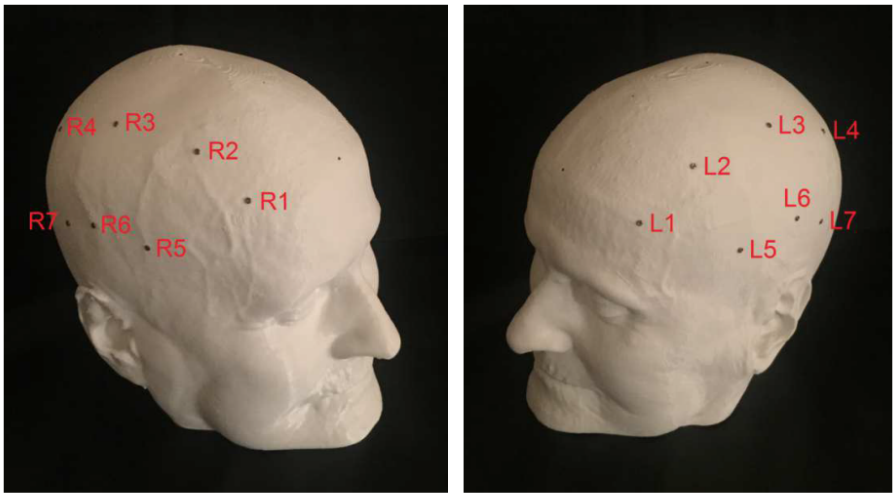

Figure 7.1: (a) Photograph of the right side of the 3D printed phantom, with fiducial locations labeled in red. The fiducial was a titanium screw with a 3mm head diameter. (b) Photograph of the left side of the phantom.

these patterns. An algorithm then generates a three dimensional surface based on the information the camera provides. Each scan was taken from a different location at a distance of approximately 50cm and at a location anterior, to the right of, and superior to the head. These locations captured the topologically rich facial features that are necessary for image registration. The different locations were intended to replicate realistic scenarios in which the location of the scanner relative to the patient's head is difficult to specify precisely. The same steps were repeated on the left side of the plastic head.

The results of the 3D scans were color surfaces in Stereolithograph (STL) file format (Figure 7.2c). To register the 3D scan to the CT scan, coarse anatomical point correspondences (e.g. nose, lateral canthus, and tip of the ear) were manually selected. Then a rigid registration using the method of Horn [134] was performed. Lastly, an iterative closest point surface registration [135] was calculated for refinement (Figure 7.2d). The registration process took approximately 1 minute.

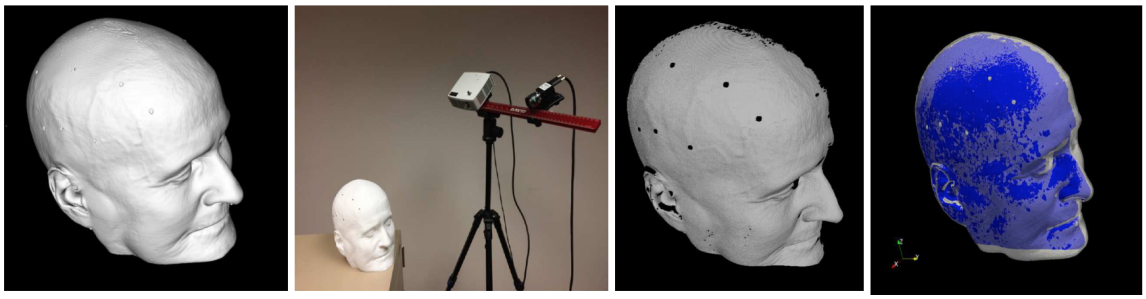

Figure 7.2: (a) 3-dimensional reconstruction of a CT scan of the phantom. (b) The DAVID SLS-3 3D scanner positioned to scan the phantom's left side. At the top of the tripod stand, the multimedia projector is on the left, and the high resolution video camera is on the right. Both are connected to a laptop (not displayed). (c) The 3- dimensional scan of the phantom's right side. The scan is in color. The screws appear as black holes in the scan due to their reflective properties. (d) Registration between the visible light-based 3D scan (blue) and the CT scan (gray). Areas in dark blue are areas where the 3D scan is closer to the observer, while areas in light blue are areas where the CT scan is closer to the observer.

7.3.2 Part 2: Feasibility and Accuracy of Using the Navigation System on Patients With CSDH

The system presented here aims to provide similar information to obtaining a CT scan with a fiducial placed at the proposed burr hole location. The intended workflow of the system involves shaving the patient's head at the location of the proposed burr hole. Then an "X" is made on the patient's scalp with a marking pen to enable identification by the visible light-based color 3D scanner as an initial working target. The 3D scan is then taken of the patient's head, with the "X" included in the scan (Figure 7.3a). The scanned surface is then registered to the patient's presenting CT scan with the CSDH, and axial, coronal, and sagittal cross sections corresponding to the center of the X are generated (Figure 7.3b). Based on this information, the location of the actual burr hole can be planned relative to the location of the marked "X".

To test the workflow and accuracy of this system, three CSDH patients were recruited. After consent was obtained, the general area close to the presumed location of the CSDH

was shaved. An ”X” mark was made with a surgical marker at the proposed location of skin incision and subsequent burr hole placement. At this time, a 3D scan of the patient's head was obtained. The scanning time was approximately 7 seconds. The SEPS placement then proceeded according to previously published protocols [129]. Specifically, the ”X” mark made by the surgical marker specified the center of the actual skin incision and subsequent burr hole placement. The guidance information was not made available to the proceduralist at the time of SEPS placement due to the IRB requirement that navigation results not influence medical decision making.

The distance between the anticipated burr hole location on the patient's skull and the actual location was used to evaluate the registration accuracy and utility of the guidance information. In essence, this is the error between where the proceduralist expects the burr hole to be based on navigation information and where it actually is after completion of the procedure. To calculate the anticipated burr hole location, the pre-procedure CT scan (Figure 7.4a) was registered to the 3D scan of the patient's scalp (Figure 7.4b) using the methods described in Part 1 (Figure 7.4c). The anticipated burr hole location was calculated as the closest point of the patient's skull to the center of the ”X” mark on the patient's scalp, as described in prior publications [119, 124]. The accuracy of this point was fundamentally dependent on the quality of registration between the 3D scan and the pre-procedure CT scan.

A post-SEPS removal CT scan was preferentially used to determine the actual location of the burr hole drilled into the skull. If one were not available, a CT with the SEPS drain in place was used. The actual burr hole location was defined as the center of the hole (or screw) on the surface of the skull in the post-procedure CT scan. The post-procedure skull was then registered to the pre-procedure skull using the methods described in Part 1. The error in registration between the skulls was less than 1mm, as it is the registration between two rigid bones. Then the distance between the anticipated burr hole location (projected onto the pre-procedure skull) and the actual burr hole location (marked on the

post-procedure skull) was calculated.

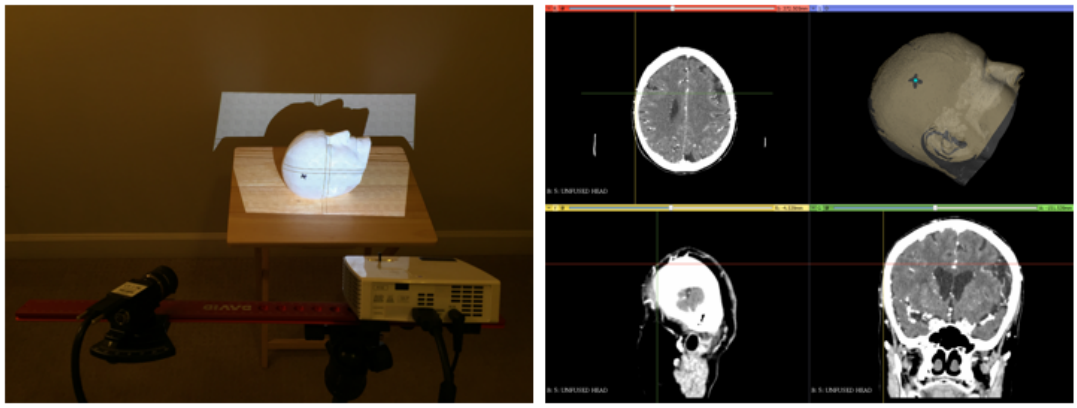

(a) (b)

Figure 7.3: Demonstration of the workflow of the 3D navigation system. (a) The proposed location of the burr hole is marked as an ”X” using a surgical marker. The patient’s head is scanned by the visible light-based 3D scanner. (b) After aligning the 3D scan with the pre-procedure CT scan, a navigation panel is presented, with coronal, sagittal, and axial views of the proposed burr hole location. The top right pane shows the alignment between the 3D scan and the CT scan. The panels are scrollable. The actual location where the burr hole will be drilled can be either the center of the ”X” mark or adjusted based on the registration data presented in these panes.

7.4 Results

For Part 1 on the right side of the phantom, the mean error for each of the fiducials is listed in Table VII.1. Only 3 of the 10 scans were able to capture Point 4, which was located in the parietal-occipital area. Also, only 8 of the 10 scans were able to capture Point 7, which was located in the posterior temporal-occipital area. Also, only 8 of the 10 scans were able to capture Point 7, which was located in the posterior temporal-occipital area. The mean error for each of the fiducials that were captured by all 10 scans was less than 2.0mm.

The results for the left side of the phantom are also listed in Table VII.1. Only 6 of the 10 scans were able to capture Point 4. The mean errors for each of the fiducials that were captured by all 10 scans was less than 2mm. For each of the errors calculated for each of

the fiducials, the largest error was 2.25mm. Table VII.1 lists the errors calculated for the 10 registrations on the right and left side of the phantom.

Table VII.1: Registration error between the actual and calculated locations of the fiducials illustrated in Figure 7.1. The average, standard deviation, and maximum errors are presented. All measurements are in millimeters. If not all 10 scans captured the fiducial location, a - was entered on the table. Avg Error, average error; Std Dev, standard deviation; Max Error, maximum error.

No.	Avg Error	Std Dev	Max Error	No.	Avg Error	Std Dev	Max Error
R1	1.07	0.35	1.87	L1	1.2	0.47	1.71
R2	1.21	0.23	1.76	L2	0.95	0.26	1.47
R3	0.85	0.44	1.94	L3	1.1	0.22	1.52
R4	-	-	-	L4	-	-	-
R5	1.01	0.39	1.8	L5	1.28	0.57	2.25
R6	1.02	0.3	1.61	L6	1.27	0.37	1.99
R7	-	-	-	L7	1.57	0.45	2.22

For Part 2, obtaining a 3D scan of the patient's shaved and marked head was more difficult than anticipated. Patients with CSDH frequently exhibited altered mental status and had difficulty holding their head still for even the 7 seconds needed to obtain the 3D scan. Initially, approximately 5 minutes were needed to obtain a successful scan. For later scans, an assistant held the patient's head during the scan. The assistant's hands were out of view of the 3D scanner. Information regarding the patients and their CSDHs is listed in Table VII.2. Figure 7.4d illustrates the navigation panel that can be generated after registration between the visible light-based 3D scan and the CT scan.

The distances between the anticipated burr hole location and the actual burr hole location are also listed in Table VII.2. Notably, the error in distance was less than 1cm for all 5 SEPS drains placed.

7.5 Discussion

Navigation systems for bedside procedures have not advanced as rapidly as those for procedures in the operating room. At the authors institution, one method of increasing the

Table VII.2: Information about the CSDHs of the three patients. The size of the CSDH was in cm and measured the anterior-posterior and superior-inferior lengths along the surface of the skull. The method of surgical planning was also noted. For Patient 1, the Axiem Stealthstation was brought to the patient's room and used. For Patient 3, a fiducial was taped on the patient's head at a proposed location, and a repeat CT head was obtained, as shown in Figure 7.4. Patients 1 and 2 had 2 SEPS drains placed simultaneously due to the size of the CSDH. The errors in anticipated vs actual locations of the burr holes was calculated as described in the text.

Patient	Location	Size	Method	Burr Hole	Error (mm)
1	L Frontal, Parietal	13x7.5	Axiem Stealthstation	Anterior	1.56
				Posterior	2.54
2	R Frontal, Parietal	10x5.5	Ruler, Landmarks	Anterior	3.31
				Posterior	9.55
3	R Parietal	8.5x5.5	Fiducial, Repeat CTH	Center	6.03

accuracy of burr hole placement at the bedside involves obtaining a CT scan with a fiducial placed at the proposed burr hole site. Here, we evaluate the feasibility of using a visible light-based 3D scanner and image registration to guide SEPS drain placement for CSDHs. The navigation information provided by this system is made to resemble that of a CT scan with a fiducial located at the proposed burr hole site. Adjustments to the proposed incision site can be made by either measuring the change in distance using a ruler or repeating the registration process with a new "X" mark.

Part 1 involved a simplified test situation to evaluate the accuracy of the system presented here. The phantom's surface was rigid and uniform in color. The available errors in registration were all less than 2.5mm and compare favorably with other methods of registration in neurosurgery [127]. The 3D scanner was unable to capture some of the posterior fiducials in several of the scans, which resulted in error values that were not available. Registration error in posterior locations is an inherent limitation of optical registration systems, which are reliant on the rich topographical anatomy of the face [136].

In Part 2, the navigation system was tested in a clinical setting. The difficulty in having the CSDH patients hold his or her head still for 7 seconds was not anticipated. Multiple attempts at scans were made, eventually concluding with having an assistant hold the

patient's head still while being out of view of the 3D scanner. The single 7-second scan initially took about 5-10 minutes to complete due to patient non-cooperation. However at the end of our study, obtaining the scan took 1-2 minutes.

To evaluate the registration accuracy in a clinically relevant setting, the authors selected the distance between the anticipated burr hole location given by the "X" mark on the skin and the actual burr hole location.There were several sources of error in the calculated distance between the anticipated and actual burr hole location on the skull. The first source was the alignment of the visible light-based 3D scan and the pre-procedure CT scan. This was the most important source of error that was evaluated. The second source was the calculation of the anticipated burr hole location based on the surface "X" mark. This calculation assumed that the drill bit for the burr hole was perpendicular to the skin surface, which was generally true. The third source of error was the alignment of the post-procedure skull CT with the pre-procedure skull CT, in which the coordinates of the anticipated burr hole were calculated. This alignment error is negligible, as it is an alignment between two rigid bones. The distances between the anticipated and the actual burr hole locations were 1.56, 2.54, 3.31, 9.55, and 6.03 mm, Table VII.2. All were less than 1 cm. The sizes of CSDHs were typically several centimeters in length and width. The errors that were reported would then be acceptable for SEPS placement.

Prior studies have investigated the use of optical surface scanning to register patient-space information with image-space data. One of the first navigation devices to use optical surface registration involved a camera capturing the red dot of a laser pointer that is directed by the surgeon[136, 137]. Laser range scanners could be used to automate the movements of the laser [63, 67]. Most recently, commercially available visible light-based 3D scanners have been used to semi-automate the contact-based registration method that is commonly used [138]. Our study is the first to evaluate the use of a visible light-based 3D scanner to assist a bedside procedure in neurosurgery, the first clinical evaluation of 3D scanning for SEPS placement, and the first to use pen ink as a localizing fiducial.

Limitations of this study include the small number of patients, the inability to confirm registration during the procedure once the patient's face has been draped, and the absence of feedback from the proceduralist regarding the usefulness of the guidance information.

In a more general sense, there are several challenges with using 3D scanning and image registration for neurosurgical planning. Two challenges include surfaces that are difficult to capture by 3D scanning and surfaces that are changed with respect to the pre-procedure CT scan.

Human hair is difficult for structured light 3D scanners to capture due to both the resolution of the scanner and hair's reflective properties [139]. Hair also cannot be used as a surface for registration due to it not appearing on the pre-procedure CT scan. In this study, a patch of hair was shaved around the proposed burr hole entry site. The skin surface at this area combined with facial features allowed the surface registration to be successful. At the authors' institution, the shave for SEPS drain placement is generous, enabling visible light-based 3D scanning and registration to work. However at other institutions, if the shave is minimal, visible light-based 3D scanning may not be successful.

Another challenge of using visible light-based 3D scanning involves surfaces that are obscured or deformed with respect to the pre-procedure CT scan. Examples include a Mayfield head-holder, eyelid tape, or intubation tubing. In the study presented here, the patient was awake and not intubated. Facial features were then available for use as registration landmarks. However, the workflow demonstrated here may be difficult to generalize to other bedside procedures or surgeries in the operating room due to the reasons mentioned above.

7.6 Conclusion

In conclusion, this chapter presents a navigation system using visible light-based 3D scanning and image registration for SEPS placement, a bedside procedure in neurosurgery. This system may provide a safety-net for junior residents to more accurately perform this

procedure, while decreasing costs due to misplacement or CT scans guiding optimal placement.

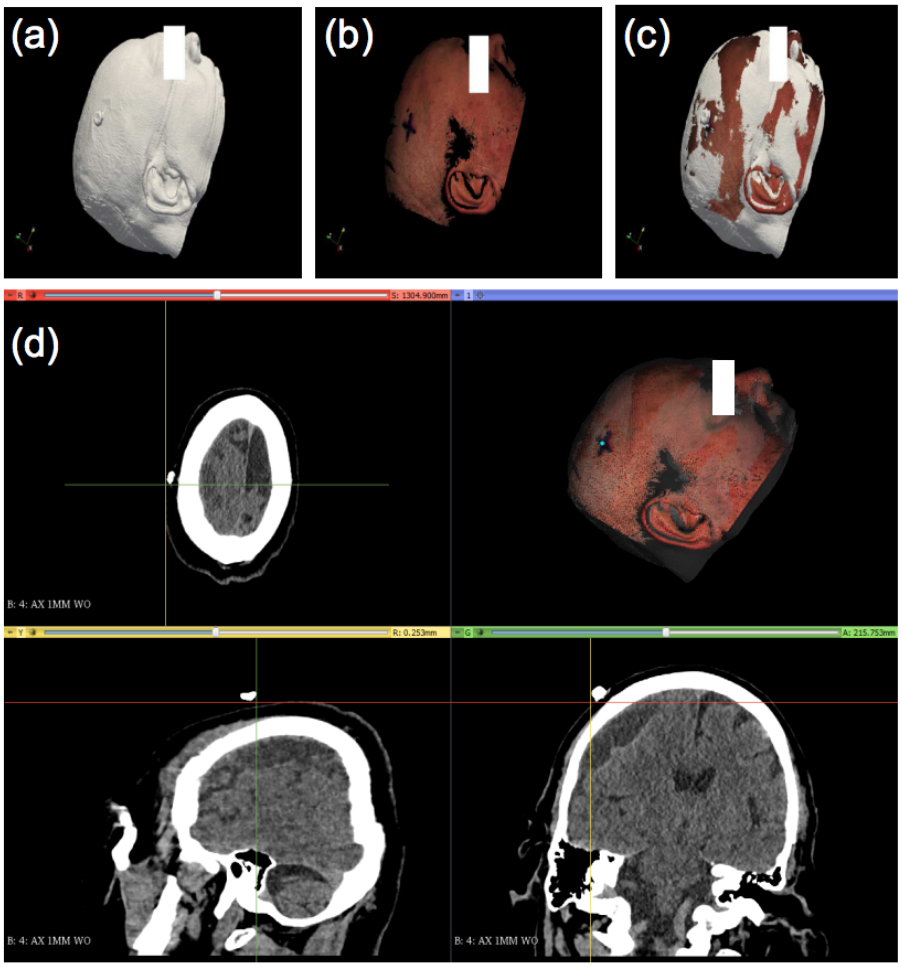

Figure 7.4: Evaluation of the 3D navigation system involving a patient with a CSDH who underwent SEPS placement. (a) 3-dimensional reconstruction of the patient's head from a pre-procedure CT scan. For this particular patient, a fiducial consisting of a metal hex nut was taped on the patient's head for the pre-procedure localizing CT scan. The initial CT scan obtained on patient presentation had too much movement and could not be used either for surgical procedure planning or for this project. The patient's eyes have been obscured for anonymity. (b) A color 3-dimensional scan of the patient's head with an "X" marking the proposed burr hole location. The proposed location is posterior and lateral to the hex nut's location, due to the recognition that the hex nut's location is too anterior and superior. (c) Registration between the CT scan and the visible light-based 3D scan of the patient. Beige areas are where the 3D scan surface is closer to the observer, and white areas are where the CT scan is closer to the observer. As expected, the "X" mark is posterior and lateral to the fiducial. (d) Navigation panel generated by the system. All views are aligned at the center of the "X" mark. The top left is the axial view of the patient's CT scan, top right is the alignment between the 3D scan and the CT scan, bottom left is the sagittal view, and bottom right is the coronal view. Cross hairs indicate the center of the ink "X" mark on the 3D scan. All of the panels are scrollable.

Chapter VIII

CONCLUSIONS & FUTURE WORK

8.1 Conclusions

In this thesis, a complete solution for quantitatively measure the cortical brain surface displacement through stereo pair reconstructions without conventional tracking technology has been proposed. This starts with a noval 'trackerless' surgical image-guided system to plan and execute craniotomy for neurosurgery. Surgeons can plan the craniotomy contour without the presence of the physical patient, and without the assistance of optical tracking system. After the dura septa is open and cortical surface is exposed, the surgical operating microscope can provide consistent brain surgery video, which is the intra-operative data source. This work shows that using stereo-pair reconstruction can provide accurate intra-operative tissue surface. Different from laser range scanner, stereo microscope is surgical procedure friendly, which means it will not interrupt the workflow. Also, the microscope itself can be tracked by attaching an optical tracking star on, then the scope can move freely and the reconstructed point clouds can be registered to the same space. The displacement of vessel feature points can be calculated before and after shift occurs since they are in the same space. This registration process can also be implemented without conventional tracking system. Instead of tracking the microscope, it is also feasible to attach rigid landmarks on the rigid bone around the craniotomy. These rigid landmarks do not move when shift occurs, so they can be used to register the pre- and post cortical surface geometries together. For comparison purpose, the designation of vessel features displacement is used as ground truth values.

In manuscript I, a novel craniotomy and cortical deformation simulation system that generates realistic soft tissue displacements has been built. The device allows for measurements and comparisons between stereo-pair reconstructions and commercial tracking sys-

tems. The device can simulate known behaviors within the operating room theatre (namely lateral shift and sag). The different inserts designed allow for variable craniotomy size analysis that range from 3 to 7 cm. The comparison results indicate that the use of stereo-pair images captured from stereo cameras has the potential to gather valid intra-operative information without disrupting the surgery. This is the prerequisite for us to compensate brain shift using stereo-pair reconstruction fully-automatically in the OR. While several groups are pursuing microscope driven stereo-pair cortical shift estimation, there is still a paucity of validation with respect to independent tracking method comparisons under controlled conditions. To our knowledge, the construction of a device like this is completely novel. To sum up, the purpose of this work was to evaluate the stereo-pair reconstruction fidelity as well as the manually-designated brain shift tracking with stereo pair. Results we have obtained suggest that the deformation computed from 3D cortical vessel surface similar to the deformation measured with the ground truth tracking system.

In manuscript II, a GUI-based system that integrates all necessary functionality for reconstructing FOV of stereo-pair or microscope cameras has been developed, and it includes (1) capturing stereo-pair images or video streams, (2) extracting checkerboard corners, (3) calibrating stereo cameras, (4) computing disparity, and (5) displaying point clouds. Moreover, the parameters associated with the disparity computation can be modified in an interactive GUI to improve the results. This reconstruction system is functional, user-friendly, and it requires only minimal prior knowledge. By applying image-to-physical space registration, the stereoscopic microscope can be tracked, and freely moved without disrupting the surgical procedure. The reconstruction accuracy and displacement comparison results suggest that this system could be used to gather cortical data to measure and compensate for brain shift during image-guided surgery. This extends the capability of conventional navigation system.

In manuscript III, the feasibility of using a 'trackerless' surgical image-guided system to plan and execute a craniotomy for neurosurgery has been demonstrated. Overall, the virtual

craniotomy plan provided by the approach was consistent with the conventional one. The interactive extension of 3D Slicer shown here can simplify the procedure of pre-operative planning by removing the need for conventional tracking and provide a reliable craniotomy contour. The work herein when combined with the cortical surface registration, cortical deformation measurement methods, and finally computational brain shift prediction framework is a powerful paradigm that could potentially eliminate the need for conventional tracking technology and usher in integrated more nimble vision-based guidance systems for neurosurgery.

Currently, the proposed framework has been tested well on the phantom experiments (in some experiments, the real clinical data is integrated into the head phantom). A fully realized system is supposed to work well on the real clinical case. It has the potential to provide the instrumentation aspect for a noninvasive soft tissue correction platform and quantify brain shift at the cortical surface. This trackerless system definitely brings benefits to both patients, neurosurgeons, and image-guided surgery field. Firstly, the craniotomy planning procedures are not necessary to be performed in the operating room, they can be performed in the surgeon's office, not even needing the partitication of the patient. This gives the surgeons a lot of flexibility when preparing for the surgery. Secondly, the use of the microscope as the intra-operative data source does not interrupt the surgical workflow since surgical the microscope is normally used in the tumor resection surgery. Thirdly, the concept of removing the conventional tracking system is a big save for the operating room, both on financial budget and room space saving. The most crucial part is that it compensates the cortical surface movement which the current commercial surgical navigation systems cannot achieve.

8.2 Future Work

The proposed framework is tested well mainly on phantom setup (although some experiments integrate the real clinical MR image into the head phantom). The next step is to test

it in a real clinical case, the steps are almost exactly the same as the phantom setup. The validation process is still the same too, comparing with the designation of vessel feature points using a conventional tracking system.

Also, as stated before, the requirement of fixed microscope settings is another direction of the future work. The microscope needs to be adjusted to the previous calibrated settings (focal length and zoom factor) in order to reconstruct the cortical surface. The only way to get the reconstruction under a new set of focal length and zoom factor is to re-calibrate the microscope in that settings. There are different things that worth investigating. First, try to rewrite the scaling python code to C++ from one of the previous graduate students in the lab. He has proposed a way to estimate the magnification factor of the microscope, so that the reconstructed point cloud can be scaled to its correct size [81]. Second, look for other groups that are trying to solve this problem, for example, Ji et al. [140] proposed an efficient method for sustaining a quantitative image-to-physical space relationship for arbitrary image acquisition settings without the need for camera re-calibration. Last but not least, seek collaboration with the manufacturing company, for example, the microscope provider, Zeiss Corp (Oberkochen, Germany), to see whether they have solutions that can provide a full range of calibration so that the cortical surface point cloud can be reconstructed under any setting. The validation is to use some geometry-known phantom (like a stair phantom in previous experiments).

Another aspect of the future work is to investigate the possibility to continue improving the accuracy of reconstruction. Current reconstruction method is based on classic stereo-vision techniques, and the accuracy is acceptable. Nowadays, deep learning techniques have developed rapidly and more researchers are trying to solve traditional computer vision problems using machine learning methods. The stereo-vision reconstruction accuracy highly depends on the quality of stereo matching. This is a classic computer vision problem, but recently researchers are investigating in applying deep learning for estimating the disparity [141, 142]. The geometry-known phantom can be used to evaluate the reconstruc-

tion accuracy.

If all of the above are fully realized, the further way to impact more is to take advantage of the consistent inra-operative surface data from surgical microscope. Near real-time image correction is possible. After the image-to-physical registration is performed, the microscope reconstructs the cortical surface every predetermined period of time. For every two adjacent cortical surface point cloud and register them to the same space, run automatic feature detection algorithm (like SIFT) to find several corresponding points, the displacement vectors of these feature points can be used to run the model correction. By doing this, the pre-operative image can be updated every predetermined period of time. To validate it in near real-time might be difficult since the ground-truth shift is hard to acquire in a short time. But it can be validated in pre- and post states if there is enough time to acquire the feature points position from a conventional tracking system.

BIBLIOGRAPHY

[1] Rebecca L Siegel, Kimberly D Miller, and Ahmedin Jemal. Cancer statistics, 2017. *CA: a cancer journal for clinicians*, 67(1):7–30, 2017.

[2] American Brain Tumor Association et al. Brain tumor statistics. *Available at:. Accessed May*, 2, 2016.

[3] Mauricio Castillo. History and evolution of brain tumor imaging: insights through radiology. *Radiology*, 273(2S):S111–S125, 2014.

[4] Robert L Galloway Jr. The process and development of image-guided procedures. *Annual Review of Biomedical Engineering*, 3(1):83–108, 2001.

[5] LD Lunsford, Richard E Latchaw, and JK Vries. Stereotactic implantation of deep brain electrodes using computed tomography. *Neurosurgery*, 13(3):280–286, 1983.

[6] Philippe Menei, Jean-Pierre Benoit, Michelle Boisdron-Celle, Dominique Fournier, Philippe Mercier, and Gilles Guy. Drug targeting into the central nervous system by stereotactic implantation of biodegradable microspheres. *Neurosurgery*, 34(6):1058–1064, 1994.

[7] Ft Mundinger and Th Hoefer. Protracted long-term irradiation of inoperable midbrain tumours by stereotactic curie-therapy using iridium-192. In *Advances in Stereotactic and Functional Neurosurgery*, pages 93–100. Springer, 1974.

[8] David M Yurek and John R Sladek Jr. Dopamine cell replacement: Parkinson's disease. *Annual review of neuroscience*, 13(1):415–440, 1990.

[9] T Takizawa, Sh Soto, A Sanou, and Y Murakami. Frameless isocentric stereotactic laser beam guide for image-directed microsurgery. *Acta neurochirurgica*, 125(1-4):177–180, 1993.

[10] T Brommeland and R Hennig. A new procedure for frameless computer navigated stereotaxy. *Acta neurochirurgica*, 142(4):443–448, 2000.

[11] Yukio Kosugi, E Watanabe, J Goto, T Watanabe, S Yoshimoto, K Takakura, and J Ikebe. An articulated neurosurgical navigation system using mri and ct images. *IEEE Transactions on Biomedical Engineering*, 35(2):147–152, 1988.

[12] P. Spectra. Polaris Optical Tracking System. http://www.ndigital.com/medical/products/%0Apolaris-family/. (Accessed: September 2017).

[13] Brainlab AG, Munich Germany. https://www.brainlab.com/en/surgery-products/overview-neurosurgery-products/cranial-navigation/. (Accessed: 2018).

[14] Medtronics Stealth Station Surgical Navigation System. https://www.medtronic.com/us-en/healthcare-professionals/products/neurological/surgical-navigation-systems/stealthstation/cranial-neurosurgery-navigation.html. (Accessed: 2018).

[15] Patrick J Kelly, Bruce A Kall, Stephan Goerss, and Franklin Earnest. Computer-assisted stereotaxic laser resection of intra-axial brain neoplasms. *Journal of neurosurgery*, 64(3):427–439, 1986.

[16] John Koivukangas, Yrjö Louhisalmi, Jyrki Alakuijala, and Jarkko Oikarinen. Ultrasound-controlled neuronavigator-guided brain surgery. *Journal of neurosurgery*, 79(1):36–42, 1993.

[17] Martin J Ryan, Robert K Erickson, David N Levin, Charles A Pelizzari, R Loch Macdonald, and George J Dohrmann. Frameless stereotaxy with real-time tracking of patient head movement and retrospective patientimage registration. *Journal of neurosurgery*, 85(2):287–292, 1996.

[18] Derek LG Hill, Calvin R Maurer, Robert J Maciunas, Robert J Maciunas, John A Barwise, J Michael Fitzpatrick, and Matthew Y Wang. Measurement of intraoperative brain surface deformation under a craniotomy. *Neurosurgery*, 43(3):514–526, 1998.

[19] Arya Nabavi, Peter McL. Black, David T Gering, Carl-Fredrik Westin, Vivek Mehta, Richard S Pergolizzi Jr, Mathieu Ferrant, Simon K Warfield, Nobuhiko Hata, Richard B Schwartz, et al. Serial intraoperative magnetic resonance imaging of brain shift. *Neurosurgery*, 48(4):787–798, 2001.

[20] Ian J Gerard, Marta Kersten-Oertel, Kevin Petrecca, Denis Sirhan, Jeffery A Hall, and D Louis Collins. Brain shift in neuronavigation of brain tumors: A review. *Medical image analysis*, 35:403–420, 2017.

[21] Siming Bayer, Andreas Maier, Martin Ostermeier, and Rebecca Fahrig. Intraoperative imaging modalities and compensation for brain shift in tumor resection surgery. *International journal of biomedical imaging*, 2017, 2017.

[22] Michael I Miga. Computational modeling for enhancing soft tissue image guided surgery: an application in neurosurgery. *Annals of biomedical engineering*, 44(1):128–138, 2016.

[23] Simon K Warfield, Steven J Haker, Ion-Florin Talos, Corey A Kemper, Neil Weisenfeld, Andrea UJ Mewes, Daniel Goldberg-Zimring, Kelly H Zou, Carl-Fredrik Westin, William M Wells, et al. Capturing intraoperative deformations: research experience at brigham and womens hospital. *Medical image analysis*, 9(2):145–162, 2005.

[24] Christine DeLorenzo, Xenophon Papademetris, Lawrence H Staib, Kenneth P Vives, Dennis D Spencer, and James S Duncan. Nonrigid intraoperative cortical surface

tracking using game theory. In *2007 IEEE 11th International Conference on Computer Vision*, pages 1–8. IEEE, 2007.

[25] Grand Roman Joldes, Adam Wittek, Mathieu Couton, Simon K Warfield, and Karol Miller. Real-time prediction of brain shift using nonlinear finite element algorithms. In *International Conference on Medical Image Computing and Computer-Assisted Intervention*, pages 300–307. Springer, 2009.

[26] Thomas Hartkens, Derek LG Hill, Andy D Castellano-Smith, David J Hawkes, CR Maurer, Alastair J Martin, Walter A Hall, Haiying Liu, and Charles L Truwit. Measurement and analysis of brain deformation during neurosurgery. *IEEE transactions on medical imaging*, 22(1):82–92, 2003.

[27] Christopher Nimsky, Oliver Ganslandt, Simon Cerny, Peter Hastreiter, Günther Greiner, and Rudolf Fahlbusch. Quantification of, visualization of, and compensation for brain shift using intraoperative magnetic resonance imaging. *Neurosurgery*, 47(5):1070–1080, 2000.

[28] C Rainer Wirtz, Mario M Bonsanto, Michael Knauth, Volker M Tronnier, Fritz K Albert, Andreas Staubert, and Stefan Kunze. Intraoperative magnetic resonance imaging to update interactive navigation in neurosurgery: method and preliminary experience. *Computer Aided Surgery*, 2(3-4):172–179, 1997.

[29] Ferenc A Jolesz, Arya Nabavi, and Ron Kikinis. Integration of interventional mri with computer-assisted surgery. *Journal of Magnetic Resonance Imaging*, 13(1):69–77, 2001.

[30] Lara M Vigneron, Ludovic Noels, Simon K Warfield, Jacques G Verly, and Pierre A Robe. Serial fem/xfem-based update of preoperative brain images using intraoperative mri. *Journal of Biomedical Imaging*, 2012:2, 2012.

[31] Neculai Archip, Olivier Clatz, Stephen Whalen, Dan Kacher, Andriy Fedorov, Andriy Kot, Nikos Chrisochoides, Ferenc Jolesz, Alexandra Golby, Peter M Black, et al. Non-rigid alignment of pre-operative mri, fmri, and dt-mri with intra-operative mri for enhanced visualization and navigation in image-guided neurosurgery. *Neuroimage*, 35(2):609–624, 2007.

[32] Jin-Song Wu, Xiu Gong, Yan-Yan Song, Dong-Xiao Zhuang, Cheng-Jun Yao, Tian-Ming Qiu, Jun-Feng Lu, Jie Zhang, Wei Zhu, Ying Mao, et al. 3.0-t intraoperative magnetic resonance imaging-guided resection in cerebral glioma surgery: interim analysis of a prospective, randomized, triple-blind, parallel-controlled trial. *Neurosurgery*, 61(CN_suppl_1):145–154, 2014.

[33] Olutayo Ibukunolu Olubiyi, Aysegul Ozdemir, Fatih Incekara, Yanmei Tie, Parviz Dolati, Liangge Hsu, Sandro Santagata, Zhenrui Chen, Laura Rigolo, and Alexandra J Golby. Intraoperative magnetic resonance imaging in intracranial glioma resection: a single-center, retrospective blinded volumetric study. *World neurosurgery*, 84(2):528–536, 2015.

[34] Christian Senft, Andrea Bink, Kea Franz, Hartmut Vatter, Thomas Gasser, and Volker Seifert. Intraoperative mri guidance and extent of resection in glioma surgery: a randomised, controlled trial. *The lancet oncology*, 12(11):997–1003, 2011.

[35] David J Engle and L Dade Lunsford. Brain tumor resection guided by intraoperative computed tomography. *Journal of neuro-oncology*, 4(4):361–370, 1987.

[36] Thorsteinn Gunnarsson, Annette Theodorsson, Per Karlsson, Steen Fridriksson, Sverre Boström, Jan Persliden, Ingegerd Johansson, and Jan Hillman. Mobile computerized tomography scanning in the neurosurgery intensive care unit: increase in patient safety and reduction of staff workload. *Journal of neurosurgery*, 93(3):432–436, 2000.

[37] MJ Daly, JH Siewerdsen, DJ Moseley, DA Jaffray, and JC Irish. Intraoperative cone-beam ct for guidance of head and neck surgery: Assessment of dose and image quality using a c-arm prototype. *Medical physics*, 33(10):3767–3780, 2006.

[38] Robert C Orth, Michael J Wallace, Michael D Kuo, Technology Assessment Committee of the Society of Interventional Radiology, et al. C-arm cone-beam ct: general principles and technical considerations for use in interventional radiology. *Journal of Vascular and Interventional Radiology*, 19(6):814–820, 2008.

[39] Alexandra Lauric, Robert S Heller, Sarah Schimansky, and Adel M Malek. Benefit of cone-beam ct angiography in visualizing aneurysm shape and identification of exact rupture site. *Journal of Neuroimaging*, 25(1):56–61, 2015.

[40] Vitor Mendes Pereira, Iris Smit-Ockeloen, Olivier Brina, Drazenko Babic, Marcel Breeuwer, Karl Schaller, Karl-Olof Lovblad, and Daniel Ruijters. Volumetric measurements of brain shift using intraoperative cone-beam computed tomography: preliminary study. *Operative Neurosurgery*, 12(1):4–13, 2015.

[41] N Nakao, K Nakai, and T Itakura. Updating of neuronavigation based on images intraoperatively acquired with a mobile computerized tomographic scanner. *min-Minimally Invasive Neurosurgery*, 46(02):117–120, 2003.

[42] Richard D Bucholz, David D Yeh, Jason Trobaugh, Leslie L McDurmont, Christopher D Sturm, Carol Baumann, Jaimie M Henderson, Ari Levy, and Paul Kessman. The correction of stereotactic inaccuracy caused by brain shift using an intraoperative ultrasound device. In *CVRMed-MRCAS'97*, pages 459–466. Springer, 1997.

[43] Geirmund Unsgaard, Steinar Ommedal, Tomm Muller, Aage Gronningsaeter, and Toril A Nagelhus Hernes. Neuronavigation by intraoperative three-dimensional ultrasound: initial experience during brain tumor resection. *Neurosurgery*, 50(4):804–812, 2002.

[44] Marloes Maria Johanna Letteboer, Peter WA Willems, Max A Viergever, and Wiro J Niessen. Brain shift estimation in image-guided neurosurgery using 3-d ultrasound. *IEEE Transactions on Biomedical Engineering*, 52(2):268–276, 2005.

[45] G Unsgaard, OM Rygh, T Selbekk, TB Müller, F Kolstad, F Lindseth, and TA Nagelhus Hernes. Intra-operative 3d ultrasound in neurosurgery. *Acta neurochirurgica*, 148(3):235–253, 2006.

[46] Rahul Sastry, Wenya Linda Bi, Steve Pieper, Sarah Frisken, Tina Kapur, William Wells III, and Alexandra J Golby. Applications of ultrasound in the resection of brain tumors. *Journal of Neuroimaging*, 27(1):5–15, 2017.

[47] Andrej Šteňo, Vladimír Hollỳ, Peter Mendel, Veronika Šteňová, L'ubica Petričková, Gabriela Timárová, Michaela Jezberová, Vít'azoslav Belan, Boris Rychlỳ, Jozef Šurkala, et al. Navigated 3d–ultrasound versus conventional neuronavigation during awake resections of eloquent low-grade gliomas: a comparative study at a single institution. *Acta neurochirurgica*, 160(2):331–342, 2018.

[48] F Prada, M Del Bene, L Mattei, L Lodigiani, S DeBeni, V Kolev, I Vetrano, L Solbiati, G Sakas, and F DiMeco. Preoperative magnetic resonance and intraoperative ultrasound fusion imaging for real-time neuronavigation in brain tumor surgery. *Ultraschall in der Medizin-European Journal of Ultrasound*, 36(02):174–186, 2015.

[49] Christian Askeland, Ole Vegard Solberg, Janne Beate Lervik Bakeng, Ingerid Reinertsen, Geir Arne Tangen, Erlend Fagertun Hofstad, Daniel Høyer Iversen, Cecilie Våpenstad, Tormod Selbekk, Thomas Langø, et al. Custusx: an open-source research platform for image-guided therapy. *International journal of computer assisted radiology and surgery*, 11(4):505–519, 2016.

[50] Frederik Maes, Dirk Vandermeulen, and Paul Suetens. Medical image registration using mutual information. *Proceedings of the IEEE*, 91(10):1699–1722, 2003.

[51] Michael I Miga, Keith D Paulsen, John M Lemery, Symma D Eisner, Alexander Hartov, Francis E Kennedy, and David W Roberts. Model-updated image guidance: initial clinical experiences with gravity-induced brain deformation. *IEEE transactions on medical imaging*, 18(10):866–874, 1999.

[52] Keith D Paulsen, Michael I Miga, Francis E Kennedy, PJ Hoopens, Alex Hartov, and David W Roberts. A computational model for tracking subsurface tissue deformation during stereotactic neurosurgery. *IEEE Transactions on Biomedical Engineering*, 46(2):213–225, 1999.

[53] Michael I Miga, Keith D Paulsen, Francis E Kennedy, P Jack Hoopes, Alex Hartov, and David W Roberts. A 3d brain deformation model experiencing comparable surgical loads. In *Proceedings of the 19th Annual International Conference of the IEEE Engineering in Medicine and Biology Society.'Magnificent Milestones and Emerging Opportunities in Medical Engineering'(Cat. No. 97CH36136)*, volume 2, pages 773–776. IEEE, 1997.

[54] Michael I Miga, David W Roberts, Francis E Kennedy, Leah A Platenik, Alex Hartov, Karen E Lunn, and Keith D Paulsen. Modeling of retraction and resection for intraoperative updating of images. *Neurosurgery*, 49(1):75–85, 2001.

[55] Michael I Miga. *Development and quantification of a 3D brain deformation model for model-updated image-guided stereotactic neurosurgery*. PhD thesis, Dartmouth College, 1998.

[56] David W Roberts, Michael I Miga, Alexander Hartov, Symma Eisner, John M Lemery, Francis E Kennedy, and Keith D Paulsen. Intraoperatively updated neuroimaging using brain modeling and sparse data. *Neurosurgery*, 45(5):1199–1207, 1999.

[57] Prashanth Dumpuri, Chun-Cheng R Chen, and Michael I Miga. Model-updated

image guidance: a statistical approach to gravity-induced brain shift. In *International Conference on Medical Image Computing and Computer-Assisted Intervention*, pages 375–382. Springer, 2003.

[58] Prashanth Dumpuri, Reid C Thompson, Benoit M Dawant, Aize Cao, and Michael I Miga. An atlas-based method to compensate for brain shift: Preliminary results. *Medical Image Analysis*, 11(2):128–145, 2007.

[59] Ishita Chen, Aaron M Coffey, Siyi Ding, Prashanth Dumpuri, Benoit M Dawant, Reid C Thompson, and Michael I Miga. Intraoperative brain shift compensation: accounting for dural septa. *IEEE Transactions on Biomedical Engineering*, 58(3):499–508, 2011.

[60] Ishita Chen, Rowena E Ong, Amber L Simpson, Kay Sun, Reid C Thompson, and Michael I Miga. Integrating retraction modeling into an atlas-based framework for brain shift prediction. *IEEE Transactions on Biomedical Engineering*, 60(12):3494–3504, 2013.

[61] Kay Sun, Thomas S Pheiffer, Amber L Simpson, Jared A Weis, Reid C Thompson, and Michael I Miga. Near real-time computer assisted surgery for brain shift correction using biomechanical models. *IEEE journal of translational engineering in health and medicine*, 2:1–13, 2014.

[62] Michael I Miga, Kay Sun, Ishita Chen, Logan W Clements, Thomas S Pheiffer, Amber L Simpson, and Reid C Thompson. Clinical evaluation of a model-updated image-guidance approach to brain shift compensation: experience in 16 cases. *International journal of computer assisted radiology and surgery*, 11(8):1467–1474, 2016.

[63] Michael I Miga, Tuhin K Sinha, David M Cash, Robert L Galloway, and Robert J

Weil. Cortical surface registration for image-guided neurosurgery using laser-range scanning. *IEEE Transactions on medical Imaging*, 22(8):973–985, 2003.

[64] David M Cash, Tuhin K Sinha, William C Chapman, Hiromi Terawaki, Benoit M Dawant, Robert L Galloway, and Michael I Miga. Incorporation of a laser range scanner into image-guided liver surgery: surface acquisition, registration, and tracking. *Medical Physics*, 30(7):1671–1682, 2003.

[65] Tuhin K Sinha, Michael I Miga, David M Cash, and Robert J Weil. Intraoperative cortical surface characterization using laser range scanning: Preliminary results. *Operative Neurosurgery*, 59(suppl_4):ONS–368, 2006.

[66] Tuhin K Sinha, Benoit M Dawant, Valerie Duay, David M Cash, Robert J Weil, Reid Carleton Thompson, Kyle D Weaver, and Michael I Miga. A method to track cortical surface deformations using a laser range scanner. *IEEE transactions on medical imaging*, 24(6):767–781, 2005.

[67] Aize Cao, RC Thompson, P& al Dumpuri, BM Dawant, RL Galloway, S Ding, and MI Miga. Laser range scanning for image-guided neurosurgery: Investigation of image-to-physical space registrations. *Medical physics*, 35(4):1593–1605, 2008.

[68] Aize Cao, Michael I Miga, Prashanth Dumpuri, Siyi Ding, Benoit M Dawant, and Reid Carleton Thompson. Target error for image-to-physical space registration: Preliminary clinical results using laser range scanning. In *Medical Imaging 2007: Visualization and Image-Guided Procedures*, volume 6509, page 65091D. International Society for Optics and Photonics, 2007.

[69] Siyi Ding, Michael I Miga, Jack H Noble, Aize Cao, Prashanth Dumpuri, Reid C Thompson, and Benoit M Dawant. Semiautomatic registration of pre-and postbrain tumor resection laser range data: method and validation. *IEEE Transactions on Biomedical Engineering*, 56(3):770–780, 2009.

[70] Thomas S Pheiffer, Amber L Simpson, Brian Lennon, Reid C Thompson, and Michael I Miga. Design and evaluation of an optically-tracked single-ccd laser range scanner. *Medical physics*, 39(2):636–642, 2012.

[71] Oskar Škrinjar, Colin Studholme, Arya Nabavi, and James Duncan. Steps toward a stereo-camera-guided biomechanical model for brain shift compensation. In *Biennial International Conference on Information Processing in Medical Imaging*, pages 183–189. Springer, 2001.

[72] Oskar Skrinjar, Hemant Tagare, and James Duncan. Surface growing from stereo images. In *Proceedings IEEE Conference on Computer Vision and Pattern Recognition. CVPR 2000 (Cat. No. PR00662)*, volume 2, pages 571–576. IEEE, 2000.

[73] Hai Sun, Hany Farid, Alex Hartov, Karen E Lunn, David W Roberts, and Keith D Paulsen. Real-time correction scheme for calibration and implementation of microscope-based image-guided neurosurgery. In *Medical Imaging 2002: Visualization, Image-Guided Procedures, and Display*, volume 4681, pages 47–55. International Society for Optics and Photonics, 2002.

[74] Hai Sun, Hany Farid, Kyle Rick, Alex Hartov, David W Roberts, and Keith D Paulsen. Estimating cortical surface motion using stereopsis for brain deformation models. In *International Conference on Medical Image Computing and Computer-Assisted Intervention*, pages 794–801. Springer, 2003.

[75] Hai Sun, David W Roberts, Hany Farid, Ziji Wu, Alex Hartov, and Keith D Paulsen. Cortical surface tracking using a stereoscopic operating microscope. *Operative Neurosurgery*, 56(suppl_1):ONS–86, 2005.

[76] Perrine Paul, Xavier Morandi, and Pierre Jannin. A surface registration method for quantification of intraoperative brain deformations in image-guided neurosurgery.

IEEE Transactions on Information Technology in Biomedicine, 13(6):976–983, 2009.

[77] Siyi Ding, Michael I Miga, Thomas S Pheiffer, Amber L Simpson, Reid C Thompson, and Benoit M Dawant. Tracking of vessels in intra-operative microscope video sequences for cortical displacement estimation. *IEEE Transactions on Biomedical Engineering*, 58(7):1985–1993, 2011.

[78] Songbai Ji, Xiaoyao Fan, David W Roberts, and Keith D Paulsen. Cortical surface strain estimation using stereovision. In *International Conference on Medical Image Computing and Computer-Assisted Intervention*, pages 412–419. Springer, 2011.

[79] Songbai Ji, Xiaoyao Fan, David W Roberts, Alex Hartov, and Keith D Paulsen. Cortical surface shift estimation using stereovision and optical flow motion tracking via projection image registration. *Medical image analysis*, 18(7):1169–1183, 2014.

[80] Ankur N Kumar, Thomas S Pheiffer, Amber L Simpson, Reid C Thompson, Michael I Miga, and Benoit M Dawant. Phantom-based comparison of the accuracy of point clouds extracted from stereo cameras and laser range scanner. In *Medical Imaging 2013: Image-Guided Procedures, Robotic Interventions, and Modeling*, volume 8671, page 867125. International Society for Optics and Photonics, 2013.

[81] Ankur N Kumar, Michael I Miga, Thomas S Pheiffer, Lola B Chambless, Reid C Thompson, and Benoit M Dawant. Persistent and automatic intraoperative 3d digitization of surfaces under dynamic magnifications of an operating microscope. *Medical image analysis*, 19(1):30–45, 2015.

[82] Xiaochen Yang, Logan W Clements, Ma Luo, Saramati Narasimhan, Reid C Thompson, Benoit M Dawant, and Michael I Miga. Stereovision-based integrated system for point cloud reconstruction and simulated brain shift validation. *Journal of Medical Imaging*, 4(3):035002, 2017.

[83] Olivier Clatz, Hervé Delingette, I-F Talos, Alexandra J Golby, Ron Kikinis, Ferenc A Jolesz, Nicholas Ayache, and Simon K Warfield. Robust nonrigid registration to capture brain shift from intraoperative mri. *IEEE transactions on medical imaging*, 24(11):1417–1427, 2005.

[84] Siyi Ding, Michael I Miga, Reid C Thompson, Prashanth Dumpuri, Aize Cao, and Benoit M Dawant. Estimation of intra-operative brain shift using a tracked laser range scanner. In *2007 29th Annual International Conference of the IEEE Engineering in Medicine and Biology Society*, pages 848–851. IEEE, 2007.

[85] David W Roberts, Alexander Hartov, Francis E Kennedy, Michael I Miga, and Keith D Paulsen. Intraoperative brain shift and deformation: a quantitative analysis of cortical displacement in 28 cases. *Neurosurgery*, 43(4):749–758, 1998.

[86] Tuhin K Sinha, Valerie Duay, Benoit M Dawant, and Michael I Miga. Cortical shift tracking using a laser range scanner and deformable registration methods. In *International Conference on Medical Image Computing and Computer-Assisted Intervention*, pages 166–174. Springer, 2003.

[87] Jay B West and Calvin R Maurer. Designing optically tracked instruments for image-guided surgery. *IEEE transactions on medical imaging*, 23(5):533–545, 2004.

[88] Zhengyou Zhang. A flexible new technique for camera calibration. *IEEE Transactions on pattern analysis and machine intelligence*, 22, 2000.

[89] X. Yang. Stereo-pair capture software. https://my.vanderbilt.edu/xiaochen/archives/75. (Accessed: September 2017).

[90] Richard Hartley and Andrew Zisserman. *Multiple view geometry in computer vision*. Cambridge university press, 2003.

[91] Richard I Hartley. Theory and practice of projective rectification. *International Journal of Computer Vision*, 35(2):115–127, 1999.

[92] Jean-Yves Bouguet et al. *Visual methods for three-dimensional modeling*. Citeseer, 1999.

[93] J. Y. Bouguet. Camera calibration toolbox for matlab. http://www.vision.caltech.edu/bouguetj/calib_doc/. (Accessed: September 2017).

[94] Roger Tsai. A versatile camera calibration technique for high-accuracy 3d machine vision metrology using off-the-shelf tv cameras and lenses. *IEEE Journal on Robotics and Automation*, 3(4):323–344, 1987.

[95] Daniel Scharstein and Richard Szeliski. A taxonomy and evaluation of dense two-frame stereo correspondence algorithms. *International journal of computer vision*, 47(1-3):7–42, 2002.

[96] Gary Bradski and Adrian Kaehler. *Learning OpenCV: Computer vision with the OpenCV library*. " O'Reilly Media, Inc.", 2008.

[97] Xiaochen Yang, Logan W Clements, Rebekah H Conley, Reid C Thompson, Benoit M Dawant, and Michael I Miga. A novel craniotomy simulation system for evaluation of stereo-pair reconstruction fidelity and tracking. In *Proc. of SPIE Vol*, volume 9786, pages 978612–1, 2016.

[98] Xiaochen Yang. Stereo-pair Capture Software. Vanderbilt.edu https://my.vanderbilt.edu/xiaochen/archives/75. (Accessed: August 2015).

[99] Kurt Konolige. Small vision systems: Hardware and implementation. In *Robotics research*, pages 203–212. Springer, 1998.

[100] Heiko Hirschmuller. Stereo processing by semiglobal matching and mutual information. *IEEE Transactions on pattern analysis and machine intelligence*, 30(2):328–341, 2008.

[101] D. Scharstein and R. Szeliski. Middlebury Stereo Evaluation - Version 3. http://vision.middlebury.edu/stereo/eval3/. (Accessed: April 2017).

[102] OpenCV. Disparity Map Post-filtering. http://docs.opencv.org/trunk/d3/d14/tutorial_ximgproc_disparity_filtering.html. (Accessed: April 2017).

[103] Qt. Qt Powerful, Interactive and Corss-Platform Applications. https://www.qt.io/. (Accessed: August 2017).

[104] Point Cloud Library. http://www.pointclouds.org/. (Accessed: July 2016).

[105] Polaris Spectra. Polaris Optical Tracking System. http://www.ndigital.com/medical/products/polaris-family/. (Accessed: July 2016).

[106] Michael Fitzpatrick. Algorithms for Registration, Error Prediction, and Rotation Parameter Conversion in Matlab. http://eecs.vanderbilt.edu/people/mikefitzpatrick/computer%20programs/computer_algorithms_in_Matlab.htm. (Accessed: July 2016).

[107] Xiaochen Yang, Logan W Clements, Ma Luo, Saramati Narasimhan, Reid C Thompson, Benoit M Dawant, and Michael I Miga. Integrated system for point cloud reconstruction and simulated brain shift validation using tracked surgical microscope. In *SPIE Medical Imaging*, pages 101352G–101352G. International Society for Optics and Photonics, 2017.

[108] Xiaochen Yang. Stereovision-based Integrated System for Point Cloud Reconstruction. Vanderbilt.edu https://my.vanderbilt.edu/xiaochen/archives/351. (Accessed: January 2019).

[109] 3D Slicer. A multi-platform, free and open source software package for visualization and medical image computing. https://www.slicer.org/. (Accessed: August 2017).

[110] VTK. The Visualization Toolkit. http://www.vtk.org. (Accessed: August 2017).

[111] ITK. National Library of Medicine Insight Segmentation and Registration Toolkit. http://www.itk.org. (Accessed: August 2017).

[112] Xiaochen Yang. Trackerless Craniotomy Planning based on 3D Slicer. Vanderbilt.edu https://my.vanderbilt.edu/xiaochen/archives/355. (Accessed: January 2019).

[113] Carlos Faria, Ofri Sadowsky, Estela Bicho, Giancarlo Ferrigno, Leo Joskowicz, Moshe Shoham, Refael Vivanti, and Elena De Momi. Validation of a stereo camera system to quantify brain deformation due to breathing and pulsatility. *Medical physics*, 41(11), 2014.

[114] Brandon Chan, Jason Auyeung, John F Rudan, Randy E Ellis, and Manuela Kunz. Intraoperative application of hand-held structured light scanning: a feasibility study. *International journal of computer assisted radiology and surgery*, 11(6):1101–1108, 2016.

[115] Tamas Ungi, Andras Lasso, and Gabor Fichtinger. Open-source platforms for navigated image-guided interventions, 2016.

[116] Slicer OpenIGTLink. OpenIGTLink interface module for 3D Slicer. https://github.com/openigtlink/OpenIGTLinkIF. (Accessed: August 2017).

[117] Andras Lasso, Tamas Heffter, Adam Rankin, Csaba Pinter, Tamas Ungi, and Gabor Fichtinger. Plus: open-source toolkit for ultrasound-guided intervention systems. *IEEE Transactions on Biomedical Engineering*, 61(10):2527–2537, 2014.

[118] 3dscanexpert.com. HP 3D STRUCTURED LIGHT SCANNER

PRO S3 (DAVID SLS-3) REVIEW. https://3dscanexpert.com/hp-3d-scanner-pro-s3-david-sls-3-review/. (Accessed: Jan 2019).

[119] Xiaochen Yang, Rohan Vijayan, Ma Luo, Logan W Clements, Reid C Thompson, Benoit M Dawant, and Michael I Miga. Trackerless surgical image-guided system design using an interactive extension of 3d slicer. In *Medical Imaging 2018: Image-Guided Procedures, Robotic Interventions, and Modeling*, volume 10576, page 105761F. International Society for Optics and Photonics, 2018.

[120] Rohan C Vijayan, Reid C Thompson, Lola B Chambless, Peter J Morone, Le He, Logan W Clements, Rebekah H Griesenauer, Hakmook Kang, and Michael I Miga. Android application for determining surgical variables in brain-tumor resection procedures. *Journal of Medical Imaging*, 4(1):015003–015003, 2017.

[121] Sarah Frisken, Prashin Unadkat, Xiaochen Yang, Michael I Miga, and Alexandra J Golby. Intra-operative measurement of brain deformation. In *Biomechanics of the Brain*, pages 303–319. Springer, 2019.

[122] Senhu Li, Jonathan M Waite, Brian T Lennon, James D Stefansic, Rui Li, and Benoit M Dawant. Development of preoperative liver and vascular system segmentation and modeling tool for image-guided surgery and surgical planning. In *Medical Imaging 2008: Visualization, Image-Guided Procedures, and Modeling*, volume 6918, page 69180C. International Society for Optics and Photonics, 2008.

[123] Thomas S Pheiffer and Michael I Miga. Toward a generic real-time compression correction framework for tracked ultrasound. *International journal of computer assisted radiology and surgery*, 10(11):1777–1792, 2015.

[124] Xiaochen Yang, Saramati Narasimhan, Ma Luo, Reid C Thompson, Lola B Chambless, Peter J Morone, Le He, Benoit M Dawant, and Michael I Miga. Development

and evaluation of a trackerless surgical planning and guidance system based on 3d slicer. *Journal of Medical Imaging*, 6(3):035002, 2019.

[125] Ishita Chen, Aaron M Coffey, Siyi Ding, Prashanth Dumpuri, Benoit M Dawant, Reid C Thompson, and Michael I Miga. Intraoperative brain shift compensation: accounting for dural septa. *IEEE Transactions on Biomedical Engineering*, 58(3):499–508, 2010.

[126] Ma Luo, Sarah F Frisken, Jared A Weis, Logan W Clements, Prashin Unadkat, Reid C Thompson, Alexandra J Golby, and Michael I Miga. Retrospective study comparing model-based deformation correction to intraoperative magnetic resonance imaging for image-guided neurosurgery. *Journal of Medical Imaging*, 4(3):035003, 2017.

[127] H Richard Winn. *Youmans neurological surgery*, volume 1. Elsevier/Saunders, 2011.

[128] Kamran Tabaddor and Kenneth Shulman. Definitive treatment of chronic subdural hematoma by twist-drill craniostomy and closed-system drainage. *Journal of neurosurgery*, 46(2):220–226, 1977.

[129] Wilson T Asfora and Lisa Schwebach. A modified technique to treat chronic and subacute subdural hematoma. *Surgical neurology*, 59(4):329–332, 2003.

[130] Tyler J Kenning, John C Dalfino, John W German, Doniel Drazin, and Matthew A Adamo. Analysis of the subdural evacuating port system for the treatment of subacute and chronic subdural hematomas. *Journal of neurosurgery*, 113(5):1004–1010, 2010.

[131] David Balser, Shaun D Rodgers, Blair Johnson, Chen Shi, Esteban Tabak, and Uzma Samadani. Evolving management of symptomatic chronic subdural hematoma: experience of a single institution and review of the literature. *Neurological research*, 35(3):233–242, 2013.

[132] Aswin Chari, Angelos G Kolias, Thomas Santarius, Simon Bond, and Peter J Hutchinson. Twist-drill craniostomy with hollow screws for evacuation of chronic subdural hematoma: A systematic review. *Journal of neurosurgery*, 121(1):176–183, 2014.

[133] Matthew T Neal, Wesley Hsu, Jillian E Urban, Nicole M Angelo, Thomas A Sweasey, and Charles L Branch Jr. The subdural evacuation port system: outcomes from a single institution experience and predictors of success. *Clinical neurology and neurosurgery*, 115(6):658–664, 2013.

[134] Amit Singla, Walter P Jacobsen, Igor R Yusupov, and David A Carter. Subdural evacuating port system (seps)minimally invasive approach to the management of chronic/subacute subdural hematomas. *Clinical neurology and neurosurgery*, 115(4):425–431, 2013.

[135] Anand I Rughani, Chih Lin, Travis M Dumont, Paul L Penar, Michael A Horgan, and Bruce I Tranmer. A case-comparison study of the subdural evacuating port system in treating chronic subdural hematomas. *Journal of neurosurgery*, 113(3):609–614, 2010.

[136] Andreas Raabe, René Krishnan, Robert Wolff, Elvis Hermann, Michael Zimmermann, and Volker Seifert. Laser surface scanning for patient registration in intracranial image-guided surgery. *Neurosurgery*, 50(4):797–803, 2002.

[137] Kurt Schicho, Michael Figl, Rudolf Seemann, Markus Donat, Michael L Pretterklieber, Wolfgang Birkfellner, Astrid Reichwein, Felix Wanschitz, Franz Kainberger, Helmar Bergmann, et al. Comparison of laser surface scanning and fiducial marker–based registration in frameless stereotaxy. *Journal of neurosurgery*, 106(4):704–709, 2007.

[138] Yifeng Fan, Dongsheng Jiang, Manning Wang, and Zhijian Song. A new markerless

patient-to-image registration method using a portable 3d scanner. *Medical physics*, 41(10):101910, 2014.

[139] Christopher R Mascott, Jean-Christophe Sol, Philippe Bousquet, Jacques Lagarrigue, Yves Lazorthes, and Valérie Lauwers-Cances. Quantification of true in vivo (application) accuracy in cranial image-guided surgery: influence of mode of patient registration. *Operative Neurosurgery*, 59(suppl_1):ONS–146, 2006.

[140] Songbai Ji, Xiaoyao Fan, David W Roberts, and Keith D Paulsen. Efficient stereo image geometrical reconstruction at arbitrary camera settings from a single calibration. In *International Conference on Medical Image Computing and Computer-Assisted Intervention*, pages 440–447. Springer, 2014.

[141] Wenjie Luo, Alexander G Schwing, and Raquel Urtasun. Efficient deep learning for stereo matching. In *Proceedings of the IEEE Conference on Computer Vision and Pattern Recognition*, pages 5695–5703, 2016.

[142] Zhuoyuan Chen, Xun Sun, Liang Wang, Yinan Yu, and Chang Huang. A deep visual correspondence embedding model for stereo matching costs. In *Proceedings of the IEEE International Conference on Computer Vision*, pages 972–980, 2015.